1978

Spectral contamination in binary X-ray systems: gas flow effects on mass determinations

Mark Aldrich Moulding
Iowa State University

INFORMATION TO USERS

This material was produced from a microfilm copy of the original document. While the most advanced technological means to photograph and reproduce this document have been used, the quality is heavily dependent upon the quality of the original submitted.

The following explanation of techniques is provided to help you understand markings or patterns which may appear on this reproduction.

1. The sign or "target" for pages apparently lacking from the document photographed is "Missing Page(s)". If it was possible to obtain the missing page(s) or section, they are spliced into the film along with adjacent pages. This may have necessitated cutting thru an image and duplicating adjacent pages to insure you complete continuity.

2. When an image on the film is obliterated with a large round black mark, it is an indication that the photographer suspected that the copy may have moved during exposure and thus cause a blurred image. You will find a good image of the page in the adjacent frame.

3. When a map, drawing or chart, etc., was part of the material being photographed the photographer followed a definite method in "sectioning" the material. It is customary to begin photoing at the upper left hand corner of a large sheet and to continue photoing from left to right in equal sections with a small overlap. If necessary, sectioning is continued again — beginning below the first row and continuing on until complete.

4. The majority of users indicate that the textual content is of greatest value, however, a somewhat higher quality reproduction could be made from "photographs" if essential to the understanding of the dissertation. Silver prints of "photographs" may be ordered at additional charge by writing the Order Department, giving the catalog number, title, author and specific pages you wish reproduced.

5. PLEASE NOTE: Some pages may have indistinct print. Filmed as received.

University Microfilms International
300 North Zeeb Road
Ann Arbor, Michigan 48106 USA
St. John's Road, Tyler's Green
High Wycombe, Bucks, England HP10 8HR

Spectral contamination in binary X-ray systems: Gas flow effects on mass determinations

by

Mark Aldrich Moulding

A Dissertation Submitted to the
Graduate Faculty in Partial Fulfillment of
The Requirements for the Degree of
DOCTOR OF PHILOSOPHY

Department: Physics
Major: Astrophysics

Approved:

Signature was redacted for privacy.

In Charge of Major Work

Signature was redacted for privacy.

For the Major Department

Signature was redacted for privacy.

For the Graduate College

Iowa State University
Ames, Iowa

1978

TABLE OF CONTENTS

		Page
I.	INTRODUCTION	1
	A. Statement of Problem	1
	B. Background - General	2
	C. Background - Cygnus X-1	9
	D. Velocity Curve Distortion Mechanisms	17
II.	GENERATION OF LOW-MASS BINARY MODELS	21
III.	GENERATION OF THE REQUIRED EMISSION LINES	27
	A. Emission-Absorption Blending: Theory	27
	B. Application to Cygnus X-1	33
IV.	GENERATION OF PHYSICALLY EXPECTED EMISSION LINES	60
	A. Gas Flow Models in Emission: Theory	60
	B. Application to Cygnus X-1	76
V.	DISCUSSION	108
	A. Comparison of Emission Lines	108
	B. Qualifications and Assumptions	117
	C. Other Implications of Low-Mass Models	126
	D. Tests for Blending Effects	127
VI.	BIBLIOGRAPHY	132
VII.	ACKNOWLEDGMENTS	137
VIII.	APPENDIX: COMPUTATIONAL TECHNIQUES	138
	A. Methods and Tests	138
	B. Computer Codes	143

I. INTRODUCTION

A. Statement of Problem

As a source of valuable information about the extra-terrestrial universe, binary star systems have proved to be most important. Indeed, information derived from the study of binaries has been used as a foundation in the understanding of many astrophysical phenomena. Appropriately, considerable effort has been channeled into the analysis of such systems, bringing the field to a level of some sophistication. The frontier of binary system analysis currently lies in the study of the proximity effects arising in close binaries. Here "close" is understood to describe a system in which gravitational distortion, mutual irradiation or mass transfer from one component to the other may become significant at some time in its evolution. These interacting systems contain potentially vast amounts of information about stellar structure and evolution and consequently are more complicated to analyze than other binaries. Therefore, when apparently new physical behavior is observed in such systems, the techniques of analysis themselves merit particularly close study for accuracy, completeness and uniqueness before such behavior can be properly verified. In this paper such a situation is shown to arise in the analysis of close X-ray binaries and an examination of the methods used is carried out in the context

of one member of that class of objects - Cygnus X-1. The immediate purpose of this study is to evaluate the nature of the secondary star in the Cygnus X-1 system, an object which, under conventional analytic procedures, has been shown to be a promising candidate for the first observed black hole.

B. Background - General

The advent of X-ray astronomy in the mid-1960's opened the door on a new and exciting class of objects. Study of the newly discovered discrete X-ray sources quickly defined the characteristics of this group, with particularly intriguing results. Each member consisted of a compact X-ray source (X-ray luminosity: 10^{36}-10^{38} ergs/sec) as the secondary component in a close (period: a few days), single-line, spectroscopic binary with an early supergiant primary. The secondaries are known to be compact objects from the variation timescales and luminosity of the X-ray radiation (cf. Pringle and Rees 1972, Webster and Murdin 1972). This conclusion is also consistent with results concerning the expected visibility of "normal" stars of the same mass (cf. Hutchings 1974, Blumenthal and Tucker 1974). See however, Avni and Bahcall (1975).

Definite spectral irregularities are also characteristic of X-ray binaries with early primaries. Absorption lines often

exhibit variations, asymmetries or filling in and many of the primaries show small spectral type changes, peculiarities or uncertainties (e.g., Smith et al. 1973 for Cygnus X-1). Emission in hydrogen, helium and other lines is observed in Cygnus X-1 (cf. Bolton 1972) and other systems, and is seen to vary with orbital phase (cf. Hutchings et al. 1973). Generally it is difficult to measure the spectra of these systems for reliable radial velocities - the blue star has relatively few measurable lines ($\sim$10) - and large scatter in radial velocity curve data is not uncommon. Large measuring errors are inherent in the spectra of early stars (Batten 1973a). Profile variations have been correlated with these velocity anomalies for some systems (cf. Zuiderwijk et al. 1974). Osmer and Hiltner (1974) and Wickramasinghe et al. (1974) display radial velocity data indicative of emission line influence in the SMC X-1 and Vela X-1 systems and Wolff and Morrison (1974) observed considerable scatter among velocities derived for different lines in the 2U 1700-37 system as do Zuiderwijk et al. (1974) for Vela X-1. Finally, the light curves seem to indicate that the orbits are generally circular and that gravitational distortion of the primary's surface may be significant.

These characteristic irregularities are clear evidence of the significance of proximity effects in these high-energy systems. In particular, mass flow between the components

seems to be essential to the understanding of these objects (below). While some spectral irregularities can be attributed to atmospheric motion characteristic of early primaries in general, the evidence for mass streaming seems inescapable (cf. Batten 1973a, Abhyankar 1959, for spectral effects of significant mass flow systems). Such a conclusion also explains X-ray absorption events in Cygnus X-1 (Mason et al. 1974) and is consistent with expectations from the theory of close binary star evolution (cf. Plavec 1970, Prendergast 1960, Biermann 1971). The presence of such interaction effects, especially the apparent interference with velocity determinations, indicates that considerable care must be taken in the interpretation of observations of these systems, particularly with respect to velocity curve data.

Figure 1 illustrates the basic model for the binary X-ray sources in which the mass flow plays a central role. The sketch is of the orbital plane and is labeled with positional phases convenient for the discussion of phase effects. Since thermalization of accreting gas is the most convincing mechanism for the X-ray production in these systems, some type of mass flow is common to all such models. The mass flow shown in the figure derives from the primary's overflow of its Roche lobe (dotted line), resulting in a gas stream injected into orbit around the secondary

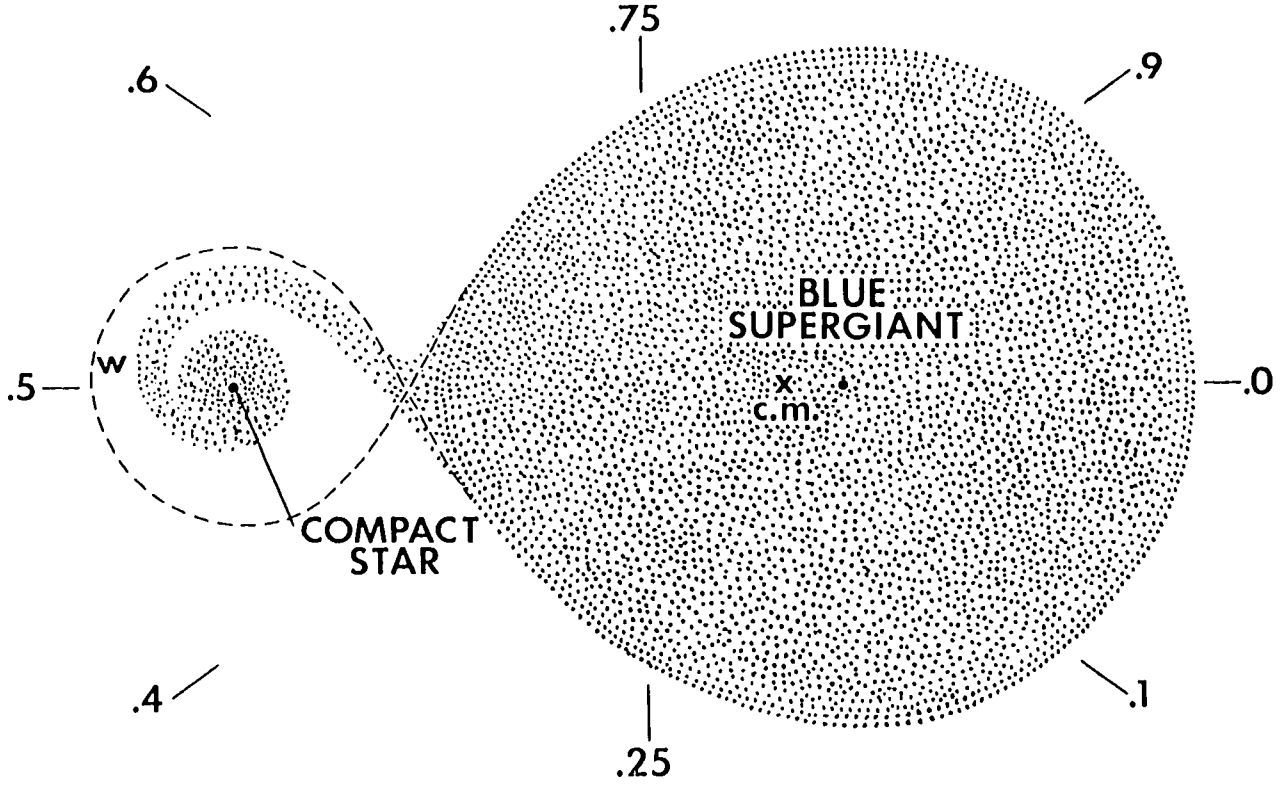

Figure 1. Typical binary X-ray source model

through the inner Lagrangian point. Conservation of angular momentum suggests that a radiating disk, rotating in the prograde sense, will be formed from this material (cf. Pringle and Rees 1972). As viscous forces transport angular momentum outward, mass accretes onto the compact star under the influence of the star's magnetic field and there produces the observed X-rays. Two main problems plagued these models initially. It was hard to understand how the lower mass star could be the more evolved component, and, in the light of the supernova theories of neutron star formation, it was difficult to explain how such a system could remain bound at all (cf. Gott 1972). These problems were resolved by supposing that the secondary was originally the more massive component and that before reaching the supernova stage, rapid mass transfer (of the Roche lobe overflow type) occurred. The subsequent supernova could not disrupt the system because less than half of the system mass was lost. This picture is supported by evolutionary calculations (referenced above, but see Oda et al. (1971) for evidence against the supernova picture), and the model of Figure 1 will be the focus of attention in this paper. For completeness it should be noted that overflow of the Roche lobe is not the only source of mass for X-ray production. For a primary within its Roche surface a moderate stellar wind is sufficient to power the X-rays (Davidson and Ostriker 1973). In such a case the injection into orbit

around the secondary is shock front driven from an injection point near "w" in Figure 1 (Prendergast 1960, Biermann 1971). Instances arise in which these wind accretion models are important. For example, the rate of mass transfer by Roche lobe overflow can easily become so great that the X-ray production is choked off. Wind accretion has no such problem. In this paper the Roche model is assumed. This choice will be discussed below and it will be seen to have little effect on the results.

Mass determinations are of primary interest in the analysis of these systems. Application of conventional methods of analysis has led to high mass values for the compact stars in several systems. In at least four cases - Cygnus X-1, 3U 1700-37, Vela X-1, SMC X-1 - the possibility that the secondary was a black hole was raised (cf. Webster and Murdin 1972, Bessell et al. 1974, Wickramasinghe et al. 1974, Osmer and Hiltner 1974). Presently, evidence supporting neutron star models for the other X-ray stars (cf. Joss et al. 1975) makes Cygnus X-1 the only remaining black hole candidate.

The black hole has been an object of extreme interest for many years and verification of the possibility that Cygnus X-1 is such an object would be a most significant event. Wheeler et al. (1973) have discussed the theory of gravitational collapse as "the greatest crisis in physics of all time." A confirmed observation of a completely collapsed

object would constitute an important statement on the validity of the general theory of relativity in extreme environments. This theory predicted the existence of such objects more than fifty-five years ago. The properties of black holes have been used in modeling many astrophysical phenomena: QSO's, galactic cores, globular clusters, a closed universe and more. Black holes have served as a focal point for the development of quantum geometrodynamics. All such related inquiries would profit from such an existence proof.

The existence of black holes in theory derives from the failure to explain how the usual forces of nature could support the collapse of a massive star under its own gravitation. Stars more massive than the upper limit of the stable neutron star mass range must somehow shed this extra mass or eventually become black holes. Considerable effort has been directed toward the determination of this upper limit. Conservatively it is placed at about two solar masses (cf. Bludman 1973, Zeldovich and Novikov 1971) by equation-of-state and causality arguments. Recent treatments have slightly extended this limit (cf. Brecher and Caporaso 1975, Hegyi et al. 1975, Abramowicz and Wagoner, 1976). Rigid and differential rotation effects and the predictions of different theories of gravitation are discussed by Hegyi (1977) and Mikkelsen (1977). Some extension of the neutron star mass range is suggested and

in one case, arbitrarily massive neutron stars are allowed. In this paper, and until these theories are evaluated, any compact object greater than two solar masses will be taken as a black hole. This represents the most conservative choice with respect to the present study.

The significance of the black hole candidacy of Cygnus X-1 is clear. It is also apparent that these highly interactive binary components may require more than the conventional analysis. Therefore a closer scrutiny of the methods leading to this conclusion seems appropriate.

C. Background - Cygnus X-1

While being anomalous in its black hole candidacy, Cygnus X-1 is also unusual in the limited amount of information it presents to the observer for analysis. Unlike other close X-ray binaries, Cygnus X-1 exhibits no X-ray eclipses. Furthermore, its X-ray radiation is not periodic as in some other systems, precluding the possibility of analyzing the system as a two-line spectroscopic binary. These deficiencies underscore the value of a critical review of the conventional analytic techniques. The X-ray luminosity of Cygnus X-1 is about 3×10^{36} ergs/sec between 2 and 10 keV with a spectrum that may be a combination of thermal sources, perhaps represented by $T \approx 10^{7}$ °K, and some nonthermal radiation. The X-ray radiation displays high variability (time scales of

50 ms to seconds), sometimes in pulse trains lasting for tens of seconds and with a large fraction (up to 50%) of the energy affected. No low-end cut-off is seen in the X-ray spectrum. See Blumenthal and Tucker (1974) for more information.

Identification of this X-ray source with a visual companion is certain. X-ray absorption events have confirmed this conclusion (Mason et al. 1974) and an observed correlation between radio and X-ray behavior (Tananbaum et al. 1972) has permitted the use of the accurate radio position to firmly associate Cygnus X-1 with the 9th magnitude B0Iab star HDE226868. The light curve is shallow (B amplitude of $\sim$.07 magnitude) and has symmetry corresponding to an ellipsoidally shaped primary with no reflection effect. This is readily understood when the luminosity of the secondary is compared to that of the blue supergiant ($\sim 10^{39}$ ergs/sec). The spectral type is normal, but slightly variable (Walborn 1973). The radial velocity curve (amplitude $\simeq$ 73 km/s) has the large scatter often seen in these systems, and while it appears to have particularly significant scatter at the phases of quadrature, a power spectrum analysis of curve residuals indicates no systematic deviation from an almost circular ($\varepsilon \simeq .05$) 5.6 day Keplerian orbit (Murdin 1975). Finally, we note that emission lines of Hα and HeII λ4686 are seen which vary with phase and are not associated with the primary (cf. Smith et al.

1973, Brucato and Zappala 1974, Hutchings et al. 1974).

The relative shortage of data from Cygnus X-1 mentioned earlier causes the estimates for the secondary mass and the consequent arguments for black hole candidacy to rely heavily on the accurate determination of the system mass function f(m) from the radial velocity curve. Here

$$f(m) = (M_x \sin i)^3/(M_x+M_p)^2 = K_1{}^3 P(1-\varepsilon^2)^{3/2}/8\pi^3 \quad (1)$$

where M_p, M_x and i are primary and secondary masses and orbital inclination, and the measurables P, ε, K_1 are orbital period, eccentricity and the average of the two semiamplitudes of the radial velocity curve. Once the X-ray source is firmly associated with a binary system and f(m) obtained, an independent determination of M_p (from spectral type, distance measurements, fits to theoretical evolutionary tracks) yields a lower limit for M_x (cf. Brucato and Kristian 1973). Light curve and X-ray eclipse data may then provide additional constraints, increasing this lower limit by allowing an estimate of i. As observed earlier, if this limit is greater than about 2 $M_\odot$ the compact star is taken to be a black hole. For Cygnus X-1 this limit has been as high as $\sim$15 $M_\odot$ (Bolton 1972, Hutchings et al. 1973), making it a prime black hole candidate.

Figure 2 shows graphically how this analysis is applied to Cygnus X-1. The observed mass function corresponds to a

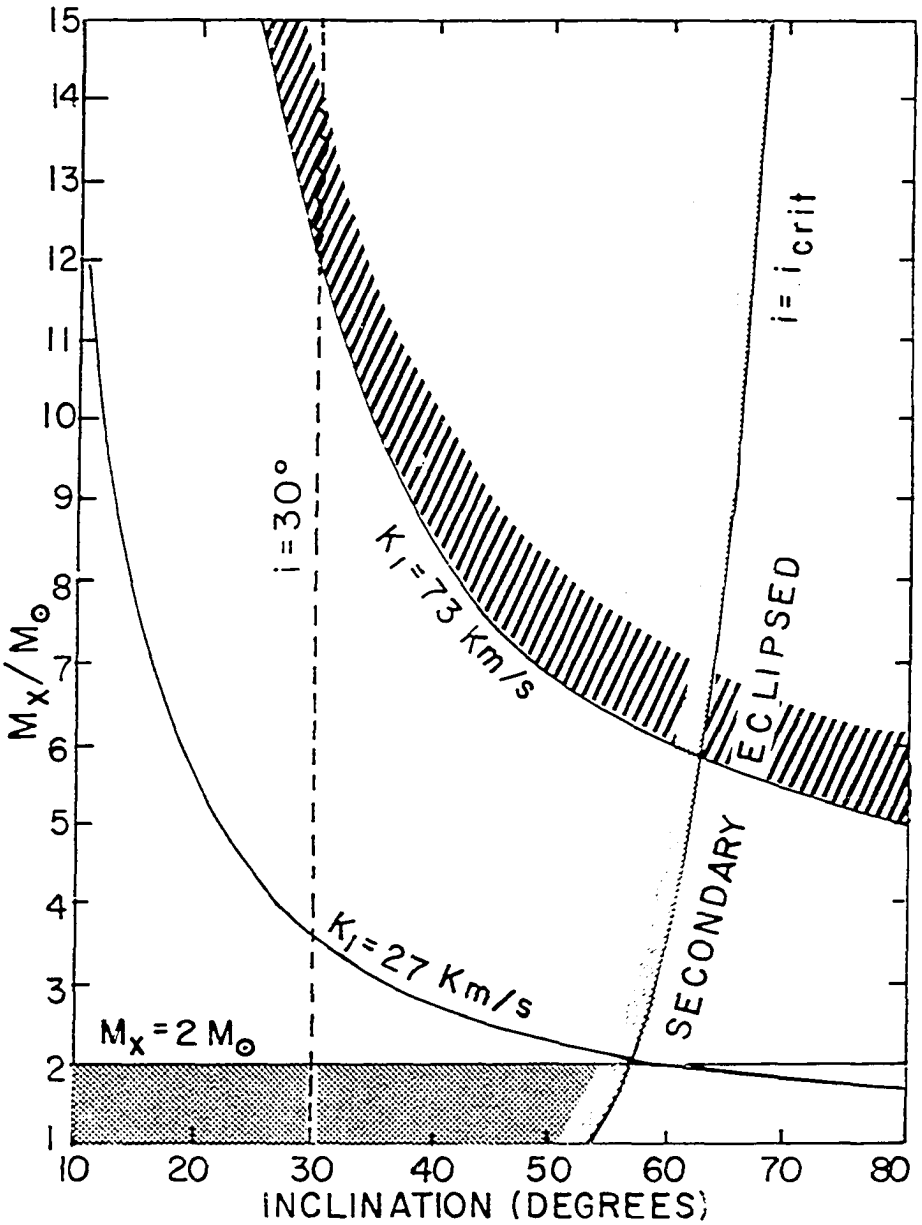

Figure 2. Secondary mass versus inclination angle

velocity curve amplitude of 73 km/s. This mass function appears as a line in the M_x versus i plot for the choice M_p = 18 $M_\odot$. This choice for M_p is reasonable for the spectral type and luminosity of HDE226868 and is a good starting point. The hatching along this line represents uncertainty in this choice and extends to the case M_p = 25 $M_\odot$. Uncertainty in the value for K_1 is not included. From this line alone, $M_x > 4.9\ M_\odot$. Next the line $i = i_{crit}$ is placed on the figure. Assuming the primary fills its Roche surface and that the secondary is a point source of X-rays, inclination angles above this critical value would lead to unobserved X-ray eclipses. The derivation of this line will be discussed later, as will the various assumptions and approximations made in this analysis. Again the hatching represents the uncertainty in primary mass. The intersection of the two lines leads to $M_x > 5.9\ M_\odot$. Finally, light curve analysis may suggest that $i \simeq 30°$. The strength of this conclusion will be discussed later. This information leads to a range M_x = 12-14 $M_\odot$ (squiggly line).

It seems that for Cygnus X-1 to be a neutron star (cross-hatched region) the mass function must correspond to a radial velocity curve amplitude of at most 27 km/s. Figure 3 illustrates further this conclusion. In it are displayed radial velocity observations for HDE226868. The different symbols denote data taken by different groups and are

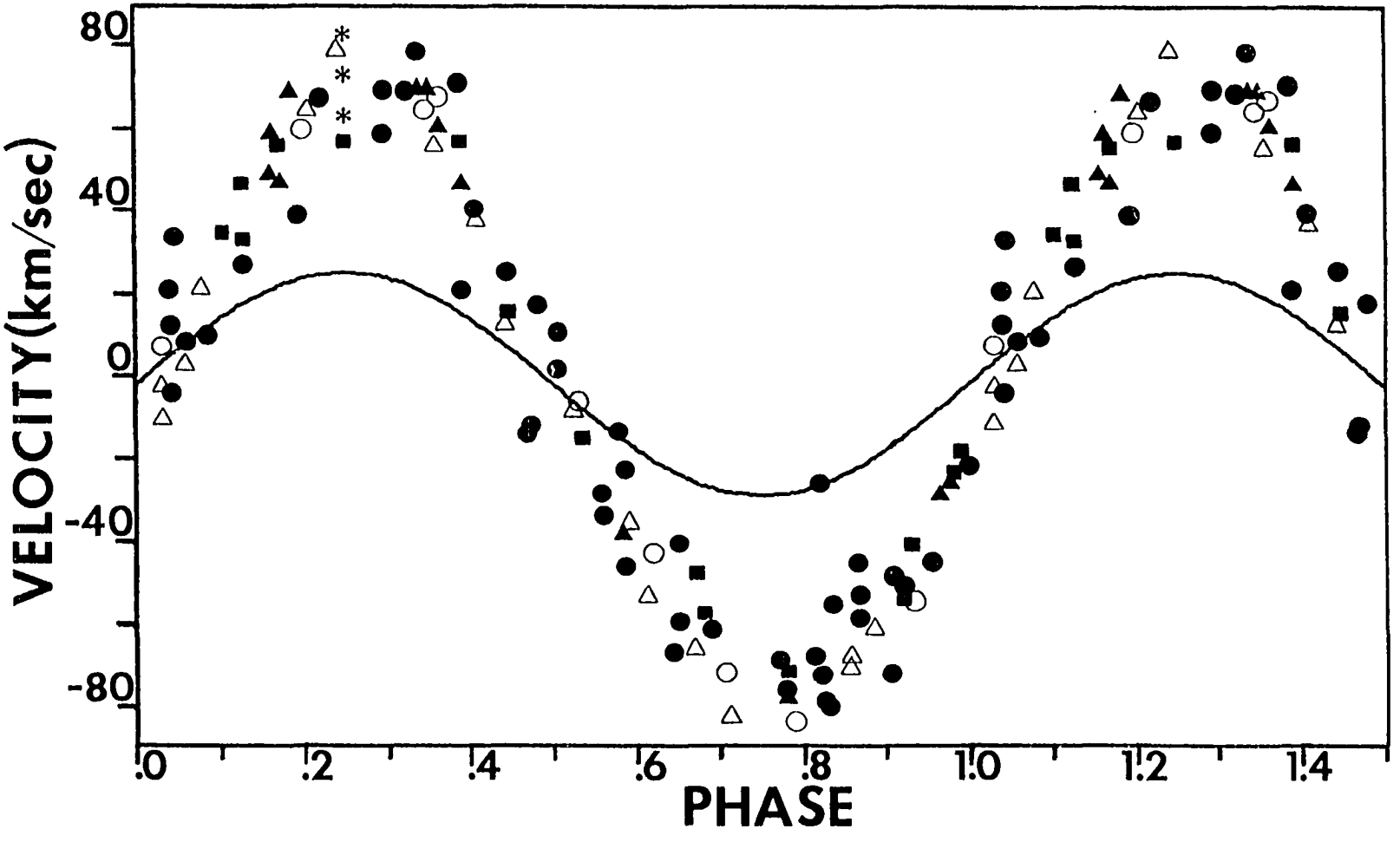

Figure 3. Radial velocity data for HDE226868 (Cygnus X-1)

consistent with the symbols used by Mason et al. (1974). Phases were calculated using t_0 = JD2441163.351, P = 5.60096 da. and the systematic velocity corrections suggested by Mason et al. (1974) were used. The sine curve shown represents the normal radial velocity curve expected for a model of this system containing a $2M_\odot$ (neutron star) secondary. The model is derived in Section II. Its parameters are found in a table in that section, and will be discussed there. This paper focuses on explaining the disparity between this curve and the data points displayed in Figure 3. As a preface to this inquiry, past attempts at explaining this apparent high-mass system should be reviewed.

Models for Cygnus X-1 which avoid the conclusion that it is a black hole have been advanced by several investigators. Trimble et al. (1973) argued for a lower value for the primary mass. If it were low enough, the 73 km/s curve in Figure 2 would intersect the cross-hatched neutron star region. Subsequent distance measurements (Bregman et al. 1973, Margon et al. 1973) verified the higher luminosity of the more massive primary, diminishing this possibility. Bahcall et al. (1974) and Fabian et al. (1974) have suggested that the X-ray source is not a member of a binary, but rather of a trinary system. The intrinsic low stability of such a system makes it unlikely that it could contain highly evolved components, much less sustain neutron star formation unaffected. The mass transfer

or loss evidenced in X-ray systems would test the stability of such a configuration to the extreme. Apparently light curve and X-ray eclipse constraints are also violated by a trinary (Hutchings 1974, Bolton 1975a). Brecher and Morrison (1973) and Lamb and Van Horn (1973) suggested that the secondary was a differentially rotating white dwarf, but problems with this model reproducing the observed X-ray variation time scales makes it unattractive (Bolton 1975a). Finally, Bahcall et al. (1973) presented a model consisting of two normal stars linked by a magnetic field whose twisted field lines would produce the X-rays. This model has not been ruled out, but the vagueness of its predictions has not earned it many disciples (Bolton 1975a).

Since the association of Cygnus X-1 with HDE226868 seems definite (above), the large secondary mass must be real, unless f(m) is somehow being systematically overestimated. Since f(m) is sensitive to K_1 (Equation 1), overestimation of the velocity curve amplitude may readily mask a low-mass secondary, as is obvious from Figure 2. Thus our scrutiny finally falls on possible mechanisms for the subtle distortion of the absorption lines of the primary in such a way that the sine curve shown in Figure 3 would be observed as the data points in that figure.

D. Velocity Curve Distortion Mechanisms

The required mechanism must account for the amplitude disparity evident in Figure 3. Moreover, it should be sinusoidal and in phase with the primary spectrum (the symmetry of the velocity curve must be maintained). Each of the proximity effects important in close X-ray binaries has the potential to effect such distortion (cf. Batten 1973a, Kopal 1959, Buerger 1969). Tidal distortion and irradiation of the primary may alter the primary lines in several ways. The dominance of one portion of the stellar surface in producing the observed continuum yields absorption lines which have velocities different from that of the center of mass. The same effect is produced by alteration of the line formation process itself: irradiation may cause an asymmetric line source function distribution. Lyutyi et al. (1973), Mauder (1973) and Hutchings et al. (1973) have shown these effects to be small for the Cygnus X-1 system. See however, Milgrom (1976) for an extreme case. Recently, Hutchings (1977) has reviewed these processes and confirmed these results. In any case, such effects would be expected to be small for a sufficiently low mass secondary.

The final possibility is that the mass flow, characteristic of these systems, can effect such distortion, with impressive results in the case of Cygnus X-1. This proposal is a natural one, for such streams exist in a radiation environment

unique to these systems and so may be the source of emission lines which can blend with primary lines in the proper way to cause significant errors in velocity determination. Furthermore, the velocity field of gas orbiting the secondary admits the possibility of emission lines arising there having the same velocity amplitude and phase as the primary spectrum. Specifically, gas in such an orbit and between the stars on the line of centers would have such properties, would be likely to be in emission because of the dual irradiation and would have maximum distorting potential at quadrature. This last property is in tune with the requirements of Figure 3. Estimates of the Keplerian orbital velocities possible for such an emission region indicate that only overestimation of the velocity curve amplitude would result from analysis of the blended line. The other proximity effects admit the possibility of underestimation as well. The distortion of velocity curves by blending of two absorption spectra has long been known to be potentially significant (Batten 1973a), and has been investigated in detail (cf. Hutchings 1973). In the light of the probable presence of significant emission line systems with regular velocity fields, it is natural to consider to what degree a similar systematic effect can derive from emission-absorption blending in these objects. Finally, we note that the same stream which produces these effects may readily explain the unblended emission seen in Cygnus X-1.

That is, such a model should be consistent with those of Smith et al. (1973), Brucato and Zappala (1974) and Hutchings et al. (1974) which have had some success explaining Hα and HeII λ4686 behavior in Cygnus X-1, and with that of Mason et al. (1974) which explains the nature of X-ray absorption events.

A conservative approach will be taken toward evaluating the feasibility of this mechanism. One line will be studied initially - Hβ. Failure to achieve significant blending at this line would defeat the mechanism because some emission contamination of Hβ is evident in HDE226868 (Bolton 1975b, Hutchings et al. 1974) and because failure at Hβ would probably rule out such behavior at other lines (Section V). The .25 quadrature configuration will be addressed, for here the distortion requirements are most harsh. Translation of the effect to other phases will be discussed in Section V. Specifically the three points labeled by asterisks in Figure 3 will be studied. It should be kept in mind that this proposed mechanism must explain, in a natural way, the anomalous nature of Cygnus X-1 without being so unique as to be contrived.

The structure of this inquiry will be by steps toward more accurate treatments, the ambition being to prove or disprove the significance of this mechanism with the simplest arguments. The first major goal therefore is to find the set of all hypothetical emission lines, each of whose presence

could account for the amplitude disparity between the curves of Figure 3. If the resulting set is null, the mechanism will have failed and the black hole candidacy of Cygnus X-1 will be strengthened. If, however, such emission lines can be found, the probability of their actual production in an X-ray binary must be discussed before any conclusions can be made about the mass of the compact star. Therefore the second major goal will be a derivation of the emission lines expected from typical mass streaming models for comparison with the set of emission lines required for significant primary line distortion and the sanctioning of neutron star models for Cygnus X-1. A valuable result of such a successful study must be the identification of observables sensitive to this effect, and the final goal of this investigation must be to suggest some observational tests for the presence of this mechanism in Cygnus X-1 and other similar objects. Finally, to clearly underscore the limitations of this treatment, most of the qualifications, assumptions and approximations will be discussed together in Section V.

II. GENERATION OF LOW-MASS BINARY MODELS

As a first step in the examination of emission - absorption blending it is necessary to describe the uncontaminated absorption line expected from a typical low-mass (neutron star) binary system having the spectral type, period, eccentricity and apparent lack of X-ray eclipses characteristic of the HDE226868 - Cygnus X-1 system. An Hβ profile common to non-rotating stars of HDE226868's spectral type may be obtained from observations or from theoretical model atmospheres. The dynamic properties of the particular binary system then alter this profile in several ways. First, the proximity effects of tidal distortion and irradiation may alter the line as noted earlier. It is assumed that such effects are not significant for Cygnus X-1, as was concluded in the last section. Second, the rotation of the primary will broaden the original line. Finally, and most importantly, the actual velocity amplitude of the primary will define the Doppler position of the profile at the phase of interest - the .25 quadrature. It is the emission line distortion of this profile away from this position which is central to the thesis.

In order to describe these effects a grid of such binary system models was generated. The grid size was defined by $1 \leq M_x/M_\odot \leq 2$, $12 \leq M_p/M_\odot \leq 30$, with either $i = i_{crit}$ or

$i = 30°$. Here i_{crit} is the inclination at which eclipse of the secondary (point source) by a primary filling its Roche surface is just avoided. Support for the choice $i = i_{crit}$ is marginal and consists mainly of X-ray observations and emission line weakening at conjunction (cf. Mason et al. 1974, Smith et al. 1973). Certainly a lower inclination is possible, but the higher value may prove consistent with other observations (Section V). In any case, $i = 30°$ is also considered. As noted by Davidson and Ostriker (1973), a stellar wind accretion model may explain X-ray emission without requiring the primary to fill its Roche lobe. Use of the Roche lobe as a critical surface has also been criticized by investigators who point out the need for inclusion of the effects of a solar wind, radiation and revolution (cf. Schuerman 1972, Kondo 1974). In the present case however, the geometry used was based on the Roche model of Kopal (1959), and the resulting size of the primary lobe was seen to be generally consistent with the radius expected for a star of HDE226868's spectral type ($\sim 20\ M_\odot$). This approximation will be studied further in Section V. The rotation of the primary is also specified by the use of Roche geometry because such a choice demands synchronization of rotation and revolution. Synchronization is apparently consistent with the circularization ($\varepsilon \simeq 0$) of the system from a probably

once-high eccentricity (cf. Gott 1972, Press et al. 1975). See however, Pratt and Strittmatter (1976). It should be kept in mind that the shape of the blended line should be consistent with the observed projected rotational velocity. This possibility is also discussed in Section V.

The geometry of the Roche potential surfaces is fundamental to the calculation of this grid of binary models because it determines the critical inclination aspect i_{crit}. Simple approximations have been used by others to estimate this value (e.g. Bolton 1975a), but such a treatment is not valid for the small secondary/primary mass ratio under consideration here. The geometry is derived from the equation for the potential at any point in a two point-mass system having mutual separation R and an orbital angular frequency ω:

$$\Psi = G(M_p/r + M_x/r_x) + \omega^2[(x-x_0)^2+y^2]/2 \qquad (2)$$

where the coordinate system has its origin at the center of mass of M_p and x increases along the line of centers toward M_x. The z axis is perpendicular to the orbital plane. Also, $r^2 = x^2 + y^2 + z^2$, $r_x^2 = (R-x)^2 + y^2 + z^2$ represent respective distances from the mass points to the point (x,y,z) in question. Here $x_0 = RM_x/(M_x+M_p)$ represents the system center of mass and ω is taken to be Keplerian: $\omega^2 = G(M_p+M_x)/R^3$. Surfaces of constant Ψ are the Roche equipotentials.

The condition $\partial\Psi/\partial x = \partial\Psi/\partial y = 0$ defines the inner Lagrangian point and therefore the value of Ψ on the critical surface ($=\Psi_0$). Once this value is determined, Equation (2) allows the computation of the surface parameters - mean radius, equivalent spherical volume radius, length of the three semimajor axes - once supplementary conditions characterizing particular points are specified. Such a program was carried out numerically for each M_x, M_p pair in the grid. Some expansions for the effective radii presented by Kopal (1959) were used in part of this program. The determination of i_{crit} was carried out by solving Equation (2) with $\Psi=\Psi_0$ simultaneously with an equation for the line of sight to M_x which was tangent to the critical surface in the x-z plane. The point (x,z) of intersection was computed efficiently using a two-dimensional Newton-Raphson method. Since the resulting critical eclipse angle i_{crit} depends only on the secondary/primary mass ratio, the set of i_{crit}'s generated by the grid models could be used to place the line $i = i_{crit}$ in Figure 2.

For simplicity in discussing the nature of blending effects in these models, this study will focus on one member of the model grid. Consideration of how blending effects will behave in other grid models will then be done in terms of the associated changes in the results of this central study. The model chosen from the grid to serve as this reference model is

described in Table 1 along with two other models. In this table, the secondary and primary critical surface radii are mean values. The "equivalent spherical volume" radii are slightly larger (Kopal 1959). V_{real} and V_s are the primary and secondary orbital radial velocities at the .25 quadrature, and V_0 is the observed system center of mass radial velocity (e.g. Bolton 1975a). The assumption that the orbit is circular ($\varepsilon \approx 0$) will receive further treatment in Section V.

Table 1. Examples of low-mass secondary models: $M_x = 2\ M_\odot$

System parameter	Reference model	Heavy primary model	Low inclination model
M_p ($M_\odot$)	18	25	18
R_s ($R_\odot$)	7	7	7
R_p ($R_\odot$)	19	22	19
a ($R_\odot$)	36	40	36
i (degrees)	57	55	30
P (days)	5.6	5.6	5.6
ε	0	0	0
V_0 (km/s)	-2	-2	-2
V_{real} (km/s)	27	22	16
V_s (km/s)	-245	-274	-146
V_{rot} (km/s)	145	163	87

We are now ready to investigate what kind of emission is required to make the reference model appear as a more massive system.

III. GENERATION OF THE REQUIRED EMISSION LINES

A. Emission-Absorption Blending: Theory

The intention of this section is to derive the numerical requirements for emission lines and absorption lines to blend in such a way as to be compatible with a lower mass secondary star, and then to apply these requirements to the Cygnus X-1 system. In this way we hope to see if any emission can play a role in masking a low-mass secondary. If the result is positive we may then ask whether or not such lines can actually be produced physically in these systems. This more complex problem is the subject of section IV.

This initial investigation of emission-absorption blending is concerned with the combination of two gaussian profiles in such a way as to shift the minimum of a given absorption profile to a specific, required position. The treatment is similar to that of Tatum (1968) for absorption-absorption blending. The gaussian approximation, while chosen for simplicity, may be fairly good for the Stark-broadened lines of early supergiants and for weak lines dominated by instrument response (Batten 1973a).

First an absorption line ($\mathfrak{F}_a$) at λ_a with half-width at half-depth $\Delta\lambda_a$ is considered:

$$\mathfrak{F}_a(\lambda_a,\Delta\lambda_a,D) = \mathfrak{F}_1\{1-D\exp[-(\ell n\, 2)(\frac{\lambda-\lambda_a}{\Delta\lambda_a})^2]\}. \qquad (3)$$

Here D is line depth in a continuum flux $\mathfrak{F}_1$. This profile is then modified to fit the binary model under consideration: if the following line of sight velocities are defined -

$V_0 \equiv$ system center of mass velocity

$V_{real} \equiv$ primary orbital velocity

$V_{rot} \equiv$ primary rotational velocity

then crude Doppler broadening and shifting can be written as

$$\lambda_a' = \lambda_a[1 + (V_0+V_{real})/c] \tag{4}$$

$$\Delta\lambda_a' = \Delta\lambda_a[1 + (V_0+V_{real})/c] + \alpha\lambda_a V_{rot}/2c \tag{5}$$

$$D' = D\Delta\lambda_a/\Delta\lambda_a'. \tag{6}$$

Here the primed notation identifies the Doppler-altered quantities. Equation (6) expresses the conservation of energy in the primary line. The parameter α is a broadening efficiency factor determined by the susceptibility of the line to rotational broadening. Its value could be estimated from more exact treatments of such broadening (cf. Cowley 1970), but in this study α is varied from unity (probably good for the scattering lines considered here) only to test the sensitivity of the results to this parameter. This approach also allows, in effect, a test of the response of the blending mechanism to primary absorption lines of different widths. This will be important in suggesting observational tests for this mechanism later (Section V).

The blended line ($\mathfrak{F}_b$) is obtained by contamination of the new absorption line with gaussian emission ($\mathfrak{F}_e$) at λ_e having half-width at half-maximum $\Delta\lambda_e$:

$$\mathfrak{F}_b = \mathfrak{F}_a(\lambda_a', \Delta\lambda_a', D') + \mathfrak{F}_e \tag{7}$$

where

$$\mathfrak{F}_e = \mathfrak{F}_2\{1 + H \exp[-(\ell n\ 2)(\frac{\lambda-\lambda_a}{\Delta\lambda_a})^2]\}. \tag{8}$$

Here H is the emission line height in a continuum flux $\mathfrak{F}_2$. To facilitate numerical study of this profile the following dimensionless variables are defined:

profile position

$$X = (\lambda-\lambda_a')/\Delta\lambda_a', \tag{9}$$

separation of blending lines

$$S = (\lambda_a'-\lambda_e)/\Delta\lambda_a', \tag{10}$$

emission line half-width at half-maximum (HWHM)

$$W = \Delta\lambda_e/\Delta\lambda_a', \tag{11}$$

normalized blend intensity

$$y = \mathfrak{F}_b/\mathfrak{F}_1, \tag{12}$$

relative secondary continuum strength

$$F = \mathfrak{F}_2/\mathfrak{F}_1, \tag{13}$$

so that

$$y = 1 - D' \exp[(-(\ell n\, 2) X^2] + F\{1 + H \exp[-(\ell n\, 2)(\frac{X+S}{W})^2]\}. \quad (14)$$

If V_{OB} represents the observed amplitude of the velocity curve, the observed position of the blend minimum (relative to λ_a') may also be expressed in a dimensionless form:

$$X_{min} = \{\lambda_a[1 + (V_0 + V_{OB} + V_{OB})/c] - \lambda_a'\}/\Delta\lambda_a' \quad (15)$$

where ΔV_{OB} is any observational uncertainty in the determination of V_{OB} but will hereafter be taken from the range of 'fitting scatter' especially obvious at quadrature in Figure 3. Then

$$y'(X_{min}) = 0 \quad (16)$$

is the condition that the blend minimum fit this observed position. Presumably, for a given absorption line (λ_a, $\Delta\lambda_a$, D), system model (λ_a', $\Delta\lambda_a'$, D') and observed orbital velocity ($V_{OB} + \Delta V_{OB}$), a set of emission lines (H, W, S) can be found that satisfy condition (16) for a suitable choice of F. From S (i.e. λ_e) the velocity of the emission region in the system may be determined. To facilitate comparison of these emission lines with possible emission region velocity fields, a velocity V_e was defined as follows. By assuming that the emission transition is the same as the transition of the chosen absorption line, the separation can be converted

directly to the stream radial velocity measured with respect to the secondary at this orbital phase. The corresponding velocity in the orbital plane is just V_e, where the motion of the emitting gas is taken to be in that plane.

We are interested in the nature and number of emission lines in the solution set derived for Cygnus X-1. Several constraints limit the size of this set however. Since the relative strengths of the observed primary lines are close to normal for the spectral type (Walborn, 1973), and the magnitude of spectral type variation with phase is low, the profile distortion caused by the blending should be kept to a minimum. Since it is likely that any emission may be reduced at conjunction (Section V), the uncontaminated λ_a' absorption line will be used as a reference line in the determination of distortion limits for the blend - the closer the blend resembles a purely shifted reference line, the more acceptable it is. (It should be noted that Hutchings et al. (1973), in spectra subtraction experiments, found Cygnus X-1 profiles to be generally filled in by 30% compared to other stars of its spectral type. Although this was thought to be a subtraction problem, it is interesting to speculate that perhaps residual emission at conjunction should be accounted for by allowing a shallower reference line.) Also the resolution of emission lines inside or outside the blend should not be allowed, nor should excessive extension of the blend above the reference

continuum level $\mathfrak{F}_1$ be permitted. These last limits on distortion may be unduly harsh in light of the irregular profiles often observed. Allowable blends will be discussed in detail in the context of the Cygnus X-1 system (below).

In practice, the procedure used to derive the required emission lines was as follows. Appropriate choices were made for the relative secondary continuum strength F and for the primary Hβ absorption line parameters $\Delta\lambda_a$ and D. The reference model of Table 1 was then used to modify the line parameters (Equations 4-6). The complete set of acceptable emission lines was then computed by stepping through a grid of line height and width values (H, W), and at each step calculating numerically the separation S from Equation (16) and testing the resulting blend profile, Equation (14), for distortion. If the blend passed this last test, the associated emission line separation S was converted to a velocity V_e as outlined above. If the blend failed the distortion test, the nature of the distortion excess was recorded.

The set of acceptable emission lines (emission lines able to reconcile the curves of Figure 3 by their blending properties), defines a continuous surface in H-W-V_e space. As modeling parameters (M_x, M_p, i, α, F) and observables (V_{OB} + ΔV_{OB}) are varied within allowable limits for a given absorption line, this surface will move, tracing a solution volume. Uncertainties similar to fitting scatter (from

whose range ΔV_{OB} is taken) may also be important in the expansion of the solution set: numerically, the line positions were determined to an accuracy of .1 km/s or better, while in practice about 5 km/s is typical. Plate scatter may have a similar effect. In this way, each solution surface derived should be regarded as being slightly blurred. Examples of solution surfaces and their dependence on modeling parameters are discussed below for Cygnus X-1.

B. Application to Cygnus X-1

Using the procedure outlined above, a large set of hypothetical emission lines was obtained for the Cygnus X-1 system. The details of the derivation are as follows. From theoretical and observed absorption lines for non-rotating stars with the spectral type of HDE226868 (Auer and Mihalas 1972, Mihalas 1964), the parameters for Hβ were extracted and reduced to an approximate gaussian equivalent ($\Delta\lambda_a \simeq 4\text{Å}$, $D \simeq .2$). Next, the low-mass binary model of Table 1 was used to produce the shifted (quadrature) reference line with $\Delta\lambda_a' \simeq 5\text{Å}$ and $D \simeq .2$. A conservative value of .001 was then chosen for F (the relative secondary continuum strength). Light curve irregularities (cf. Hutchings et al. 1973) may be interpreted as limiting the secondary continuum to less than two percent, whereas Blumenthal and Tucker (1974)

have quoted a figure of one percent as an upper limit. The above choice is indeed conservative. From Figure 3 was taken the value for V_{OB} (=73 km/s) with ΔV_{OB} = 0 (middle asterisk in that figure) at the .25 quadrature. The solution surface was then computed.

In Figures 4-6 are shown examples of the line blends associated with a number of the derived emission lines which illustrate some distortion extremes. In those figures the broadened Hβ reference line appears as a plain line while the blend is represented by a dotted line and has its minimum at the observed line position X_{min} (=0.14). Each blend is labeled by the corresponding emission line parameters: height H (for F = .001), half width W and peak position X_E (=-S). The profile in Figure 4A represents a typical acceptable blend. The blend in Figure 4B was obtained with the same emission line as that in Figure 4A, but with less separation between the blending lines - a subset of the emission line solutions are double-valued in V_e. This profile is on the limits of acceptability due to excessive filling in of the reference line. Such a variation with phase would be readily observable. The Figure 5A profile is at the narrow limit of acceptability while the blend in Figure 5B is unacceptable because it violates continuum intrusion, emission line resolution and filling in requirements. The blend in Figure 6A is formed by an emission line almost too weak to

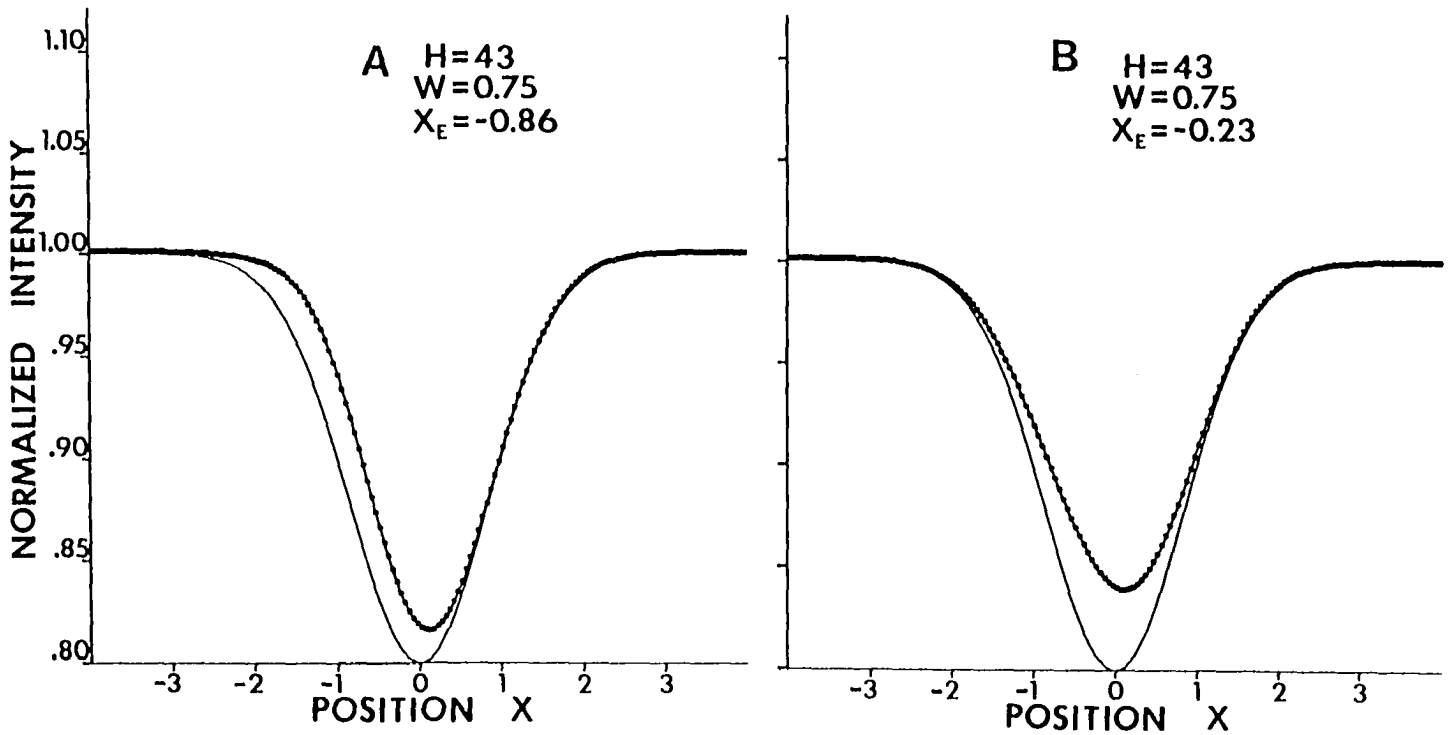

Figure 4. Emission-absorption blend profiles

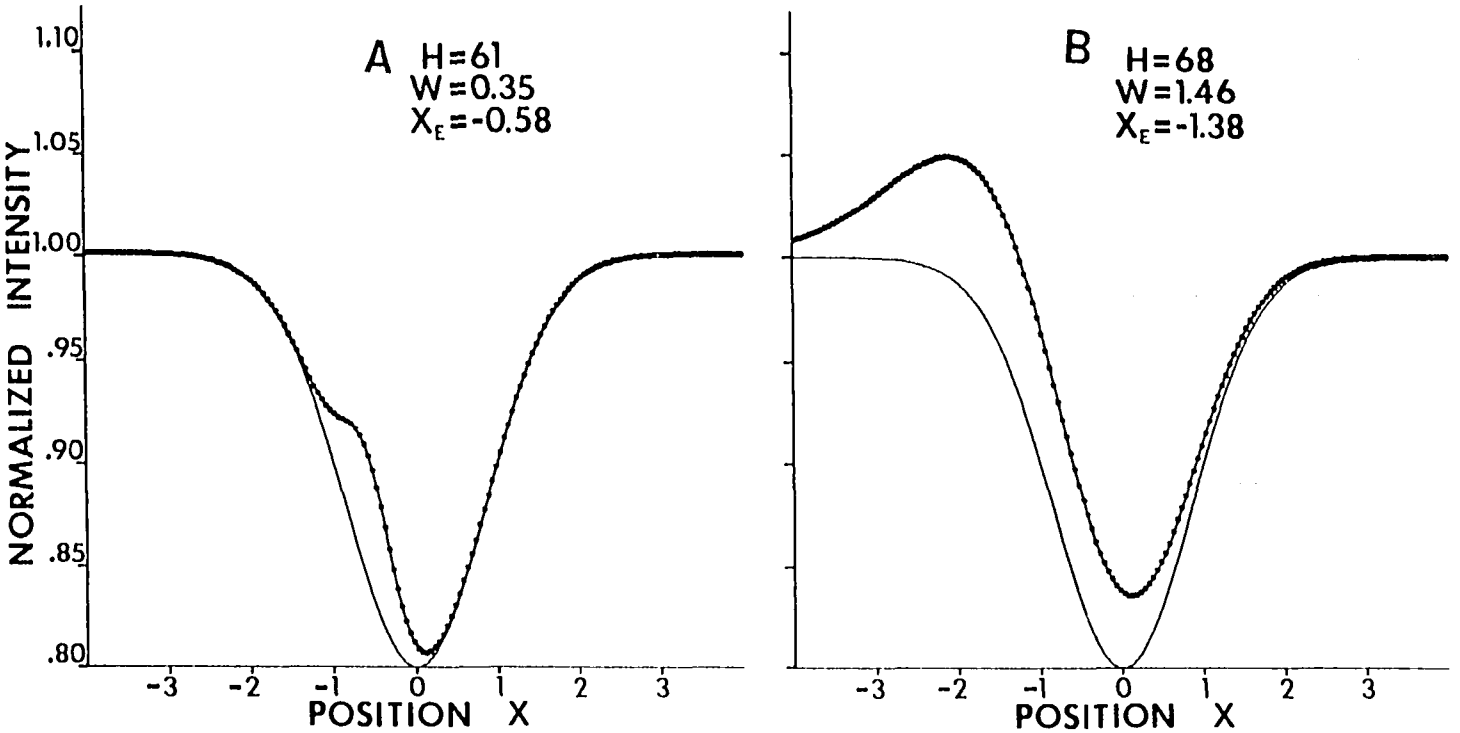

Figure 5. Emission-absorption blend profiles

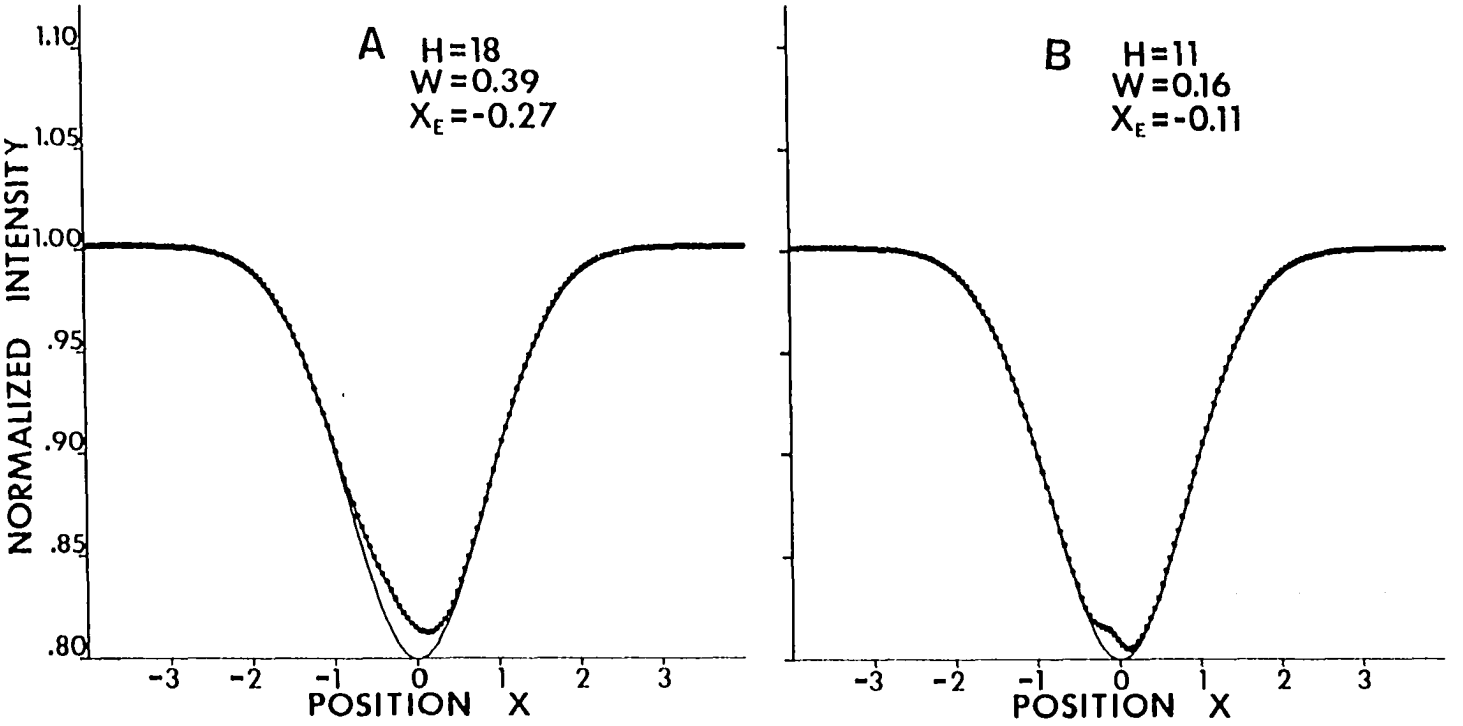

Figure 6. Emission-absorption blend profiles

effect the required shift of line minimum. The Figure 6B profile is on the threshold of rejection due to emission line resolution and will be considered further in Section V. Actual values used in the rejection criteria were as follows: depth change less than 20%, width change less than 20%, equivalent width change less than 30%, and continuum intrusion less than 5%. Emission line resolution was determined using profile slope tests which rejected blends exhibiting a slope sign change between the reference line minimum and a point to the left of the emission line peak for S less than about 1.5. These values are largely empirical and are meant to be only initial estimates although Hutchings et al. (1973) and others (cf. Wolff and Morrison 1974) show profile variations from 30% to 60% for some lines. Recently Bolton (1977) has confirmed the conservative nature of these numbers, feeling that only the blend of Figure 5B, the most distorted of the examples, would be unacceptable in that the emission contamination may be detectable. It must be remembered that profile parameters can only be estimates because actual profiles are not so nicely describable. This gaussian study is intended only to investigate the possibility of an effect and not the details thereof.

It is desirable to study the trends exhibited by the entire set of possible emission lines of which the emission

lines associated with Figures 4-6 are a subset. To facilitate that end, several data display techniques were used. The first representation is shown in Figures 7 and 8. These figures represent a two dimensional display of the emission line solution surface derived above which corresponds to the model of Table 1. Height H and the emission line half width at half maximum (HWHM) define a matrix whose elements represent the results of the search for solutions V_e to Equation (16). The numerical symbols correspond to values of V_e for emission lines whose associated blends survived the distortion limit test. These are the acceptable emission lines, each of which can blend with the reference absorption line subtly enough to escape ready detection and yet which is able to cause enough velocity distortion to effectively mask a low-mass secondary. The correspondence between symbol and velocity range is presented in Table 2. The letter symbols represent the type of distortion excess that caused an emission line to be considered unacceptable as outlined earlier. The explanation of these symbols is also found in Table 2. The rejection symbols are listed in that table in the order in which the corresponding tests were made in the profile testing routine.

The double valued solutions have been separated in these figures for clarity. Figure 7 displays the low-V_e solutions and Figure 8 the high-V_e lines. The continuity evidenced in

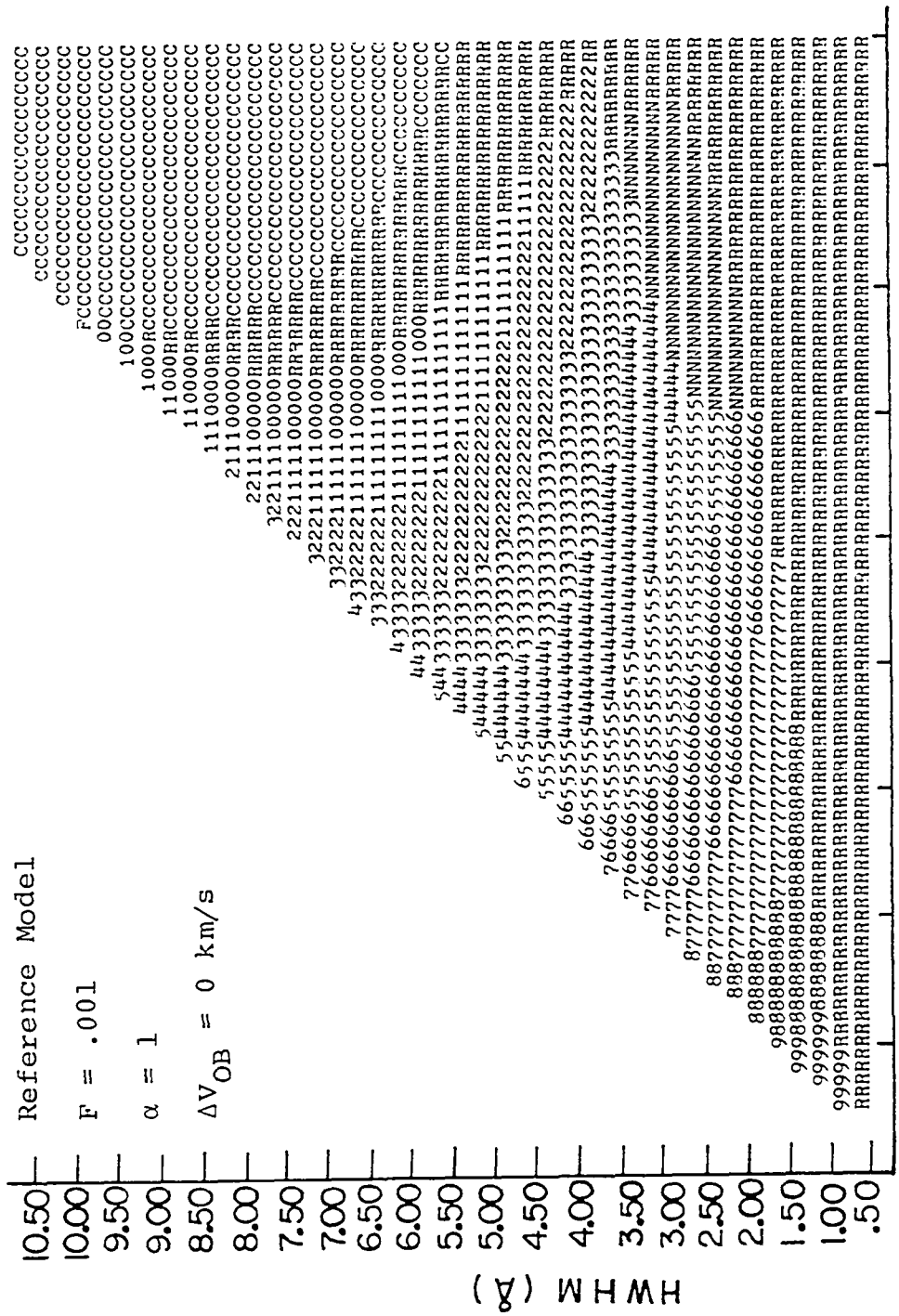

Figure 7. Required emission lines: low-V_e solutions - 2D

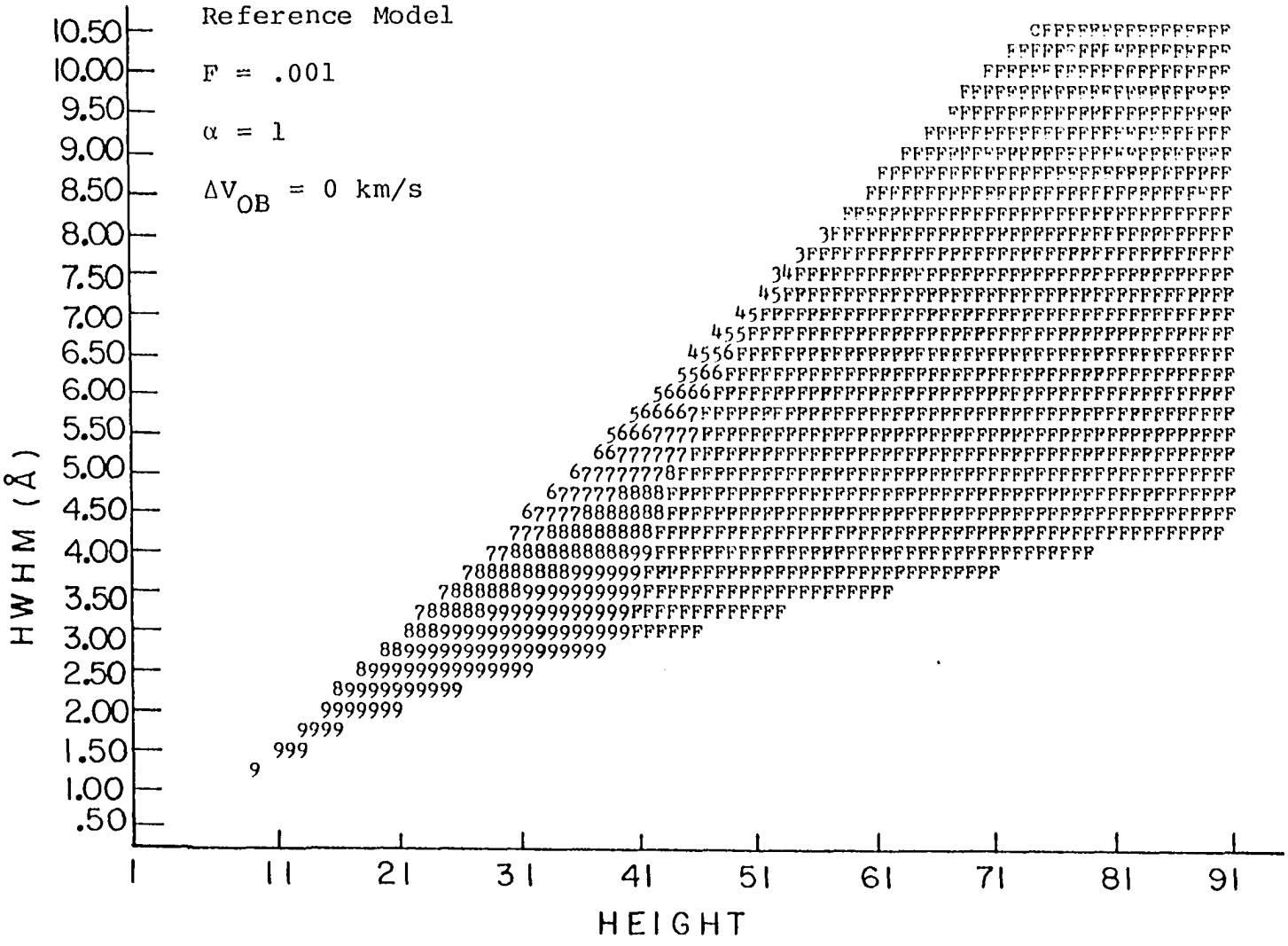

Figure 8. Required emission lines: high-V_e solutions - 2D

Table 2. 2-D display matrix: symbol key

Symbol	Velocity range (km/s)	Symbol	Velocity range (km/s)	Symbol	Violation
0	-323 to -259	5	1 to 66	C	Continuum intrusion
1	-259 to -194	6	66 to 130	F	Filled in
2	-194 to -129	7	130 to 195	R	Resolved emission
3	-129 to -64	8	195 to 260	N	Too narrow
4	-64 to 1	9	260 to 325	A	Small equivalent width

the velocity trends and in the rejection trends confirms the consistency of the numerical techniques. Note that the high-V_e solutions of Figure 8 fit smoothly onto the low-V_e solutions of Figure 7 along the boundary of the solution region. The rejection results behave as expected as well, lending more credibility to the methods used. Invariably, very narrow emission lines are resolved in the blend. Slow lines are resolved outside the blend or intrude above the continuum, depending on their shapes. The fast, broad lines of Figure 8 fill in the reference absorption line too much, as expected for strong emission almost superimposed on the absorption. Note that here "fast" refers to a more positive V_e. Apparently a wide range of emission lines are able to provide the distortion required to allow neutron star models for Cygnus X-1.

Before analyzing this surface any further, another data display technique should be considered. In Figures 9 and 10 are displayed the three-dimensional versions of Figures 7 and 8 with the unacceptable solutions suppressed. The continuity of the surface is clearer in this representation and the behavior of the surface is more easily seen. Subsequent investigation of the solution volume associated with modeling parameter variations will be discussed primarily in the context of this representation. In particular, the effects of such variations will be analyzed in terms of alterations in

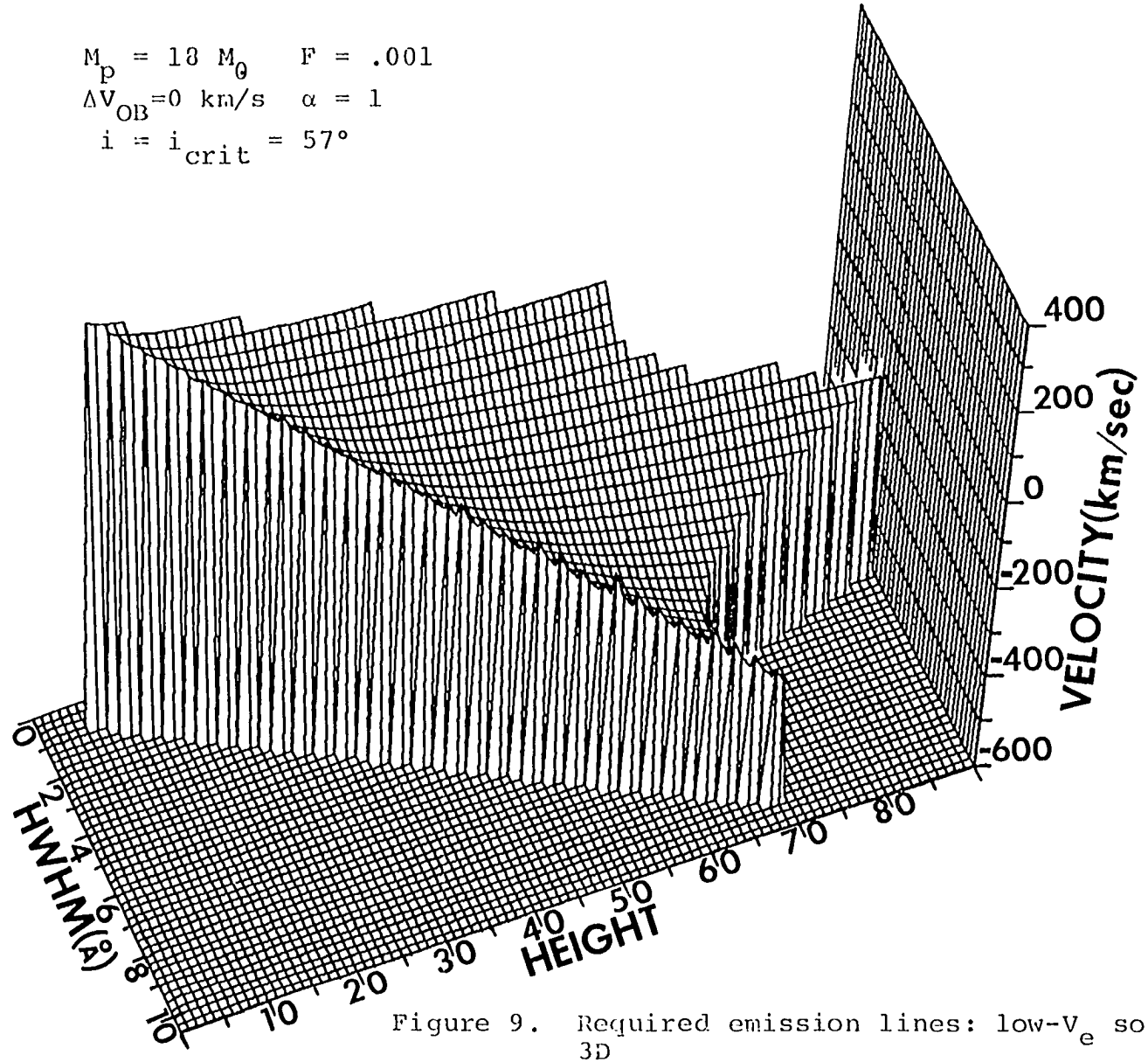

Figure 9. Required emission lines: low-V_e solutions - 3D

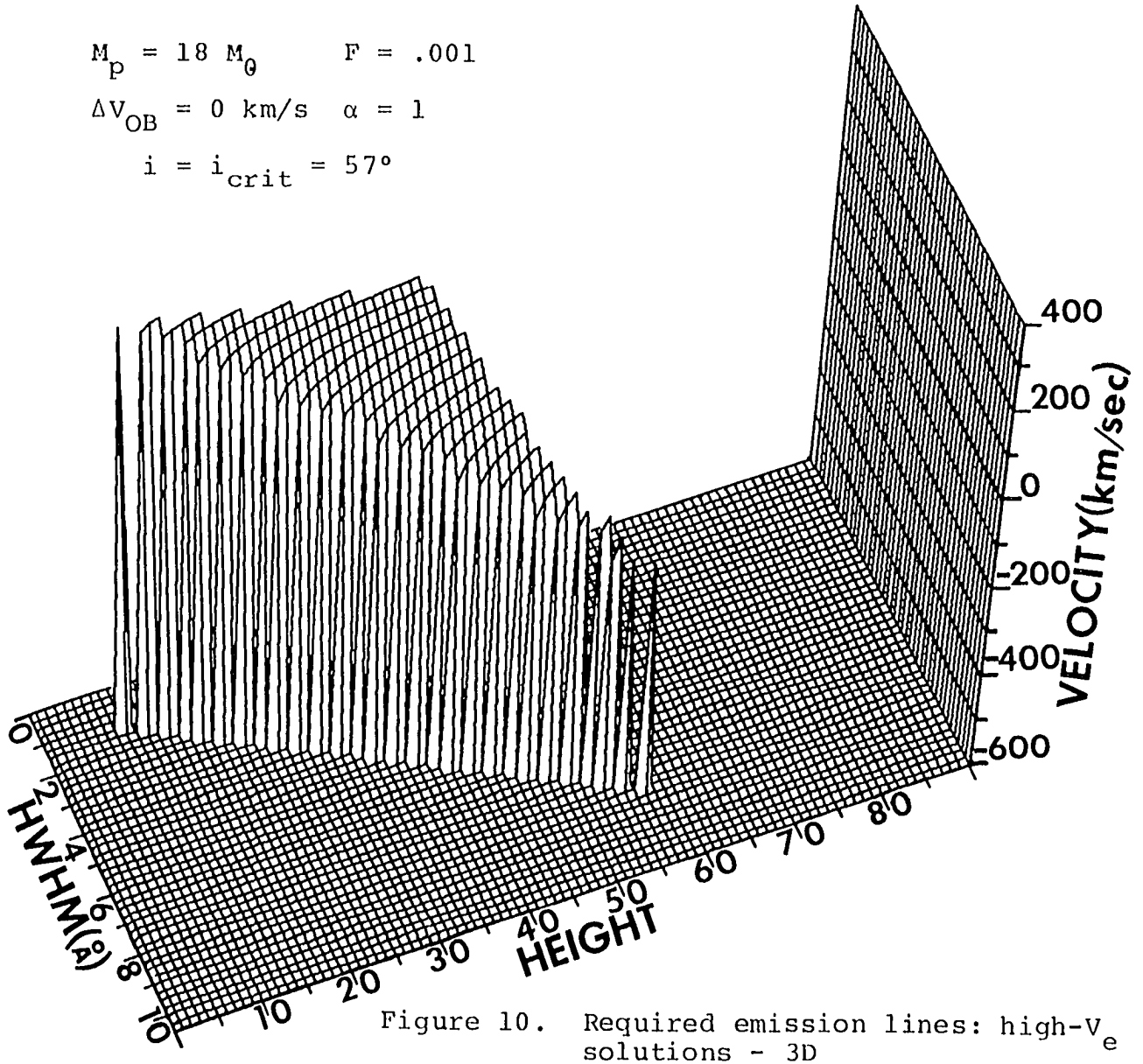

Figure 10. Required emission lines: high-V_e solutions - 3D

the reference surface of Figure 9, the corresponding changes in the associated high-V_e surface of Figure 10 not being discussed unless they are unusual.

The most interesting feature of the surface in Figure 9 (henceforth called the reference surface) is the appearance of negative velocity solutions. Emission lines need not arise in the region between the stars for the appropriate blending to take place. Apparently, fairly wide emission lines can remain undetected and yet still affect the primary line while being significantly separated from it. The significance of this result will be discussed in the next section with respect to the gas flow models it implies.

To test the sensitivity of the reference surface to the choice of modeling parameters - to explore the nature of the solution volume - each of the parameters was sampled within its allowable range and the above procedure repeated to derive a new surface. The results of such tests are displayed in Figures 11-18, only the low-V_e surfaces being shown. Figures 11 and 12 illustrate the power of the relative secondary continuum F parameter in significantly influencing the surface configuration. Variation of this parameter dramatically affects the position of the surface in the H-W plane. The increase of rejection percentage with increasing F is due mainly to the greater frequency of detectable

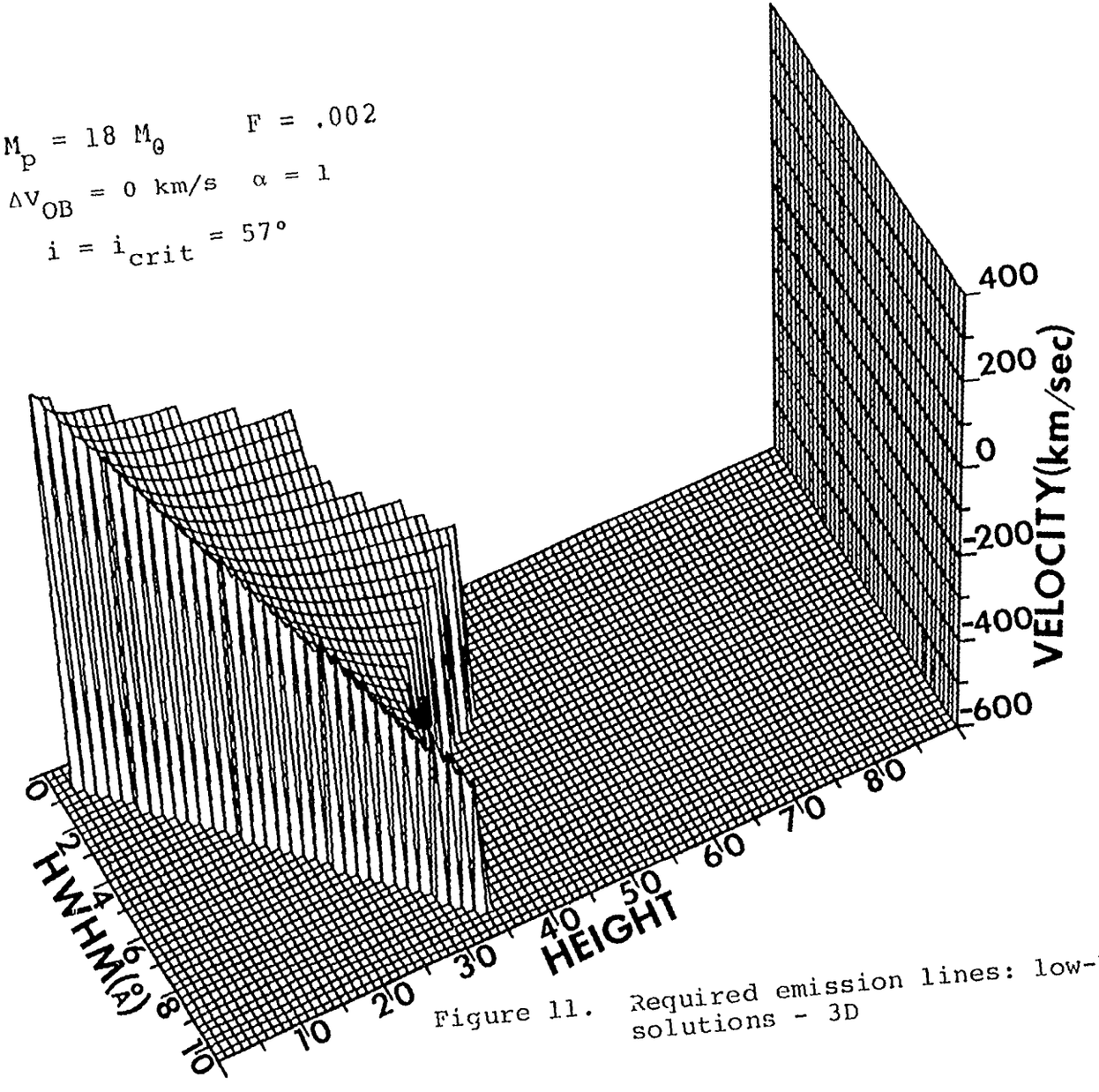

Figure 11. Required emission lines: low-V_e solutions - 3D

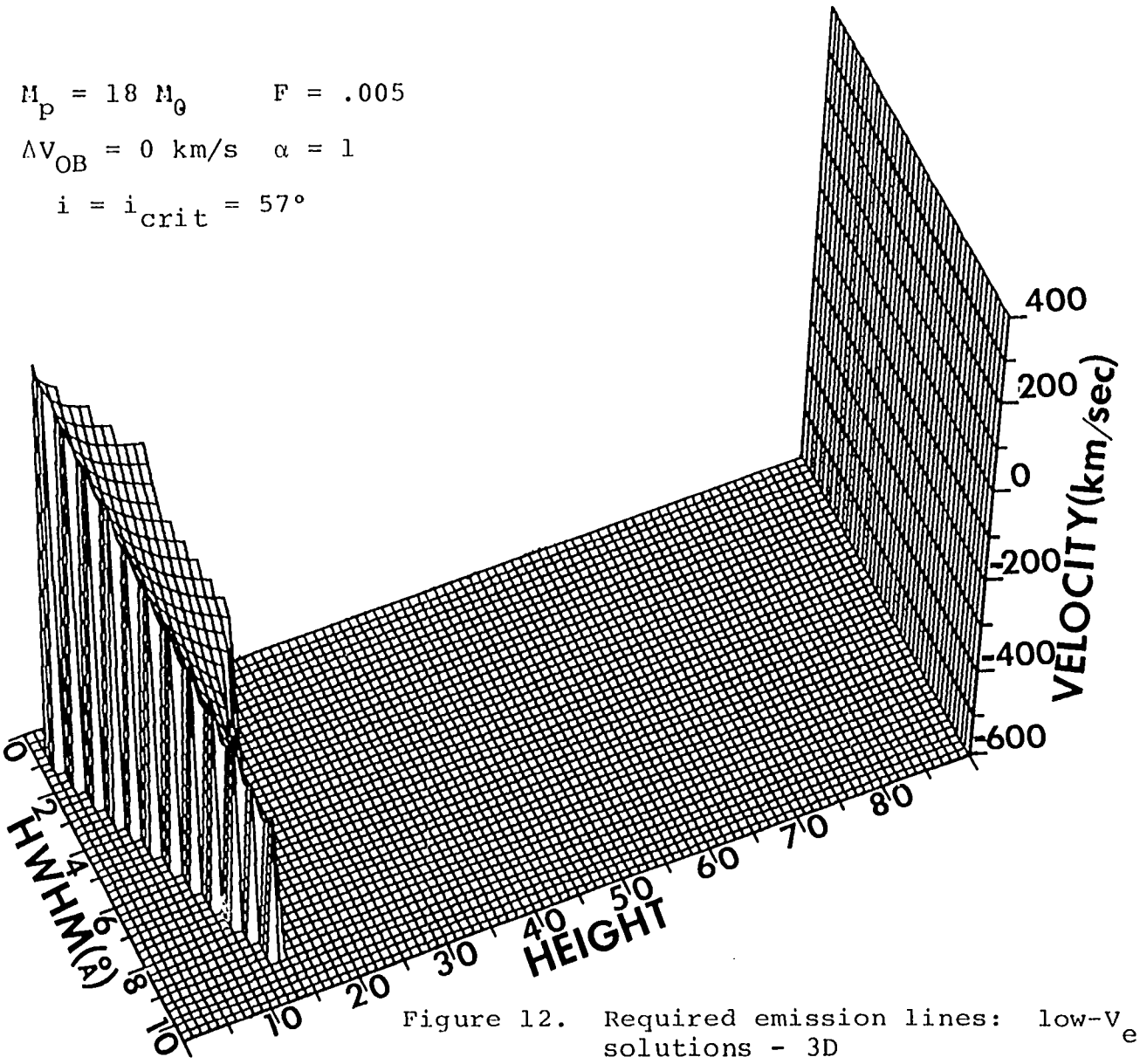

Figure 12. Required emission lines: low-V_e solutions - 3D

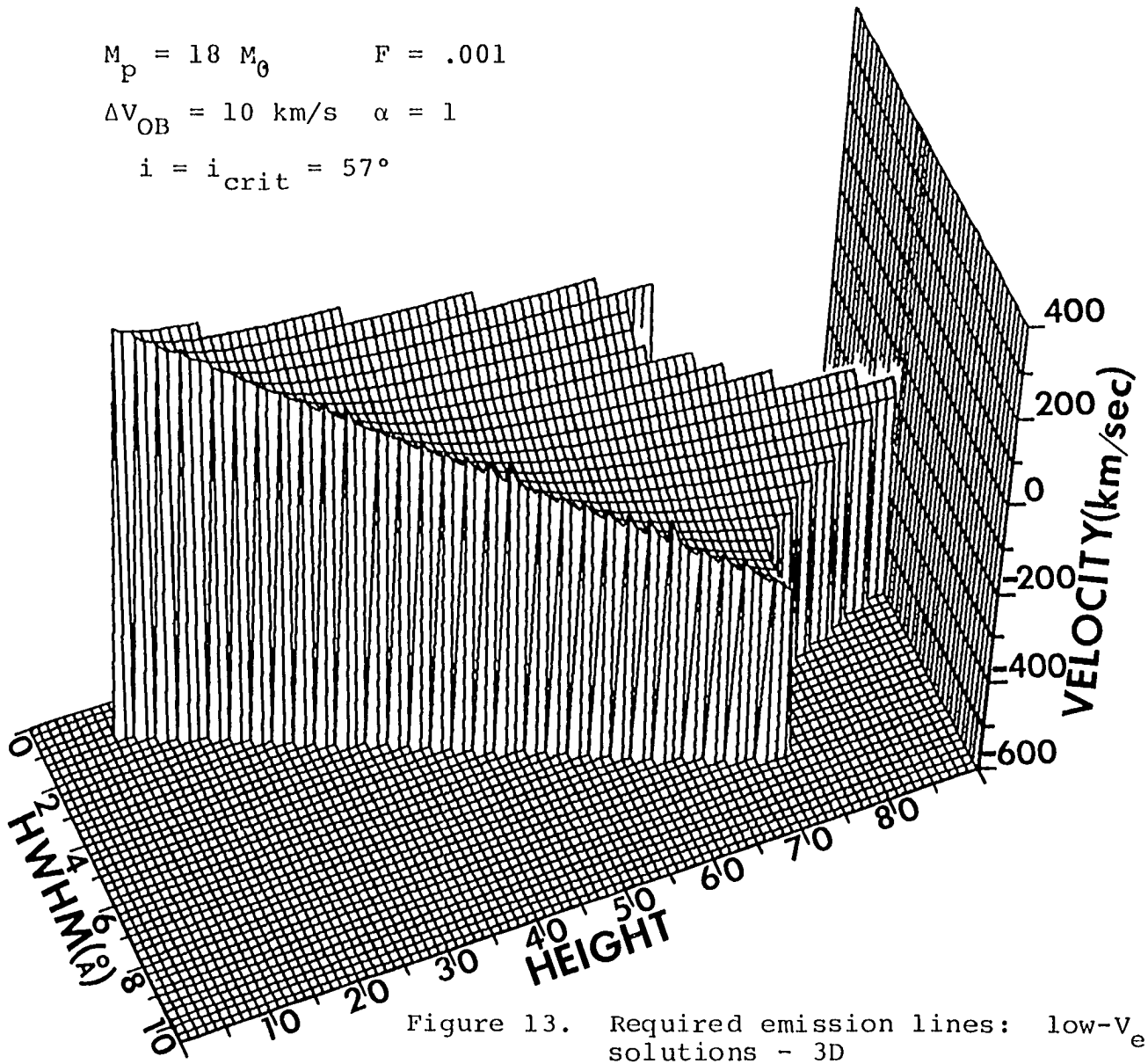

Figure 13. Required emission lines: low-V_e solutions - 3D

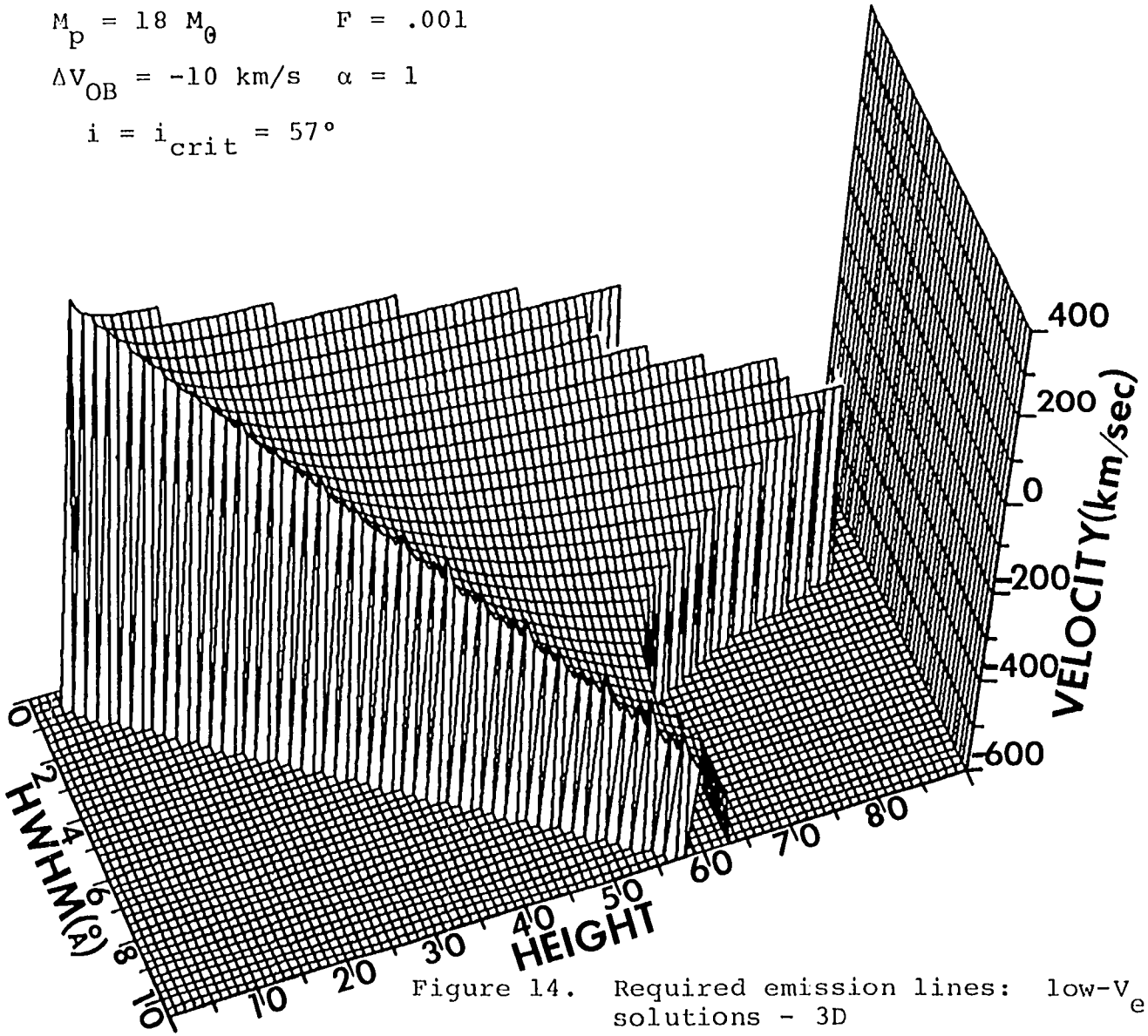

Figure 14. Required emission lines: low-V_e solutions - 3D

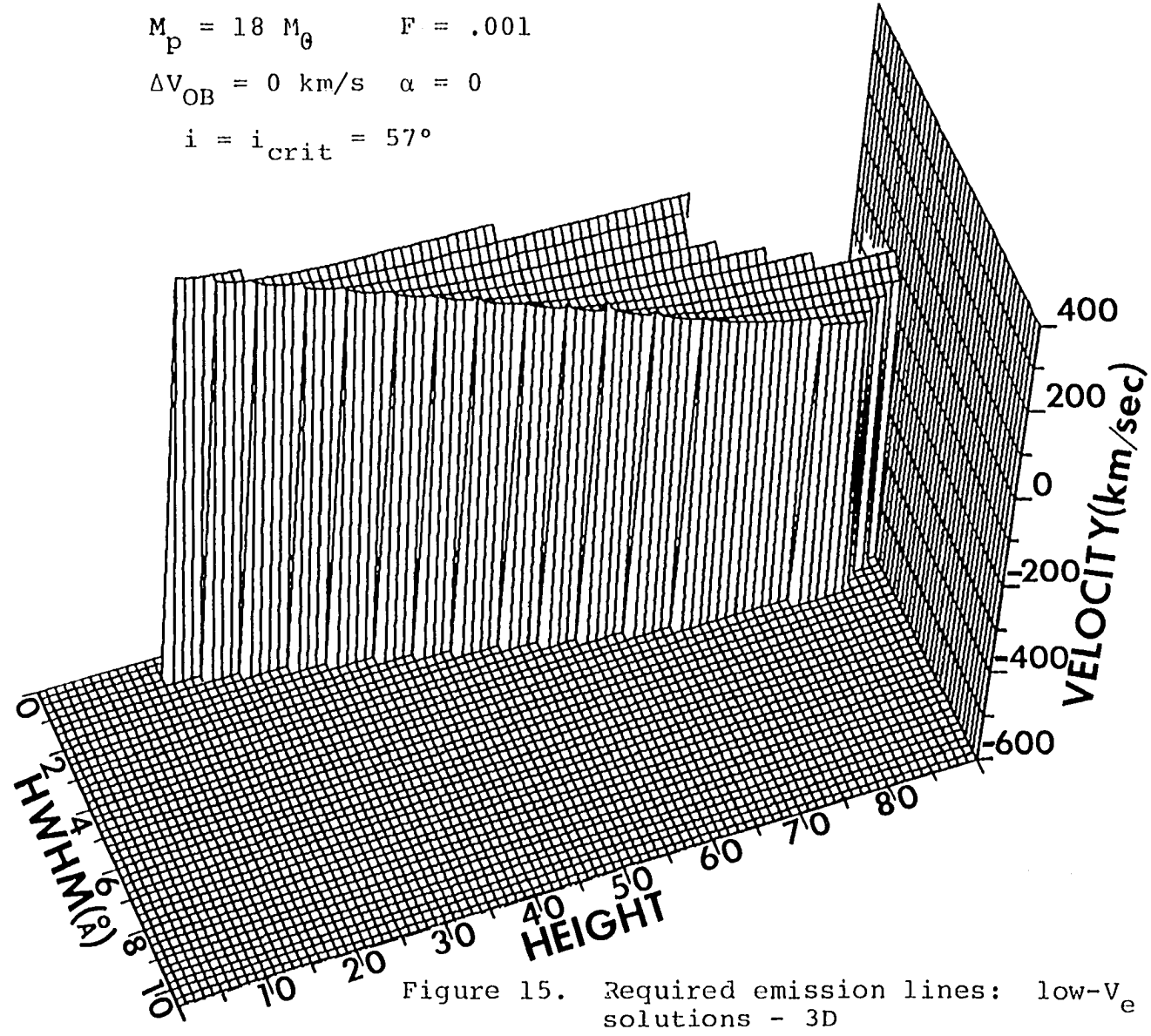

Figure 15. Required emission lines: low-V_e solutions - 3D

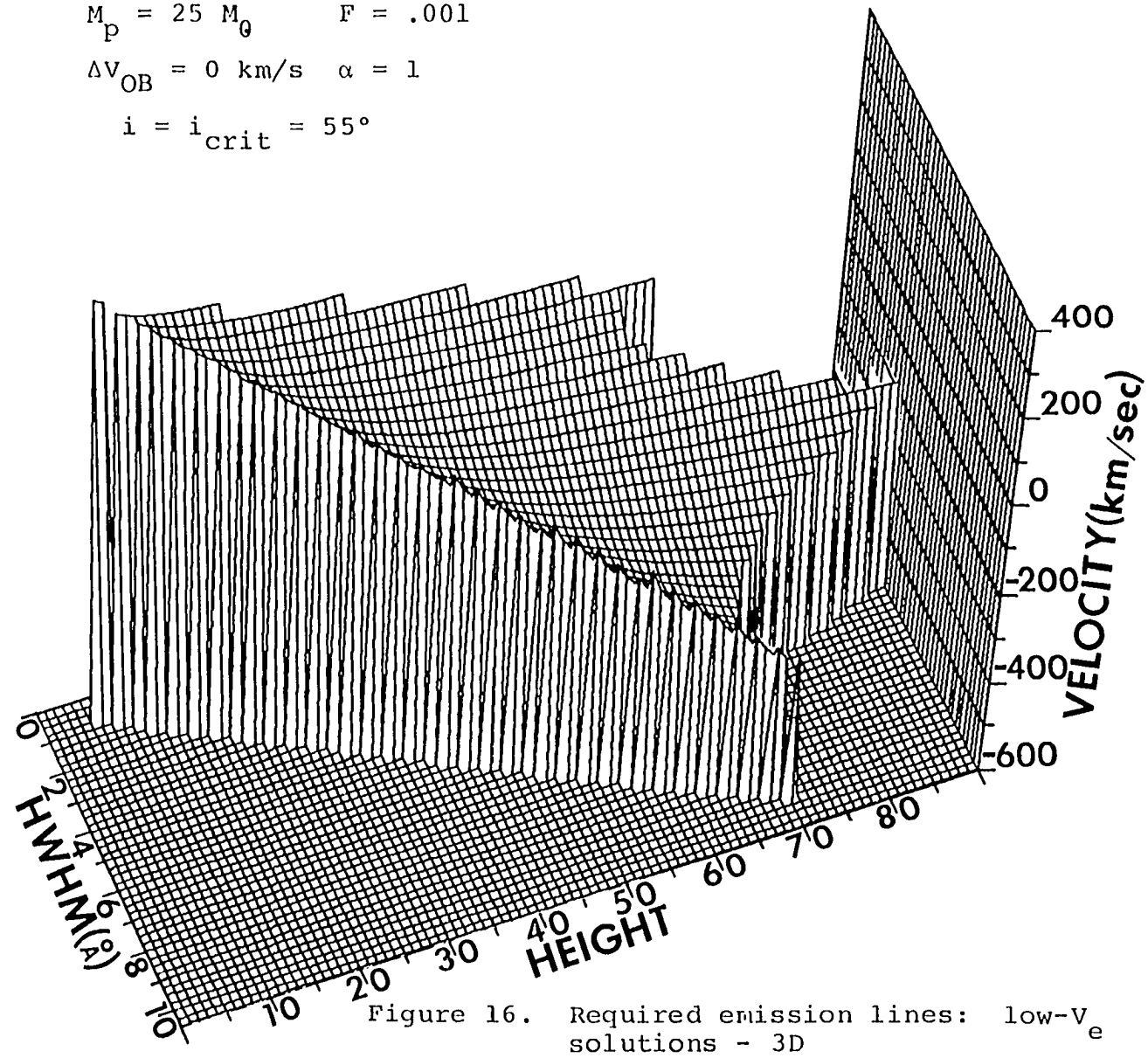

Figure 16. Required emission lines: low-V_e solutions - 3D

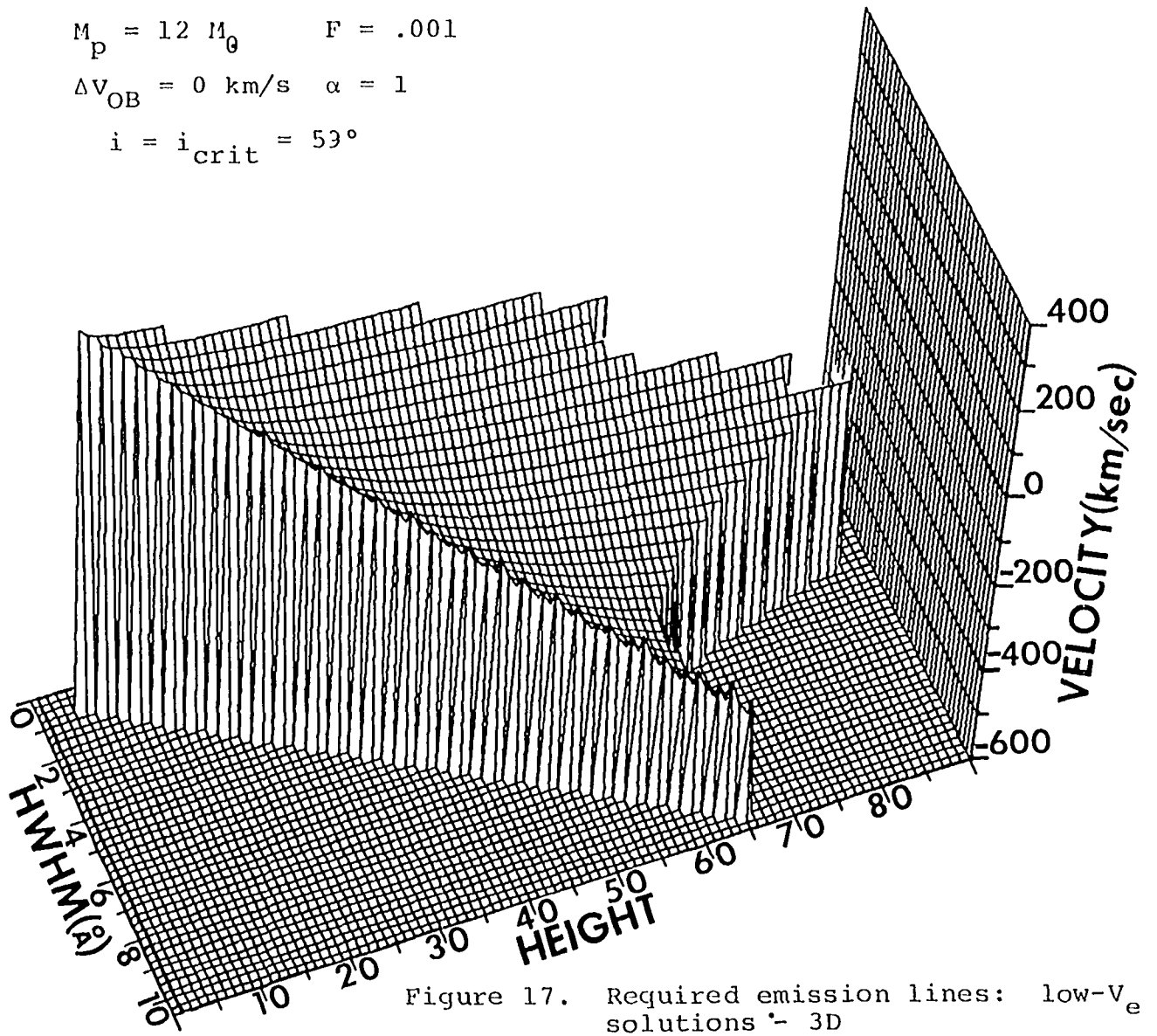

Figure 17. Required emission lines: low-V_e solutions - 3D

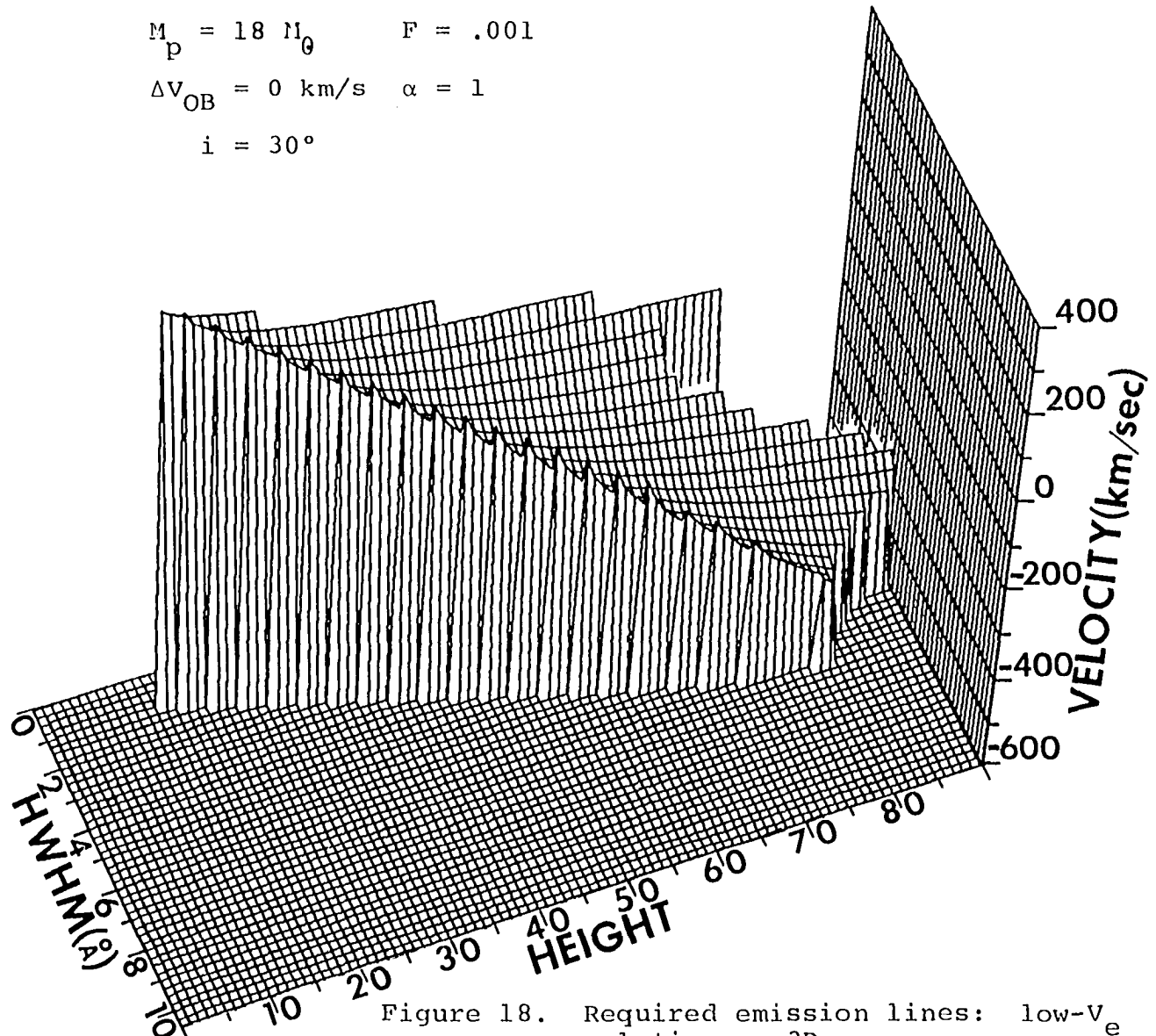

Figure 18. Required emission lines: low-V_e solutions - 3D

intrusion of the emission into the continuum. Such an effect is somewhat artificial in that the continuum used in the rejection test was that of the primary and not the combined continua; consequently higher values of F are improperly discriminated against by this test. For the F values shown in Figures 11 and 12 such an error is small: the trend is real and dramatic. Care must still be taken however, in comparing surfaces of differing F parameter because H is related to F through the maximum allowable emission (α F(1+H), Equation 14), a quantity roughly fixed by the reference absorption line choice and the rejection criteria. Thus, while H decreases markedly in the 3-D plots, the actual flux in the line (α FH) decreases more modestly with increasing F. The general tendency toward shorter, fatter emission lines with increasing F illustrates the enhanced ability of the emission line wing to distort the reference line. If the secondary continuum source is too bright the range of acceptable emission lines becomes very small due to blend distortion. If it is too faint, the range becomes restricted to very high lines, which are more difficult to produce. From Figures 9, 11 and 12 it seems that the blending mechanism requires $-4 < \log F < -2$ to avoid being unsuccessful, or, at least, very contrived.

The range of the parameter ΔV_{OB} - the uncertainty in the

observed velocity curve amplitude - has particular importance in that once a physical model for the system is specified, the surfaces resulting from values at each extreme roughly bound the solution volume for that model. To investigate the nature of this residual volume, this parameter was varied from its value of zero in the above treatment. At the .25 quadrature the values $\Delta V_{OB}^{\pm} = 10$ km/s were considered (asterisks in Figure 3). These choices correspond to the most probable error in the scatter about the curve. In some cases even more extreme uncertainties exist for some points (cf. Hutchings et al. 1973) and a discussion of the possible influence of radiating gas on this parameter will be included in Section V. The results of the new ΔV_{OB} values are displayed in Figures 13 and 14 for the low-V_e surfaces. The case of Figure 14 ($\Delta V_{OB} = -10$ km/s) corresponds to a lower observed velocity curve amplitude (lower asterisk in Figure 3) and as is expected, admits more weak emission lines as acceptable: the disparity between the curves in Figure 3 is lower and therefore more easily explained by weaker emission. The corresponding changes in the line velocities defines a V_e thickness to the volume between the surfaces of Figures 13 and 14 of about 200 km/s, the surface of Figure 9 roughly bisecting this volume.

Figure 15 shows the surface derived by variation of the

rotational broadening efficiency parameter α. The use of $\alpha = 0$ to represent a line unbroadened by primary rotation effectively narrowed the reference line (to $\Delta\lambda_a' \simeq 4\text{Å}$). As expected for a narrower absorption profile, the emission line solutions were shifted to sharper profiles - narrower or higher or both. The velocity components were correspondingly shifted to higher values, the surface becoming flatter and smaller as well. This behavior - the apparent sensitivity of the blending mechanism to absorption line width - may be important for possible observational tests of the mechanism's importance in Cygnus X-1 (Section V).

Other binary system models from the grid generated in Section II were also considered, to test further the range of possible emission lines. Such changes from the reference model parameters of Table 1 effectively alter the sine curve of Figure 3, and modify the reference absorption line as well. Variation of the primary mass M_p within the grid range reasonable for B0 supergiants resulted mainly in a velocity displacement of the solution surface with little effect on H or W positions. A range of 12 to 25 $M_\odot$ generally defined a solution volume of thickness $\sim$100 km/s about the reference surface, the higher M_p value yielding a higher V_e as Figures 16 and 17 show. The trend is as expected since a higher M_p lowers the sine curve amplitude (Equation 1, Table 1), thereby increasing the separation of the curves in Figure 3. Higher

velocity emission lines are then necessary to provide more distortion of the primary absorption line. The range of emission lines is not restricted, as it was for the case ΔV_{OB} = 10 km/s (Figure 13), because the increased rotation of the primary (Table 1) broadens the reference line, producing a compensating effect much like the reverse of the α = 0 trend (Figure 15). Variation of M_x has an effect similar to that produced by changes in M_p, but the V_e shifts are in the opposite sense and are of smaller magnitude.

Finally, the constraint on inclination angle (critical eclipse aspect) was lifted to see how the solution set would be affected by either allowing lower angles or by allowing the higher values possible for a wind accretion model in which the primary is significantly smaller than its Roche lobe. Both of these possibilities will be discussed later. The low inclination grid model (i = 30°) was considered for this purpose (Table 1) and the results are shown in Figure 18. Since this inclination reduces both the sine curve amplitude (Figure 3) and the rotational velocity of the primary, a combination of the effects seen in Figures 13 and 15 is to be expected. Indeed, Figure 18 shows the surface shape of Figure 13 with the truncation in the W direction characteristic of Figure 15. The smaller size of the i = 30° surface indicates that if the low inclination can be verified by independent means, even

the blending mechanism may be unable to explain Cygnus X-1's apparent high mass, at least for wider emission lines.

The efforts of this section have produced a wide range of emission lines capable of interfering subtly with the accurate mass determination of Cygnus X-1. It should be emphasized that parameter choices made here have been conservative with respect to the production of emission and its subsequent blending properties. The derived blends are "noise-free" and so represent the case of most detectable distortion. Inclusion of photon noise to obtain more realistic profiles would further extend the range of emission lines able to satisfy the blending requirements. This section has also seen the identification of effects sensitive to observations (blending sensitive to primary line width). We now must consider whether or not any of these lines are to be expected physically in an X-ray binary containing an early primary. The discussion above has also illustrated some guidelines for use in selecting gas flow models for this continued inquiry (e.g., limits on F).

IV. GENERATION OF PHYSICALLY EXPECTED EMISSION LINES

A. Gas Flow Models in Emission: Theory

The intention of this section is to describe emission lines of Hβ produced by gas whose state is defined by the environment of the Cygnus X-1 system, specifically, by the environment of the reference model for that system described in Table 1. Comparison of these lines with the lines derived in Section III will be discussed in the next section in an effort to evaluate the potential significance of the emission-absorption blending mechanism.

Models for these regions of gas flow are hardly unique. Many of the modeling parameters are not well-determined. The nature of the gas flow derives from such parameters as source and rate of mass transfer, stream viscosity, stellar wind strength and the luminosity, magnetic field and rotation of the accreting object. It is also influenced by the radiation field of the binary pair. Adjustment of these parameters yields a wide spectrum of gas flow models generally fitting the X-ray observations and satisfying the few general constraints on visible radiation, but widely varying in the nature of the predicted visible line spectrum (cf. Pringle and Rees 1972). However, within the general constraints for these models, the plausibility of

producing emission lines similar to those described in Section III can still be discussed. In fact, the results of Section III provide guidelines for the choice of one such gas flow model for initial consideration.

The requirement that the velocity distortion mechanism be sinusoidal and in phase with the primary's absorption spectrum in order to maintain the symmetry of the radial velocity curve, limits the gas flow models for this study. Models which can produce such an effect with contaminating emission lines should have a geometry which is symmetric about the line of centers. Emission region models not having this symmetry would produce an unobserved spurious eccentricity in the radial velocity curve if blending was significant, and would produce unblended emission lines if it was not. In particular, the initial gas stream occupying the trailing hemisphere of the secondary Roche lobe (see Figure 1) will not be considered in this inquiry. Presumably this stream adequately explains the origin and phase behavior of unblended helium and hydrogen emission as mentioned earlier (e.g., Bolton 1975a). Consideration of disk or partial disk models will therefore guide this search for contaminating emission lines. These models are also more likely to be stable than stream models (cf. Bolton 1975a), a quality desirable in light of the apparent constancy of the observed

radial velocity curve amplitude over long time scales. The size of such an emitting region is determined by the many free parameters mentioned above. Once a mass distribution is defined, its emission properties may be sensitive to the stimulating radiation of the two stars. For example, if the X-ray source dominates in exciting the gas to emission, a full disk would contribute to such emission. If the supergiant becomes important in producing emission in the gas, the substellar hemisphere may be favored in its emission strength.

Assuming that the emission region is defined by gas having a Keplerian orbit about the secondary allows further restrictions on which flow models might produce the required emission lines of Section III. The Keplerian approximation is chosen for simplicity and is good near the secondary. A discussion of possible modifications of this restriction will be included in Section V. Figure 19 illustrates the velocity field for circular Keplerian orbits about a two solar mass object. The velocity magnitudes displayed may be compared directly with the emission line velocities as they were computed using the same coordinate system (velocities shown are the orbital plane component of the radial velocities measured with respect to the secondary at the .25 quadrature). In that figure, R_s is the radius of the secondary Roche lobe for the reference model of Table 1 (=7 $R_\odot$), and the curves

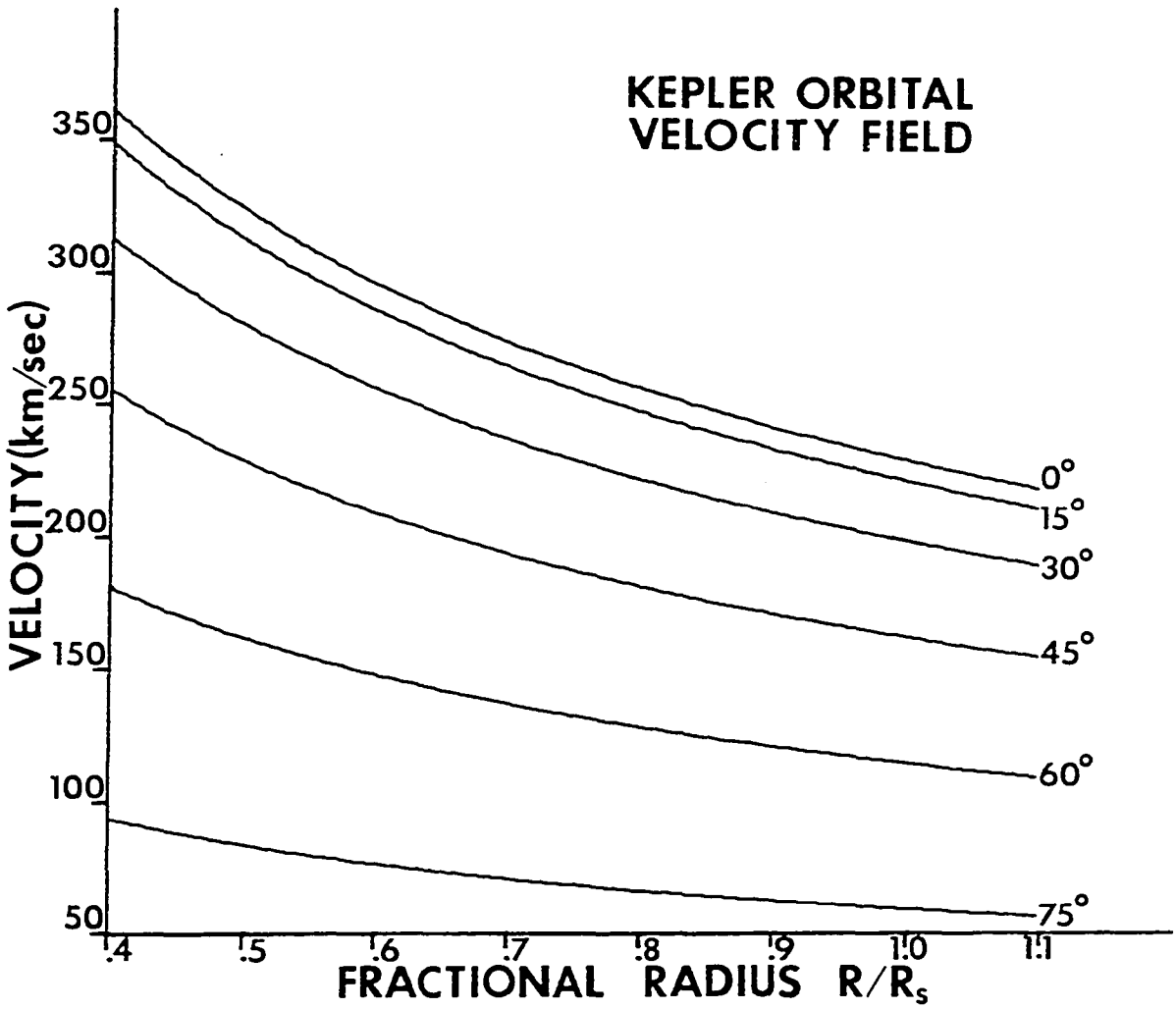

Figure 19. Velocity field for circular Keplerian orbits for the reference model

are labeled by a position angle measured in the orbital plane from the line of centers. Note that Figure 19 displays only velocity magnitudes, and that for the coordinate system defining V_e, positive values correspond to Keplerian velocities in the substellar hemisphere while negative velocities represent that part of the orbit in the other hemisphere.

From Figure 19 we first notice that the range of velocities available to a Keplerian disk in the reference model system (Table 1) readily contains the range of required emission line velocities V_e of Section III (e.g., Figure 9). Such a model disk need not extend unusually close to the central object to accommodate those required velocities. Generally these disk models associate positive velocities (substellar hemisphere emission) and negative velocities (outside hemisphere emission) with relatively narrow emission lines since the emitting region is roughly localized to a region of limited velocity dispersion. On the other hand, emission arising from a region symmetric about the secondary (whole disk emission) would generally be characterized by wider lines, and velocities closer to zero. This trend is only partially mirrored in the nature of the emission lines of Section III. From Figure 9, for example, we see the general association of more positive velocities with narrower lines; however, this trend is true even in the negative V_e domain, unlike the trend expected from simple Keplerian disk

models (above). The conclusion is that emission from a whole disk or from the portion of a disk in the substellar hemisphere should be the focus of the first gas flow models considered. Models in which emission arises from the outer hemisphere, yielding negative V_e emission lines, may still be possible. For example, if shock heating from wind accretion put that region into emission, the associated turbulence could produce fairly wide lines. Also, these arguments are only relative: widths have not been estimated yet for comparison with the numbers of Figure 9, although it seems difficult for even Keplerian dispersion to produce the wider lines in that figure. So the widths of lines produced in the outer hemisphere may be acceptable. However, the most promising model for first consideration is that in which the radiation field peculiar to these binaries puts the substellar portion of an accretion disk into emission, the resulting lines being relatively narrow and the line velocities being roughly 200-300 km/s (Figure 19). By considering only this model initially, we are in effect testing the feasibility of producing only the narrow, positive V_e lines in Figures 9-18.

The geometry of this basic gas flow model is shown in Figure 20 and is taken to be a section of a ring of constant thickness located between the stars and having a Keplerian velocity field about the secondary. In the context of this working model, we consider a radiation dominated, optically

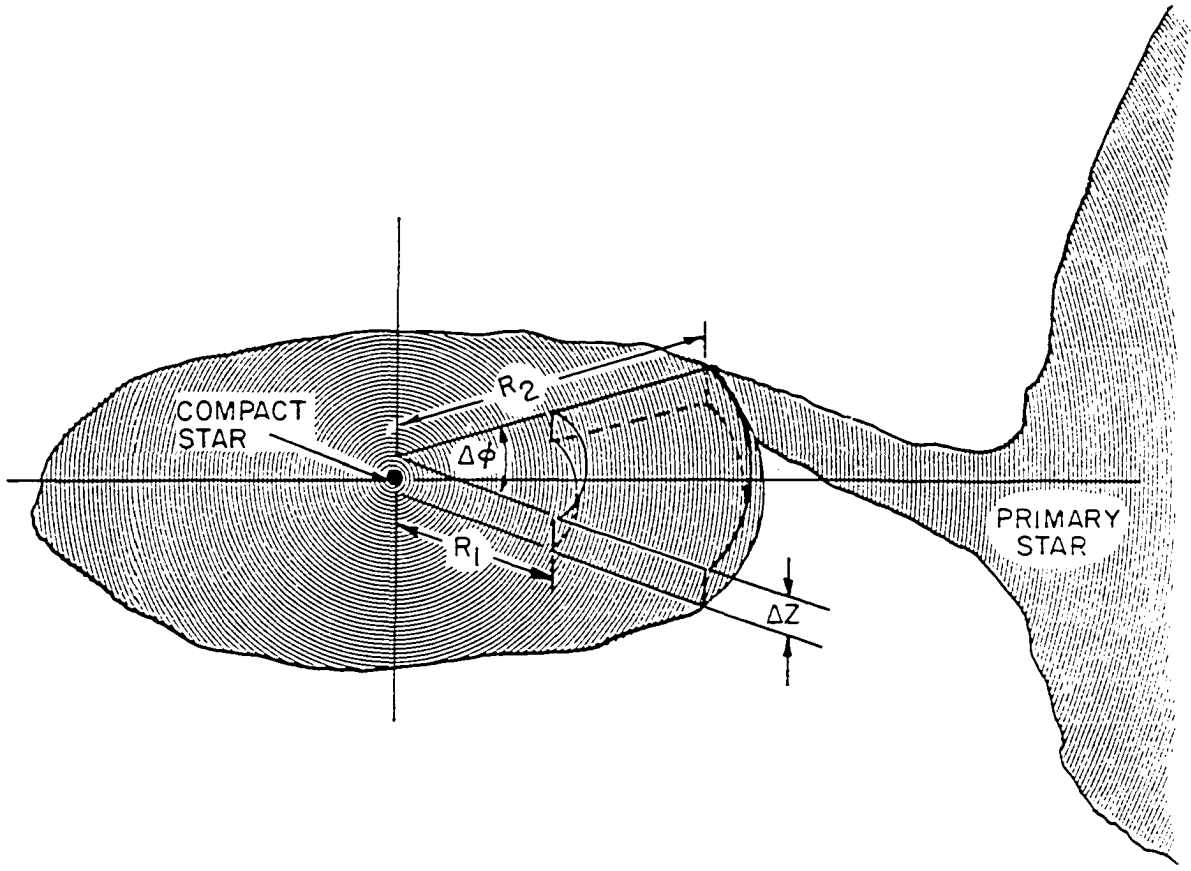

Figure 20. Gas flow model geometry

thin hydrogen gas irradiated laterally by a B0 supergiant (dilution factor W_1 and effective temperature (T_1) and a hot X-ray source (W_2, T_2). The gas is assumed to be isothermal (electron temperature T_e) and of uniform density (electron number density $N_e \simeq$ hydrogen number density N_H). Keeping in mind the inherent limitations of the gaussian line approximation, we seek only order of magnitude estimates or reasonable limits for the emission line parameters produced by this gas. We cannot hope for strict self-consistency in this investigation as even symmetric emission profiles are not expected from these models, much less gaussian lines. Therefore a detailed treatment of the radiative transfer problem for these models is unjustified; moreover, the assumption of a thin, radiation dominated gas explicitly demands this approximation.

Two methods of increasing sophistication, are used to estimate the emission line parameters for this gas. For the preliminary estimate, few of the free parameters defining these gas models are specified. Only the cloud model parameters T_e and N_e and the cloud radiation environment parameters W_1, T_1, W_2, T_2 are set. The gas is assumed to have a uniform source function (no velocity field) and an isotropic radiation field. The only geometric parameter specified is a characteristic line of sight dimension. Solution of the statistical equilibrium equations for the nonthermodynamic

equilibrium atomic level populations then leads to estimates of emission line height H and width W for various line opacity and emissivity profiles. The gas volume required for a relative secondary continuum strength F equal to .001 is also estimated. For this choice of F, the height and width estimates can be compared directly with those of the positive V_e lines in Figures 9 and 10 (and in Figures 13-18 as well, since these estimates are insensitive to the choice of the modeling parameters of Section III).

Analysis of the results of this model (below) encouraged the extension of this treatment to explicitly take into account the Keplerian velocity field and the shape of the chosen gas model (Figure 20). In this latter approach, the geometry is completely specified and the relative continuum strength F is computed along with the detailed emission profile. The emission region mass and luminosity are also calculated. These parameters must be consistent with the required accretion rate and the available energy sources respectively. The resulting emission profiles are then reduced to various gaussian equivalents for comparison with the lines of Section III. This second method of emission line estimation was applied to several choices of gas parameters (N_e, T_e) and to many geometric variations to explore the sensitivity of the results to each parameter. Throughout the line derivation procedure, checks were maintained on the validity of the

initial assumptions. The consequences of some resulting inconsistencies are dealt with in Section V.

The details of these two emission line estimation schemes are as follows. The methods have in common the calculation of level populations and the consequent opacities and emissivities. To this end, the level populations are estimated using a computer program written to solve the statistical equilibrium equations for the first n bound states of a hydrogen atom and the continuum. Only T_e, N_e, T_1, W_1, T_2, W_2 and n are specified for this calculation. Collisional and radiative rates of excitation, deexcitation, ionization and recombination are computed from expressions given by Jeffries (1968) and the radiation field integrals are handled numerically by the program. The derived populations are taken to be constant in accord with the thin (single scattering) gas approximation made above. The opacities and emissivities included in the investigation were as follows. The subscripts c, ℓ, t used below refer to continuum, line, and total (line plus continuum) contributions respectively.

1. The opacity

For the opacity (κ) we use $\kappa_t = \kappa_\ell + \kappa_c$ and assume κ_c is constant over the line. The continuum opacity includes free-free, bound-free and electron scattering contributions as

follows. The free-free opacity is

$$\kappa_{ff} = 4.10 \times 10^{-21} g\ T_e^{-1/2} \lambda^3 N_e N_H [1-\exp(-hc/k\lambda T_e)]\ cm^{-1} \quad (17)$$

(cf. Allen 1973). Here g is the Gaunt factor. The bound-free contribution was computed at the absorption edge of the line from

$$\kappa_{bf} = a_{\lambda 0} N_i\ cm^{-1} \quad (18)$$

where N_i is the number density of atoms in the absorbing state labeled by total quantum number i and $a_{\lambda 0}$ is the absorption edge cross section for photoionization from this level:

$$a_{\lambda 0} = 7.91 \times 10^{-18}\ gi\ cm^2 \quad (19)$$

(cf. Allen 1973). For electron scattering, the Thomson cross section σ was used, so

$$\kappa_{es} = \sigma N_e = 6.65 \times 10^{-25}\ N_e\ cm^{-1}. \quad (20)$$

The line opacity is written as

$$\kappa_\ell(\lambda) = \lambda^4 N_i A_{ji} (g_j/g_i - N_j/N_i) \phi_\lambda / 8\pi c. \quad (21)$$

Here subscripts refer to lower (i) and upper (j) level quantum numbers for the transition, A_{ji} being the Einstein rate coefficient for spontaneous emission in the line. Statistical weights are represented by g and level populations by N. The normalized absorption profile ϕ_λ ($\int_0^\infty \phi_\lambda d_\lambda = 1$) is taken

to be gaussian with half width W_0:

$$\phi_\lambda = [(\ell n\ 2)/\pi W_0^{\,2})^{1/2} \exp[-(\ell n\ 2)(\lambda-\lambda_0)^2/W_0^{\,2}]. \qquad (22)$$

2. The emissivity

For the emissivity (j) we use $j_t = j_\ell + j_e$ and assume j_e is constant across the line. The continuum emissivity includes recombination and free-free contributions as follows. Recombination emissivity (free-bound) was written as

$$j_{fb} = 2.16 \times 10^{-22}\ T_e^{-3/2}\ N_e N_H \sum_n n^{-3} g_n \exp[-(hc/\lambda - \chi_n)/kT_e] \text{ergs sec}^{-1}\ \text{cm}^{-3}\ \text{ster}^{-1}\ \text{Å}^{-1} \qquad (23)$$

where χ_n is the ionization potential of level n and g_n its Gaunt factor. The summation is over all levels contributing to radiation at λ (Kaplan and Pikelner 1970). The free-free contribution is

$$j_{ff} = 6.91 \times 10^{-28}\ g T_e^{-1/2}\ N_e N_H \exp(-hc/\lambda kT_e) \text{ ergs sec}^{-1}\ \text{cm}^{-3}\ \text{ster}^{-1}\ \text{Å}^{-1} \qquad (24)$$

(Allen 1973). The line emissivity is written as

$$j_\ell = hcN_j A_{ji} \chi_\lambda / 4\pi\lambda \qquad (25)$$

(cf. Jeffries 1968) where the normalized emission profile

χ_λ ($\int_0^\infty \chi_\lambda d\lambda = 1$) is taken to have the same form as the opacity profile ϕ_λ. This approximation is discussed in Section V. Values for the A_{ji} required above and in the collisional and radiative rate equations are taken from the tables of Wiese et al. (1969) and Gaunt factors are taken as unity.

3. The profile

To facilitate comparison with the previously derived lines, the emission profile is written as:

$$H(\lambda) = (\mathfrak{F}_t/\mathfrak{F}_c) - 1. \qquad (26)$$

In this section the subscripts "total" and "continuum" refer only to the emission source associated with the secondary component and are therefore understood to be related to the quantities of Section III by the equivalence $\mathfrak{F}_t \equiv \mathfrak{F}_e$, $\mathfrak{F}_c \equiv \mathfrak{F}_2$. The two methods described above use the computed opacities and emissivities in different ways to estimate the emission line parameters H, W, V_e from Equation (26).

a. Case 1 Only H and W are estimated in this first case, V_e being a typical Keplerian velocity extracted from Figure 19. For a cloud of uniform source function, isotropic radiation field and line of sight dimension s, Equation (26) becomes

$$H(\lambda) = (I_t/I_c) - 1 = \frac{S_t[1-\exp(-\tau_t)]}{S_c[1-\exp(-\tau_c)]} - 1 \qquad (27)$$

with

$$S_t = (\kappa_c/\kappa_t)S_c + (\kappa_\ell/\kappa_t)S_\ell. \qquad (28)$$

This follows from the formal solution to the transfer equation. Here I is intensity, S is the source function (= j/κ), and τ is the optical depth (= κs in the present approximation).

Equation (27) can also be expressed as

$$H(\lambda) = \frac{\kappa_c[1-\exp(-\tau_t)]}{\kappa_t[1-\exp(-\tau_c)]}(1 + j_\ell/j_c) - 1 \qquad (29)$$

from which a rough profile can be generated for some choice of W_0 in ϕ_λ and χ_λ (e.g. Equation 22). In this case H = $H(\lambda_0)$.

b. Case 2 To take into account the nonuniformity of the source function and the details of the disk geometry and rotation, Equation (26) must be evaluated in parts. If the radiation field is isotropic in the gas we write

$$\mathfrak{F}_t = (1/d^2)\int_A\int_\tau S_t(\tau)\exp(-\tau)\,d\tau dA \qquad (30)$$

where d is the distance to the observer and the integrations are over optical depth and the projected area A of the cloud. A similar relation holds for $\mathfrak{F}_c$. In the present

approximation the level populations are constant; however, S and κ are now functions of position in the disk because of the dispersion introduced by the Keplerian velocity field. For convenience we consider the M_x-centered cylindrical coordinates $r\phi z$ associated with the Cartesian system xyz where y increases along the line of centers toward the primary and x is also in the orbital plane, increasing in the direction of the orbital motion of the secondary. Thus

$$\mathfrak{F}_t = (1/d^2) \int_{R_1}^{R_2}\int_{\phi_1}^{\phi_2}\int_{z_1}^{z_2} j_t(r,\phi,z)\exp[-\tau(r,\phi,z)]\,rdzd\phi dr \tag{31}$$

where R_1 and R_2 are the inner and outer radii of the disk section and z measures its thickness. Here $\tau(r,\phi,z) = \int_a^b \kappa_t dx'$ where x' denotes the line of sight and b is the point where the line of sight from $a(r,\phi,z)$ intercepts the surface of the cloud nearest the observer. Since the models considered allow the line of sight to intercept the cloud surface more than twice in places, the τ integration may have to be done in pieces. The new positional dependence of S and κ is expressed as an alteration of the profiles ϕ_λ and χ_λ. For example, in Equation (22) λ_0 is replaced by λ_0' where

$$\lambda_0' = \lambda_0(1-V_\ell/c). \tag{32}$$

Here V_ℓ is the local radial velocity of the gas as expressed in the Cartesian line of sight coordinate system x'y'z' (dy'dz' = dA). For the .25 quadrature x'y'z' is just a rotation of xyz around y and we have

$$V_\ell = (GM_x)^{1/2} \sin i \sin \phi \, r^{-1/2} \tag{33}$$

$$= (GM_x)^{1/2} \sin i \, y' [(\sin i \, x' - \cos i \, z')^2 + (y')^2]^{-3/4}. \tag{34}$$

The first form (Equation 33) is used in the modification of the emissivity profile χ_λ since the rϕz coordinate system is convenient for the numerical evaluation of the flux integral in which the emissivity appears (Equation 31). The second form (Equation 34) is used in the modification of the absorption profile ϕ_λ since the line of sight coordinates are convenient for the optical depth integration. The four-fold integration for total line flux was done numerically with gaussian quadrature techniques. The resulting profile (Equation 26) was then fit with various gaussian profiles yielding estimates for effective emission line parameters H, W and V_e. This treatment should reveal which flow configurations - if any - can be expected to produce emission lines comparable to the required lines of Section III.

B. Application to Cygnus X-1

For Cygnus X-1, the emission region model described in Table 3 (gas model 1) was chosen for the initial profile computations. This flow system is assumed to exist in the reference binary model of Table 1. The electron density was selected from typical ranges quoted by Batten (1973b) in a summary of known mass flow characteristics, and is consistent with the absence of forbidden lines in Cygnus X-1. Although the energy balance of the gas was not done in detail, an electron temperature of 10^4 °K is reasonable for this system and density (cf. Spitzer 1968) if energy gains in the gas from viscous or shock heating and X-ray irradiation augment slightly the effects of the B0 primary. The statistical equilibrium equations were written for the first five hydrogen bound states (n = 5) and the continuum.

In Table 4 are listed the results of the opacity and emissivity calculations for gas model 1 and several variations of it. A population inversion at Hβ was observed. In the table, the absorption and emission coefficients are

Table 3. Gas model 1

$T_1 = 3 \times 10^4$ °K	$W_1 = .3$	$T_2 = 10^7$ °K	$W_2 = 10^{-7}$
$T_e = 10^4$ °K	$N_e = 2 \times 10^{12}$ cm^{-3}		
$R_1 = .2\ R_\odot$	$R_2 = 7\ R_\odot$	$\Delta\phi = 120°$	$\Delta z = 4\ R_\odot$

Table 4. Gas properties

Gas Model No.	Gas Model Parameters				Opacity (10^{-13}) cm^{-1}			Emissivity (10^{-6}) ergs/sec cm^3 ster Å		Absorption, emission coefficients	
	T_e (10^4) °K	N_e (10^{12}) cm^{-3}	W_1	log W_2	K_{es}	K_{ff}	K_{bf}	j_{ff}	j_{fb}	k_ℓ (10^{-10}) Å/cm	ε_ℓ (10^{-2}) ergs/sec cm^3 ster
1	1	2	.3	-7	13	.60	2.5	1.4	13	3.2	4.8
1a			.4	-6	13	.60	2.2	1.4	13	2.7	4.6
2		1	.3	-7	6.7	.15	.61	.36	3.2	.76	1.2
2a			.4	-6	6.7	.15	.52	.36	3.2	.63	1.2
3	1.5	2	.3	-7	13	.40	1.8	3.1	11	2.3	3.7
3a			.4	-6	13	.40	1.6	3.1	11	1.9	3.5
4		1	.3	-7	6.7	.11	.45	.78	2.8	.56	.90
4a			.4	-6	6.7	.11	.39	.78	2.8	.47	.90

defined by $\kappa_\ell = k_\ell \phi_\lambda$ and $j_\ell = \varepsilon_\ell \chi_\lambda$. Table 5 shows the rough line estimates for these same gas models for a chosen line of sight dimension $s = 5 \times 10^{11}$ cm, and a relative continuum strength F of .001. Parameters are shown for the cases W_0 = thermal width and W_0 = 1Å, and the gas volume needed to assure the value of F is also displayed. From Table 4 it is seen that the continuum opacity is dominated by the electron scattering contribution and that all reasonable choices for a line of sight dimension of a disk in this system guarantee an optically thin continuum. The electron density appears to have significant influence on the gas characteristics. The parameters of Table 4 are more responsive to N_e changes than to the T_e changes considered. This behavior may be important later in the determination of more disk model limitations on the blending mechanism. The variation of the dilution factor seems to exert only a small influence on the continuum parameters, the largest effect being seen in the bound-free opacity. Line parameters are a bit more affected and the dilution factors may play an important role in defining emission line shape. Independent variation of W_1 and W_2 reveals a comparable sensitivity of the results to each of these parameters.

The preliminary emission line estimates of Table 5 are encouraging. The thermal lines and the broadened (1Å)

Table 5. Emission line estimates

Model Number	Thermal Width Profile				1Å Width Profile				Volume
	H	W(Å)	EW(Å)	τ	H	W(Å)	EW(Å)	τ	$cm^3(10^{34})$
1	31	.6	.04	357	30	2.5	.16	75	7
1a	35	.6	.04	302	35	2.5	.19	63	7
2	109	.6	.14	85	107	2.0	.46	18	29
2a	127	.5	.14	70	124	2.0	.53	15	29
3	30	.8	.05	216	30	2.5	.16	54	7
3a	35	.8	.06	178	34	2.5	.18	44	7
4	105	.6	.13	53	104	2.0	.44	13	28
4a	121	.6	.15	44	118	2.0	.50	11	28

lines have acceptable equivalent widths in the primary continuum: the required lines of Section III had equivalent widths from .01 to 1.4Å roughly, so this gas model can put enough energy into emission to possibly affect the primary spectrum. Line heights are generally encouraging as well, the higher N_e results in particular are included in the range of heights derived for the required lines (Figure 9). Widths are narrow in the thermal case, but apparently sensitive to the nature of the broadening mechanism: the 1Å lines are in the width range of the acceptable lines of Figure 9. The total optical depths listed in this table are not so encouraging, and the results for the line parameters must be weighed carefully in the light of these high values which apparently contradict the assumption of optical thinness. A discussion of the possible effects of this disparity will be included in Section V. For the present we notice that artificial broadening does correct the disparity somewhat and that much better agreement is to be expected from models with a more realistic velocity field: the velocity dispersion of a Keplerian disk should improve these results markedly, producing an optically thinner disk and producing stronger, broader emission lines. Models with a smaller line of sight dimension would also be more acceptable. The volume of gas necessary to fit F = .001 is acceptable, but rather large in

the case of the lower electron densities: the values correspond roughly to one-tenth and one-half the secondary Roche lobe volume. The strong influence of N_e on emission line production implies a restricted range of densities for which blending may be significant.

The initial line estimates encourage the extension of this treatment to consideration of detailed disk models. To that end, the full geometric description of gas model 1 was considered for the computation of a detailed profile. Only thermal broadening was used. Also considered were the N_e, T_e variations of model 1 listed in Table 4 as models 2, 3 and 4. The resultant profiles are displayed in Figure 21 where the profile number corresponds to the model number from which the line was computed. To more easily compare these lines of differing F, relative flux has been plotted instead of H. The profiles are similar in their anticipated blending properties and have a small spread in peak position. Generally, the hotter, thinner gases put more energy into emission than did model 1. Models which differ from model 1 in geometry were also considered for the profile derivation. These models are defined in Table 6. They test the role of disk shape in the formation of emission lines. The results of these geometric variations are displayed in Figures 22 and 23. Profile 5 results from a much smaller disk than that of model 1 and is consequently much weaker

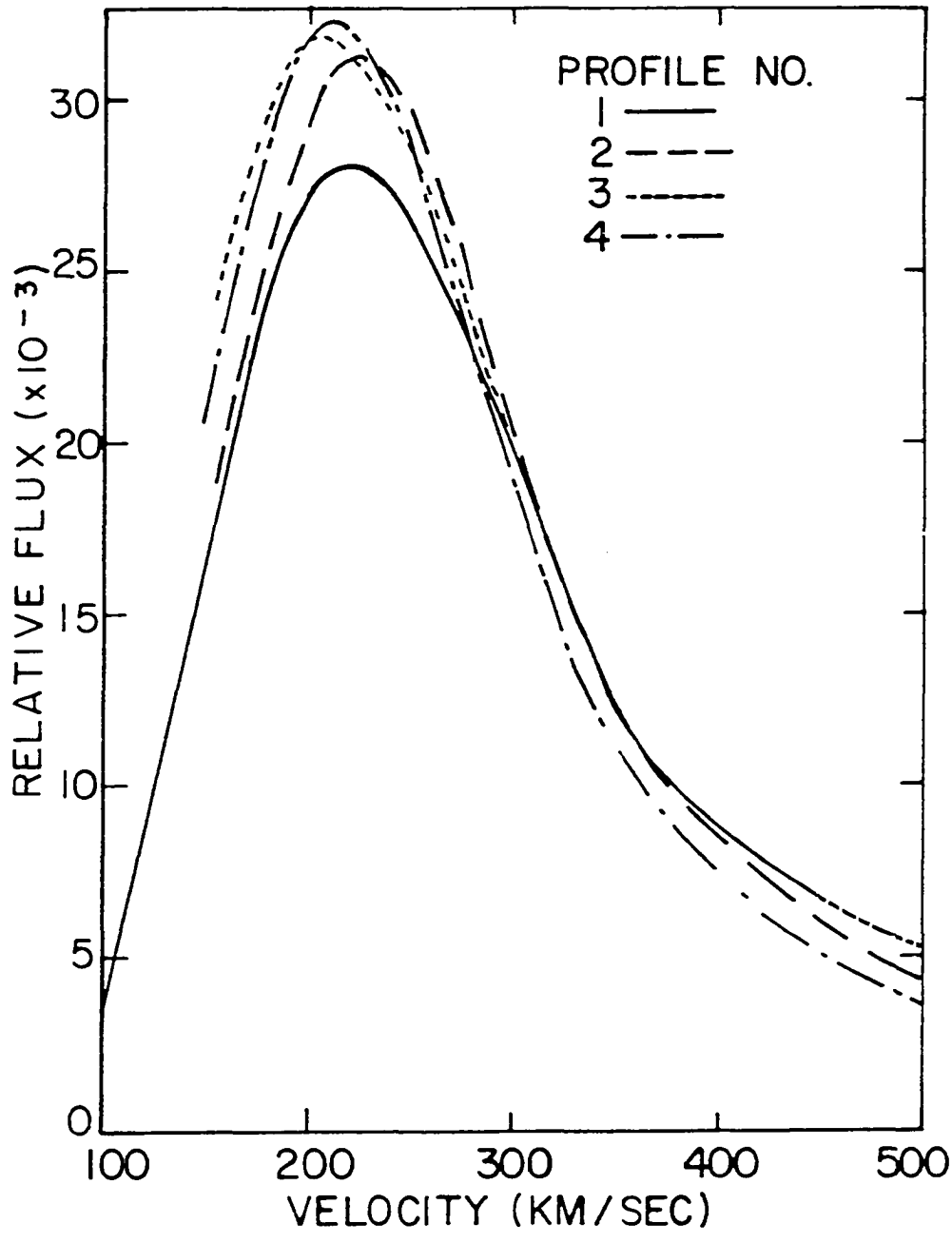

Figure 21. Expected emission lines: N_e, T_e variations

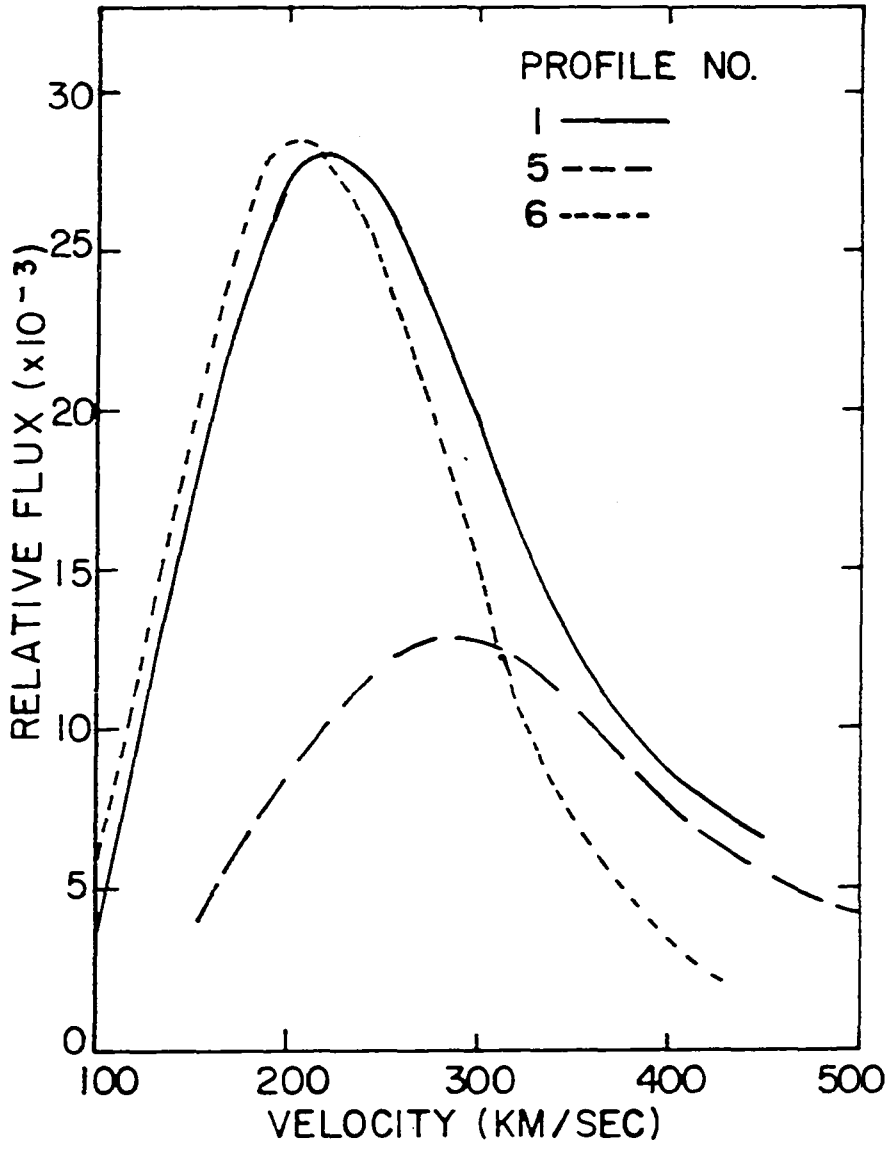

Figure 22. Expected emission lines: geometry variations I

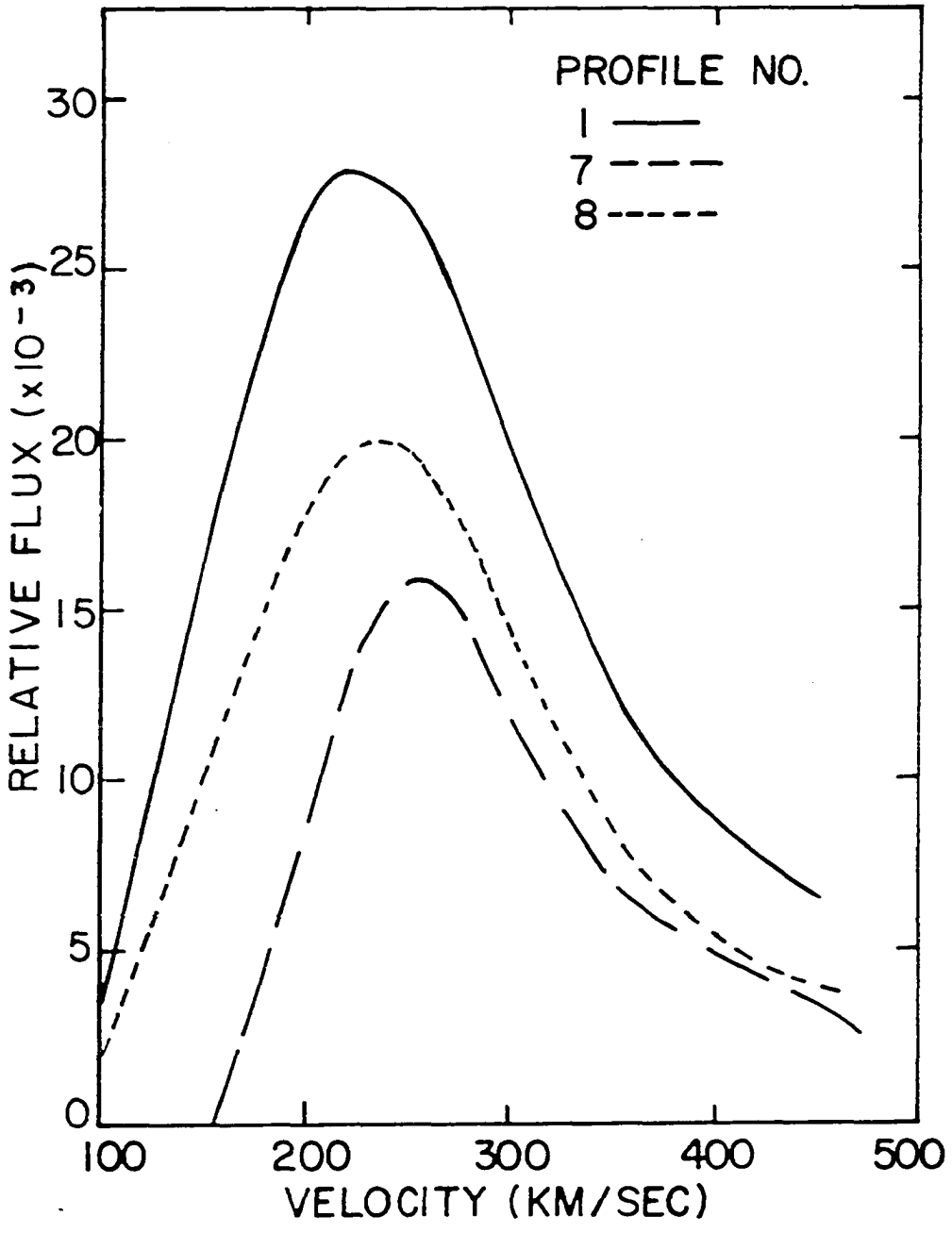

Figure 23. Expected emission lines: geometry variations II

Table 6. More gas models: geometric variations from model 1

Model Number	Change from Model 1
5	$R_2 = 4\ R_\theta$
6	$R_1 = 2\ R_\theta$
7	$\Delta\phi = 60°$
8	$\Delta z = 2\ R_\theta$

than profile 1, though it may share some blending properties with profile 1 in the wing. Profile 6 results from a larger inner radius for the disk section, simulating a ring model. Omission of the fast inner Kepler core of the disk shifts the peak to a lower velocity and sharpens the profile somewhat without significantly affecting line strength. In Figure 23, profile 7 is produced by a disk section of reduced angular extent and so is somewhat weaker than profile 1. Much of the slow radial velocity contributions to the light in emission have been eliminated, yielding the higher-velocity, asymmetric profile shown. Finally, profile 8, produced by a thinner disk, is also weaker than profile 1, but the smaller optical depth across this disk compensates somewhat for the lower energy content, and yields emission stronger than that in profile 7.

To evaluate the actual blending properties of these lines in the context of the required lines of Section III

is difficult. In order to compare these nongaussian lines with the gaussian profiles of the last section, several attempts were made to fit gaussian curves to portions of these profiles. Such an approach is admittedly artificial, and the possible consequences of fit deviations must be considered to fully justify the comparison. This problem is discussed below. In Figures 24-31 are shown the trial gaussian fits made to each of the eight profiles discussed above. Four trials were run on each profile. The first attempt was a fit to all the profile points generated. Generally these fits had little relation to the profile points, but served as a first guess at the effective H, W and V_e for the line. More serious attempts to derive gaussian parameters reflective of the blending properties of these lines were undertaken by restricting the region of the fit. A region near line center was chosen to represent the properties of that portion of the profile, and a region centered on the high velocity side of the peak was chosen for comparison. The results of these trials are shown in Tables 7 and 8. The departures from these fits are generally significant only in the far red wing (Figures 24-31), which is important in the consideration of whether or not the blended line will be unacceptably distorted by the actual nongaussian profile. This is unlikely since the violation would have to be one of excessive filling in of

Figure 24. Gaussian fits to profile 1

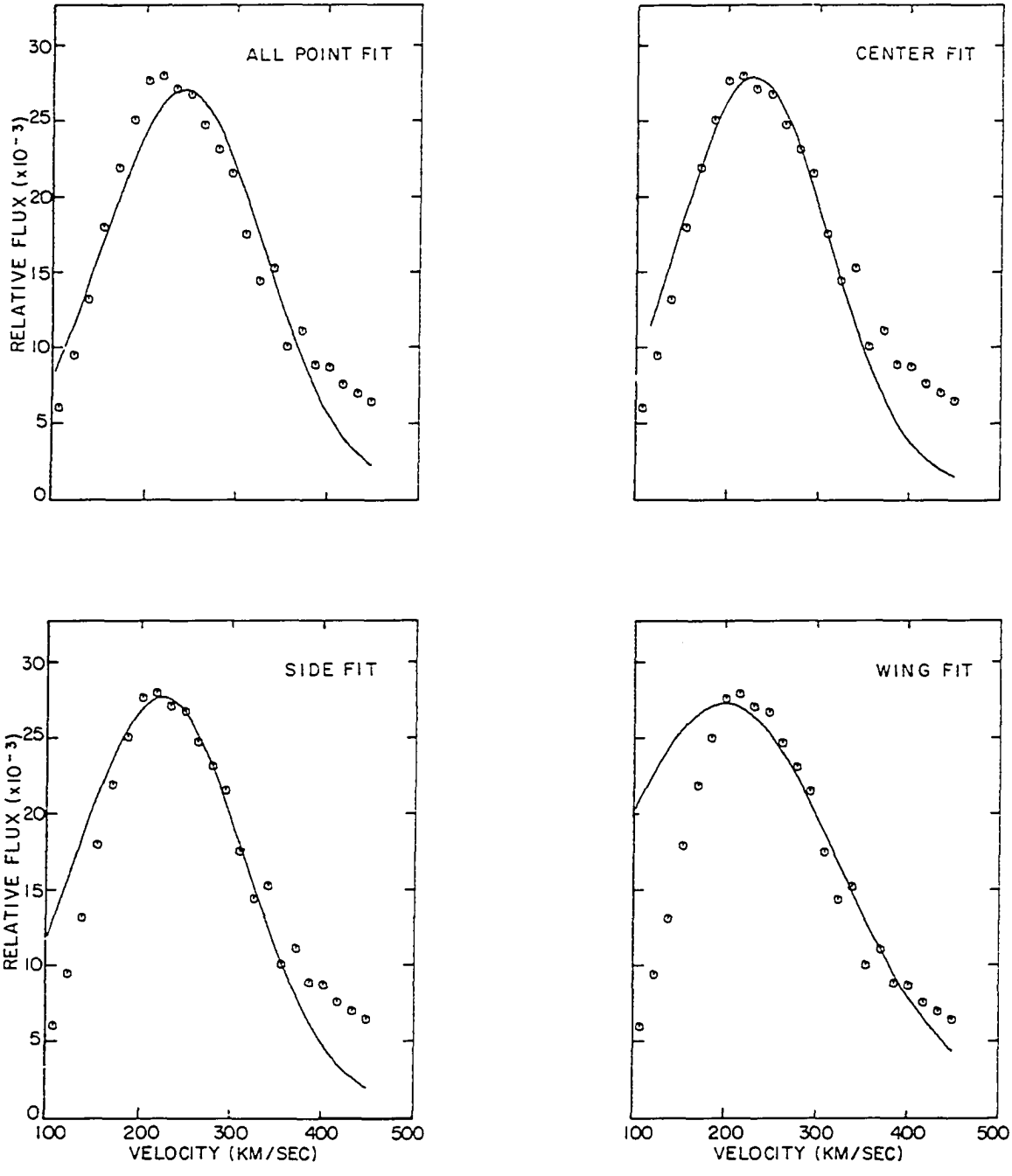
ALL POINT FIT
CENTER FIT
SIDE FIT
WING FIT
RELATIVE FLUX (x10⁻³)
VELOCITY (KM/SEC)
0
5
10
15
20
25
30
100
200
300
400
500

Figure 25. Gaussian fits to profile 2

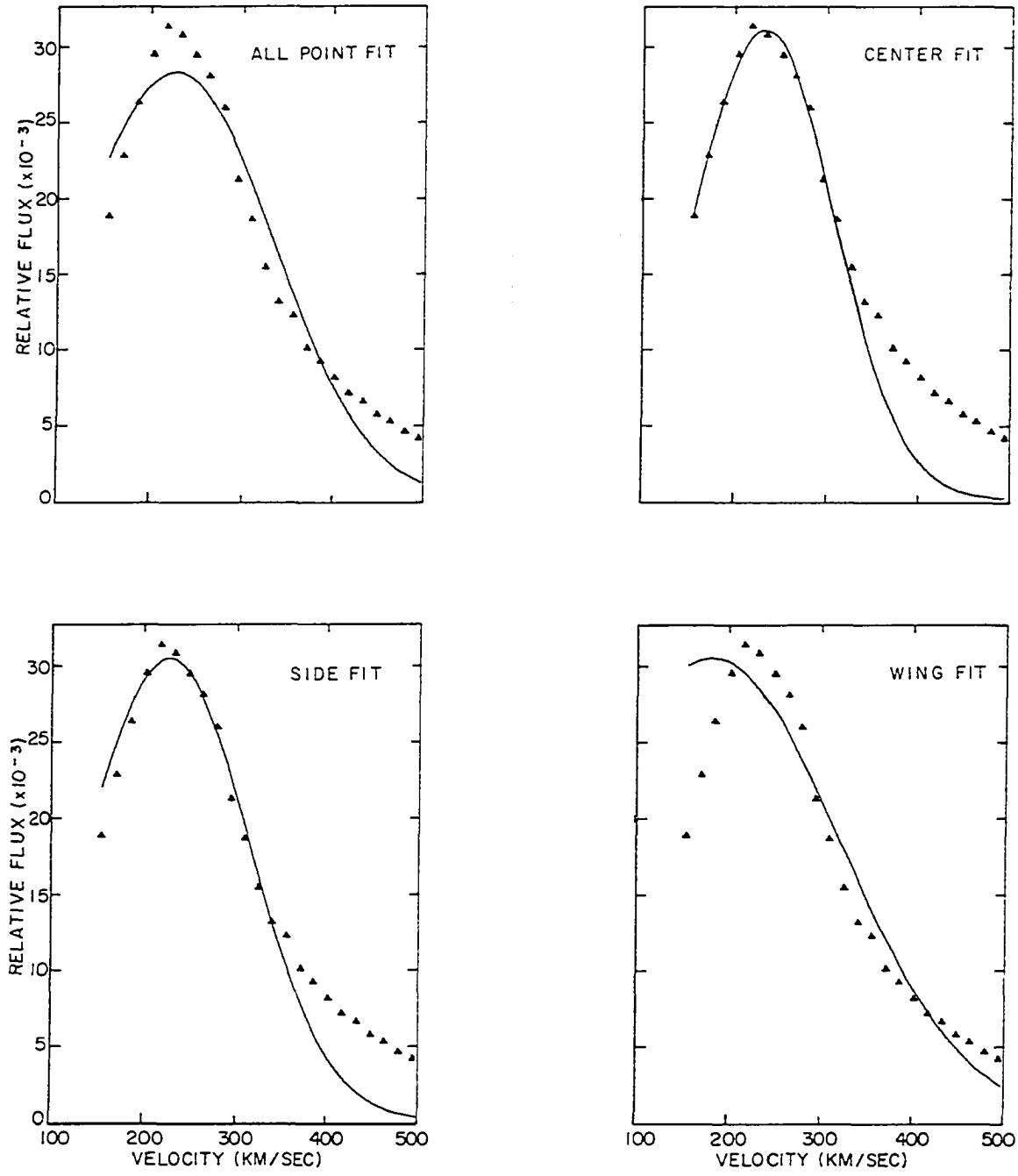
ALL POINT FIT
CENTER FIT
SIDE FIT
WING FIT
RELATIVE FLUX (x10⁻³)
VELOCITY (KM/SEC)
0
5
10
15
20
25
30
100
200
300
400
500

Figure 26. Gaussian fits to profile 3

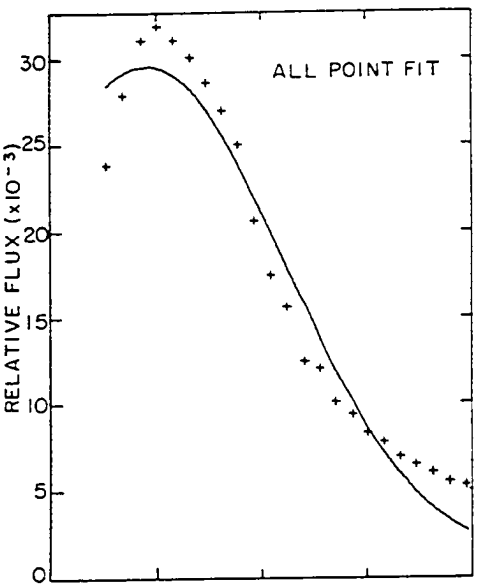
ALL POINT FIT
RELATIVE FLUX (x10⁻³)
0
5
10
15
20
25
30

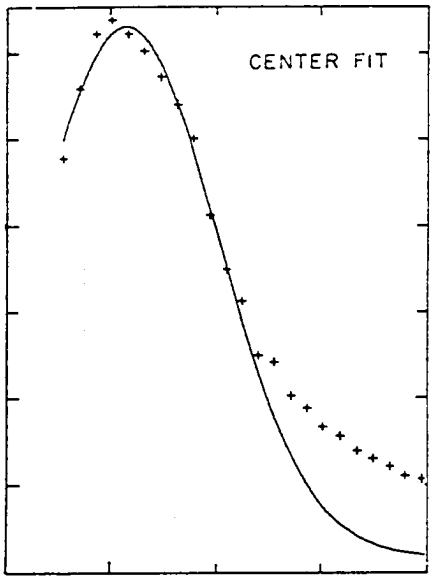
CENTER FIT

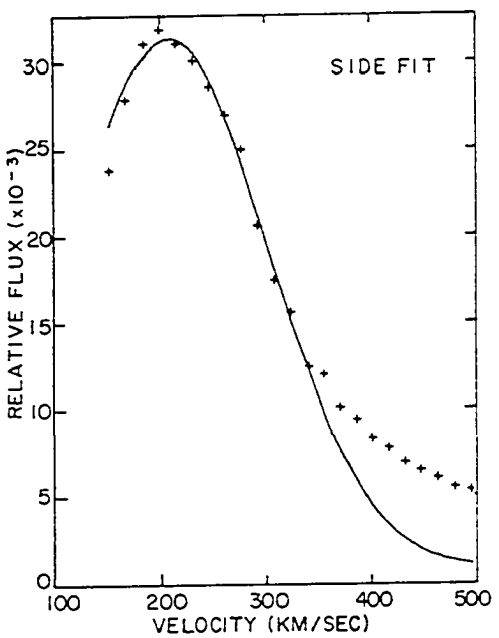
SIDE FIT
RELATIVE FLUX (x10⁻³)
0
5
10
15
20
25
30
100
200
300
400
500
VELOCITY (KM/SEC)

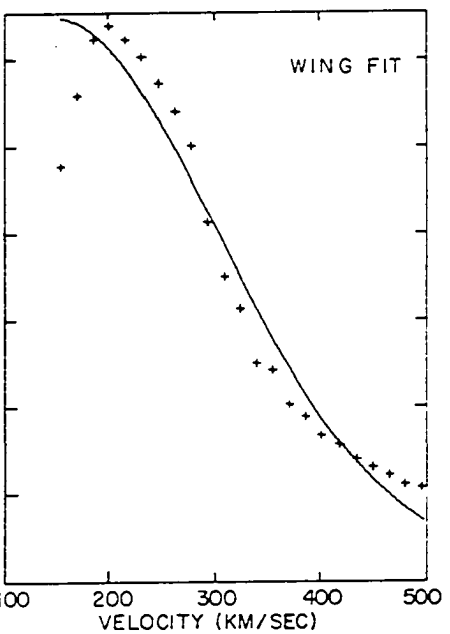
WING FIT
100
200
300
400
500
VELOCITY (KM/SEC)

Figure 27. Gaussian fits to profile 4

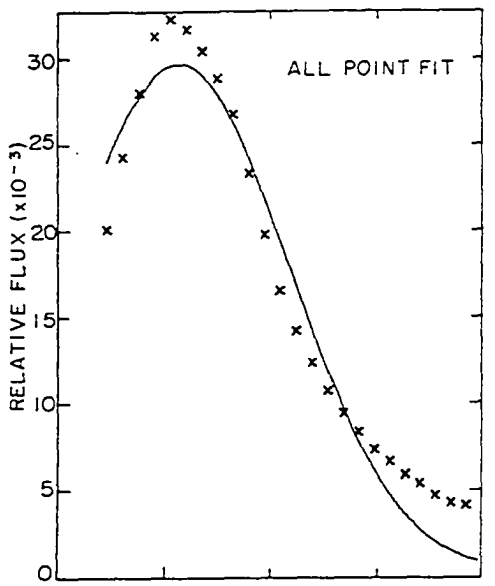
ALL POINT FIT
RELATIVE FLUX (x10⁻³)
0
5
10
15
20
25
30

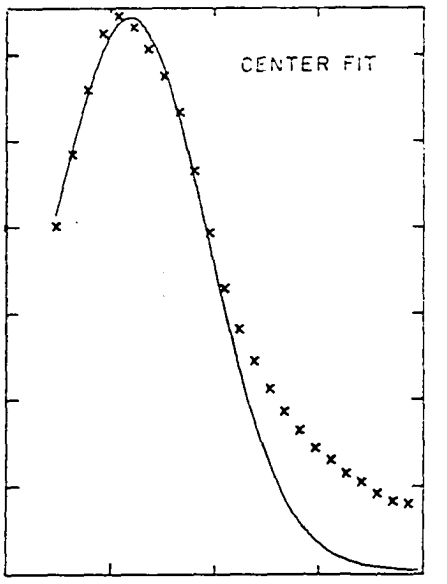
CENTER FIT

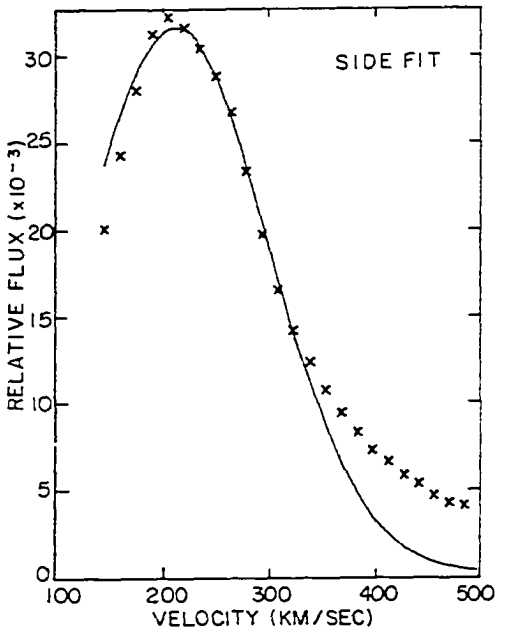
SIDE FIT
RELATIVE FLUX (x10⁻³)
0
5
10
15
20
25
30
100
200
300
400
500
VELOCITY (KM/SEC)

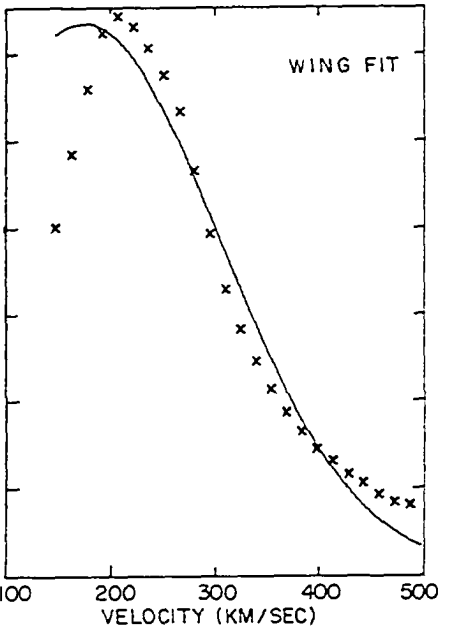
WING FIT
100
200
300
400
500
VELOCITY (KM/SEC)

Figure 28. Gaussian fits to profile 5

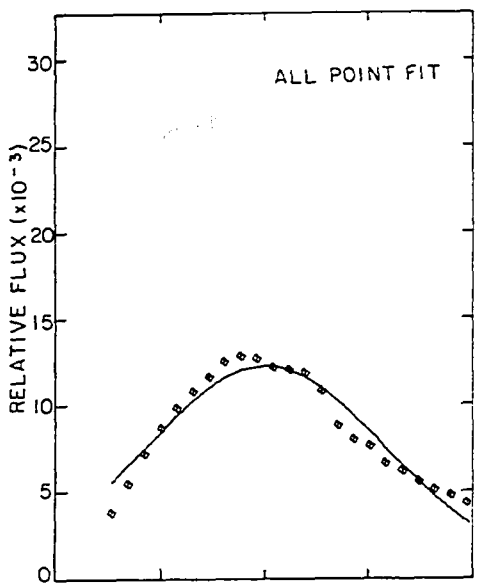
ALL POINT FIT
RELATIVE FLUX (x10⁻³)
0
5
10
15
20
25
30

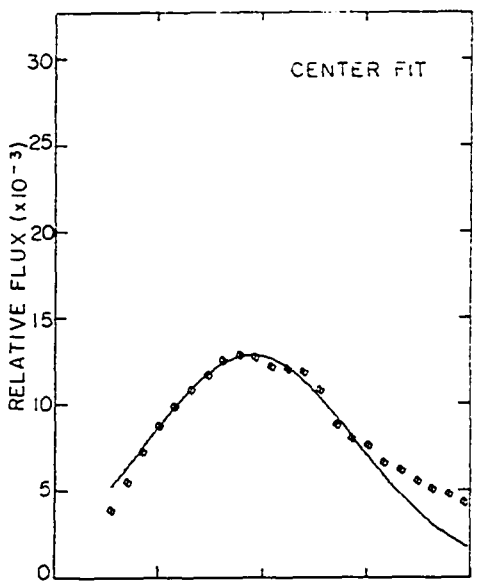
CENTER FIT
RELATIVE FLUX (x10⁻³)
0
5
10
15
20
25
30

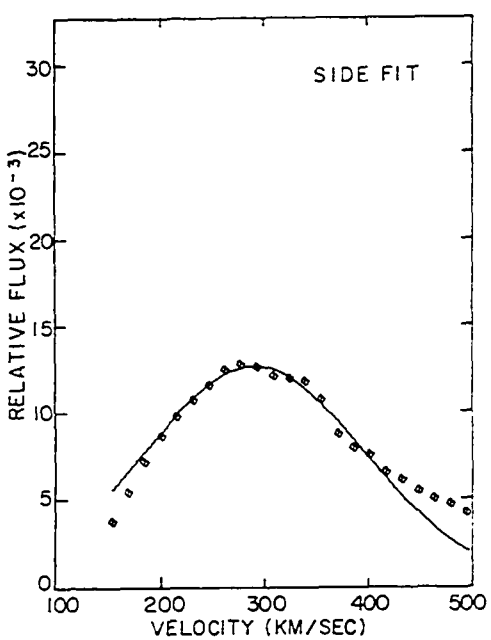
SIDE FIT
RELATIVE FLUX (x10⁻³)
0
5
10
15
20
25
30
100
200
300
400
500
VELOCITY (KM/SEC)

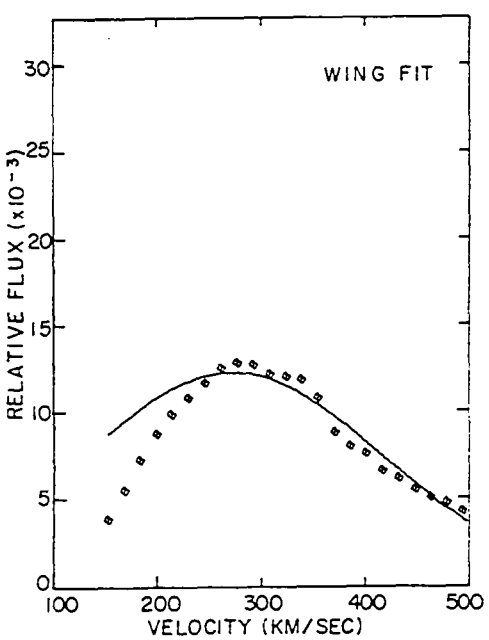
WING FIT
RELATIVE FLUX (x10⁻³)
0
5
10
15
20
25
30
100
200
300
400
500
VELOCITY (KM/SEC)

Figure 29. Gaussian fits to profile 6

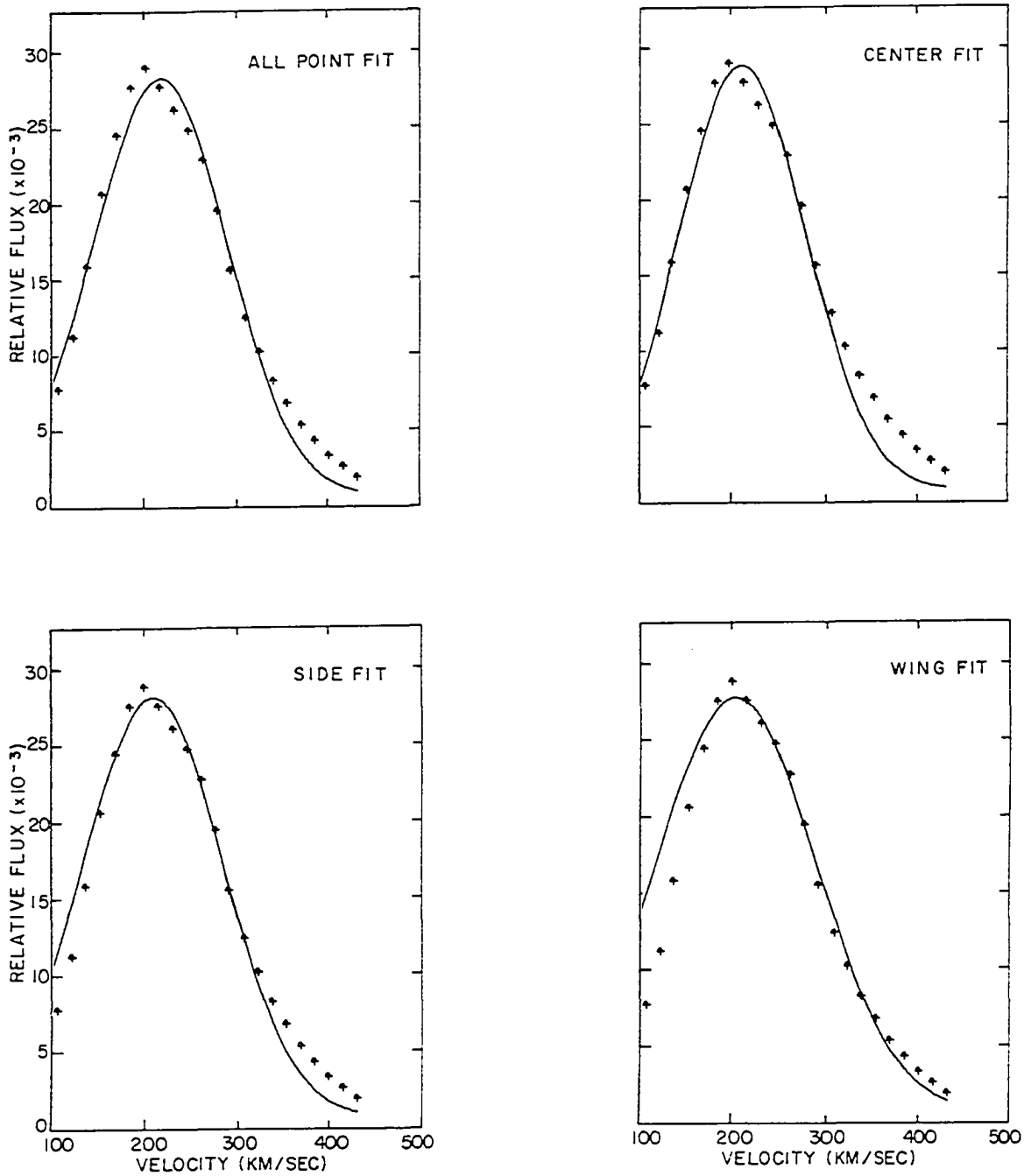
ALL POINT FIT
CENTER FIT
SIDE FIT
WING FIT
RELATIVE FLUX (x10⁻³)
VELOCITY (KM/SEC)
0
5
10
15
20
25
30
100
200
300
400
500

Figure 30. Gaussian fits to profile 7

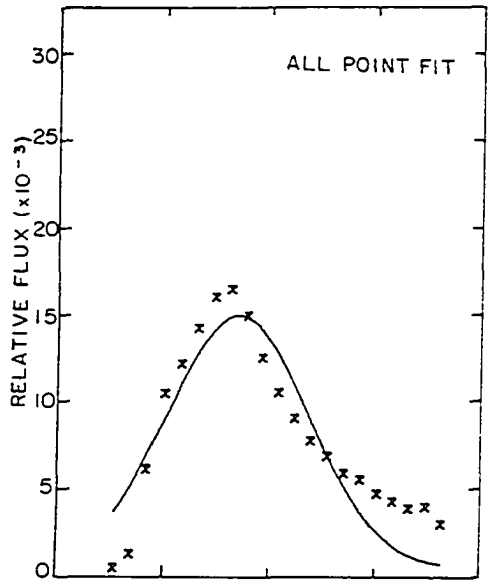
ALL POINT FIT
RELATIVE FLUX (x10⁻³)
0
5
10
15
20
25
30

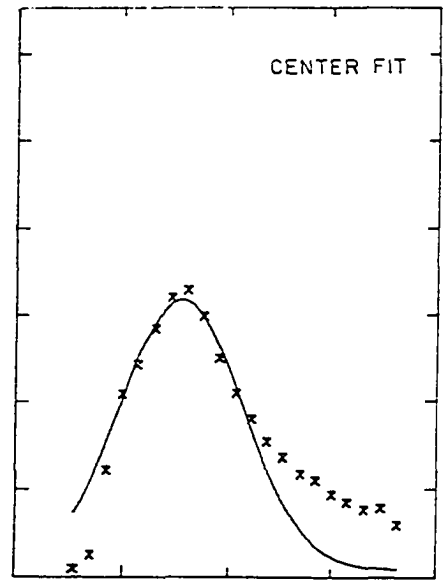
CENTER FIT

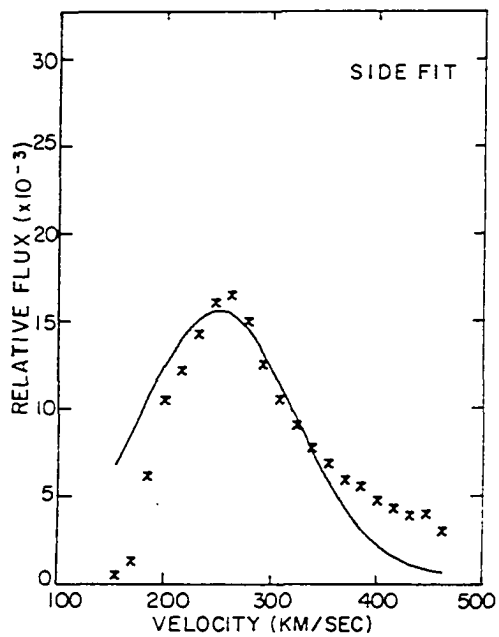
SIDE FIT
RELATIVE FLUX (x10⁻³)
0
5
10
15
20
25
30
100
200
300
400
500
VELOCITY (KM/SEC)

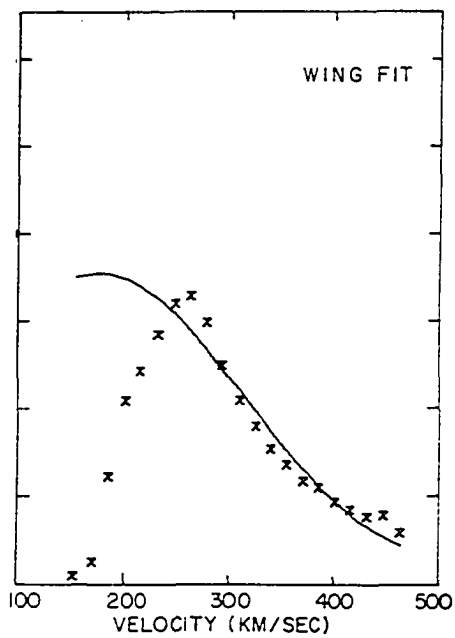
WING FIT
100
200
300
400
500
VELOCITY (KM/SEC)

Figure 31. Gaussian fits to profile 8

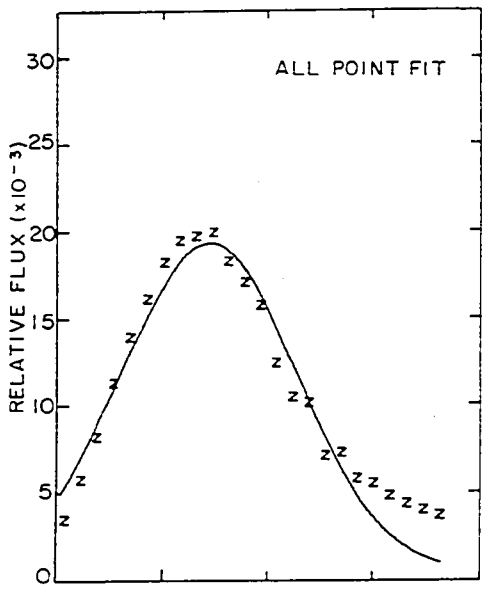
ALL POINT FIT
RELATIVE FLUX (x10⁻³)
0
5
10
15
20
25
30

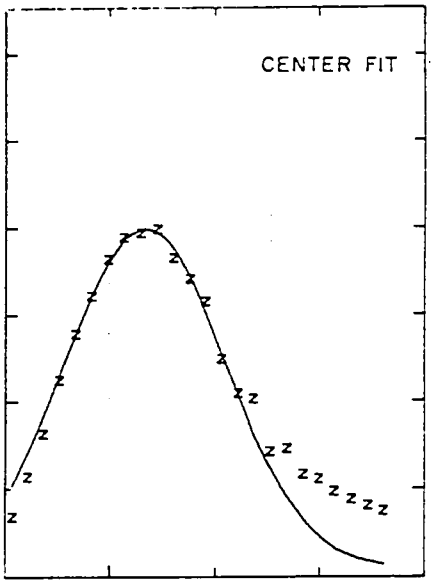
CENTER FIT

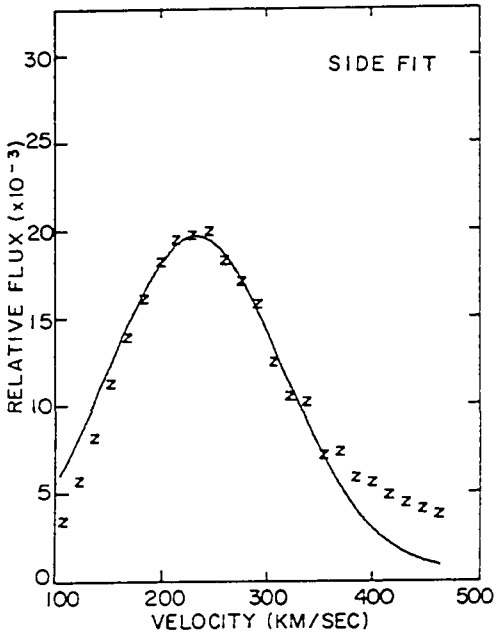
SIDE FIT
RELATIVE FLUX (x10⁻³)
0
5
10
15
20
25
30
100
200
300
400
500
VELOCITY (KM/SEC)

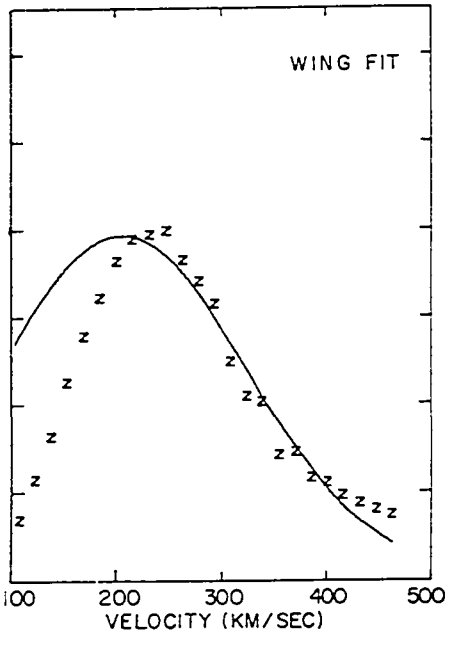
WING FIT
100
200
300
400
500
VELOCITY (KM/SEC)

Table 7. Expected emission line parameters: center fits

Profile	Fit Range (km/s)	$F(10^{-3})$	H	W(Å)	V_e(km/s)	EW(Å)
1	150 to 310	.80	34	1.3	225	.08
2	150 to 310	.23	134	1.2	230	.08
3	150 to 290	.83	37	1.4	215	.09
4	140 to 290	.24	134	1.2	218	.08
5	200 to 390	.27	46	1.6	290	.04
6	100 to 295	.73	39	1.1	214	.07
7	200 to 330	.43	37	1.0	257	.03
8	150 to 325	.44	44	1.2	236	.05

Table 8. Expected emission line parameters: side fits

Profile	Fit Range (km/s)	$F(10^{-3})$	H	W(Å)	V_e(km/s)	EW(Å)
1	190 to 310	.80	34	1.5	222	.09
2	190 to 350	.23	132	1.4	226	.09
3	180 to 340	.83	37	1.5	210	.10
4	185 to 340	.24	132	1.4	213	.09
5	210 to 410	.27	46	1.7	290	.05
6	150 to 305	.73	38	1.2	211	.07
7	230 to 350	.43	36	1.2	251	.04
8	190 to 340	.44	44	1.3	235	.05

the absorption line, a condition arising only in the highest V_e lines of Figure 10 (i.e., only for superposition of a strong emission profile on the absorption reference line).

An attempt was also made to fit the entire red wing of each profile with a gaussian curve. These wing fits are also displayed in Figures 24-31 and are described in Table 9. In some cases the representation of the blending properties of the line by such a fit is fairly good. Only profile 7 (Figure 30) could not be reasonably fit with effective gaussian parameters, so its blending properties are not well-estimated. This defect will prove to be unimportant because of the relative weakness of this line. Wing fitting generally yields effective gaussian lines of larger width and lower peak velocities than the other fits, and consequently if the rejection criteria of Section III are applied to these gaussian profiles, they would be artificially labeled unacceptable. For example, the blue wing is not actually strong enough to cause the significant continuum intrusion which the gaussian line might suggest.

For each of the eight profiles, the various fits differ little in their gaussian line parameters. Even the wing fit values are not dramatically different from those of the center and side fits. Therefore, we conclude that for comparison with the lines of Section III, each of the eight profiles (except profile 7) may be represented with some

Table 9. Expected emission line parameters: wing fits

Profile	Fit Range (km/s)	$F(10^{-3})$	H	W(Å)	V_e(km/s)	EW(Å)
1	190 to 450	.80	34	2.0	200	.12
2	190 to 560	.23	132	2.2	180	.14
3	180 to 550	.83	38	2.5	148	.17
4	185 to 490	.24	133	2.0	174	.14
5	230 to 515	.27	44	2.3	273	.06
6	170 to 440	.73	38	1.4	205	.08
7	230 to 470	.43	41	2.2	174	.08
8	200 to 460	.44	44	1.9	206	.08

reliability by only a small range of gaussian lines. As expected, this detailed profile calculation has confirmed the nature of the emission lines predicted by the first estimation method, and improved the results markedly. Equivalent width results are similar in both treatments, while wider lines, having much lower optical depths, were produced by the more realistic approach.

In this section we have described eight emission lines physically produced by gas in the Cygnus X-1 binary system. In terms of gaussian parameters, these lines are defined by the small range of values presented in Tables 7, 8 and 9. We are now ready to compare these profiles with the lines of Section III in order to evaluate the importance of emission contamination as a mechanism for velocity curve distortion.

V. DISCUSSION

A. Comparison of Emission Lines

In this section we evaluate the importance which emission-absorption blending might have in affecting the mass determination of Cygnus X-1. This evaluation will proceed in four main steps. First, the actual emission lines expected from plausible models of the gas flow in this system (Section IV) will be compared with the hypothetical emission lines which are known to be able to affect the mass determination significantly (Section III). Next, the qualifications and assumptions used in the derivations of the last three sections will be critically reviewed. The third step will present and evaluate other consequences of this model and finally, possible observational tests of this effect will be discussed and some extensions of this work suggested.

To begin, we evaluate the blending properties of the profile produced by gas model 1 (Figure 24) and then discuss the other lines comparatively. The relative continuum strength F of this model is .0008 which is comparable to the value used to derive the required emission lines of Figures 9 and 10 and 13-18. Apparently, the equivalent gaussian parameters for this profile, displayed in Tables 7-9, fall within the solution volume defined by the surfaces in these

figures. In particular, the wing fit values of Table 9 and the side fit values of Table 8 bracket the reference surface (Figure 9) and are very close to it. This is evident if these values are compared with those explicitly displayed in Figure 7. Profile 1 can cause the required distortion. In fact, the actual profile is less likely to cause unwanted distortion than its wing fit gaussian equivalent as noted earlier (compare the blue wings in the Figure 24 wing fit plot). Profile 1 is a medium energy member of the solution set of Figure 9, its .09 Å equivalent width lying comfortably in the .01 to 1.4 Å range of that set. For gas model 1, the disk's luminosity is $\sim 10^{35}$ ergs/sec and its mass is $\sim 10^{-10}$ $M_\odot$, yielding a low ($\leq$ 1 km/sec) average radial infall velocity if an X-ray luminosity of 10^{37} ergs/sec is to be fueled (cf. Davidson and Ostriker 1973). This result is important in that the postulated Keplerian velocity field is not disrupted by the required infall speed. Also, too rapid an infall speed would be hard to explain with viscous forces and might lead to variability in the disk properties over relatively short timescales. This last possibility is unacceptable for the present model.

The nature of profile 1 as a contaminating emission line can be put into clearer perspective in the following way. The absorption line produced by the reference model

of Table 1 ($\Delta\lambda_a' \simeq 5\text{Å}$, $D' \simeq .2$) can be put into the coordinates of Figures 21-23. On those plots this line would be centered at 324 km/s and range in relative flux from 0.8 to 1.0 with a half width at half depth of about 365 km/s. With respect to this line, profile 1 would be represented in normalized coordinates by H = 34, W = .3, X_E = -.3. By comparing these values with those of emission lines in Figures 4-6 we can get some idea of the blend which profile 1 would produce. We anticipate a blend intermediate to those shown in Figures 5A and 6A.

From Figures 21-23 we see that gas models 2, 3, 4 and 6 all produce profiles similar to profile 1 and so are also expected to fall within the solution volume of Section III. This conclusion is also supported by the analysis of the behavior of the surfaces in that section. Figures 9, 11, and 12 show that lower F surfaces admit higher-H lines. Thus we might expect the lower F profiles which have larger H values (profiles 2, 4, and 6) to also be acceptable contaminating lines.

From Table 7 (for example) we see that the electron density N_e is a sensitive control of F and of line height H (compare the high-N_e profile 1 with the low-N_e profile 2), and, in general, of line strength as well (Figure 21). The F restrictions of Section III therefore imply some restrictions on N_e for effective emission region models. The

upper limit on F is defined by distortion and visibility considerations and seems to be about .01. Since an increase in N_e significantly increases F, this limit implies an upper limit on N_e as well. Actually, considerations other than F value more severely limit the maximum N_e. Too large an electron density inhibits the line emission itself. Collisions become important in the gas and enhanced emission from overpopulated upper levels is no longer possible: the disk emission reflects local conditions and not the direct effects of the stellar irradiation. From consideration of the relative rates of collisional and radiative transitions at Hβ, an upper limit on N_e of 10^{13} cm^{-3} seems generous.

The lower limit on F is set by the behavior of the solution surfaces of Section III with decreasing F. The range of acceptable lines moves steadily toward sharper lines. Decreasing N_e, while lowering F also produces sharper lines with the increased velocities necessary to keep the profiles near the solution surface of Figure 9. This implies that no lower limit need be set on N_e. Actually such a limit can be estimated by noticing that there is a limit to the sharpness and speed of an acceptable emission line above which the emission becomes resolved in the absorption profile. For narrow, high lines the velocity thickness of the solution volume becomes small as well - these lines must be precisely located in the absorption profile to cause

acceptable blending. From these considerations a lower limit of 5×10^{11} cm^{-3} seems reasonable for N_e.

Temperature variations produce profile changes which behave much like those induced by N_e variations. The similarity of profiles 3 and 1 indicate that lines produced by temperature changes in model 1 should retain their blending properties - especially near absorption line minimum (at 324 km/s in Figure 21). If the slight line strength change does not yield observable blend distortion, these lines should remain in the solution set. This conclusion can be stated in another way. A temperature increase produces a more energetic emission line, but changes F only slightly. Considering, then, the surface of Figure 9, we see that the parameter trends of Table 7 reflect the shape of that surface: higher, wider lines have lower velocities. Thus T_e changes cannot readily remove a profile from the set of good contaminating lines. As in the case of N_e variation, limits on T_e arise less from the constraints of Section III than from the approximations of Section IV. If the temperature is too high, collisional rates thermalize the profile; if the temperature is too low, increased opacities weaken the emission. These violations of the Section IV limits for collisional rates and optical depth are less sensitive to T_e than to N_e, and so a range of T_e is more difficult to

estimate. An interval from 5×10^3 to 1.5×10^4 °K may be a good first guess, with the upper limit being set by consideration of heavy element cooling and total energy requirements rather than by unacceptable collisional rates. In fact, the N_e and T_e limits are related, and a product of these quantities may be the properly bounded quantity. Empirically, we find $5 \times 10^{15} < N_e T_e < 10^{17}$ where the units are degrees/cm^3.

Figures 22 and 23 indicate that geometry may be very important in the production of acceptable emission lines. The models 5-8 represent smaller volume regions than that of model 1 and consequently yield weaker emission lines. We cannot conclude however, that these lines are unable to cause the required distortion of the reference absorption line because the solution volume of Section III admits lines even weaker than these. To remain in the solution volume, these profiles need not vary from the profile of model 1 in accord with the shape of the reference surface, although to do so would help to guarantee such containment. The low F values of these lines makes comparison with the surfaces of Section III difficult; therefore, we will discuss these profiles in terms of their effective heights in the F = .001 continuum. This can be done in a conservative way since overestimation of F increases the rejection probability. The effective heights for profiles 5-8 are then 13, 28, 16

and 19 respectively for the side fit case (Table 8). The effective height of profile 1 is 27 in an F = .001 secondary continuum. Each of the geometry variations of Table 6 produces a distinct emission profile not easily related to the others: each profile must be considered separately. One general trend can be seen however. From Figure 9 it appears that lower H lines require higher velocities to cause the proper distortion. This trend is followed by the profiles of Figures 22 and 23. Therefore, since profile 1 is acceptable, it seems likely that the others may also be.

To see if this is indeed the case, we now describe each profile's position with respect to the reference surface (Figures 9 and 10) with the help of Figures 7 and 8. We use the effective heights and side fit values for W and V_e (Table 8). Profile 1 lies about 20 km/s above the Figure 9 surface, a position comfortably within the solution volume defined by either ΔV_{OB} variation (Figures 13-14) or by primary mass uncertainty (Figures 16-17). Profile 5 is about 10 km/s above the Figure 10 surface, a position also within those limits. We speculate, for example, that for $M_p \simeq 20\ M_\theta$ this line will produce an acceptable blend much like that shown in Figure 6A. Profile 6 is too sharp to be acceptable. Its position corresponds to that of a line able to cause the proper distortion, but one which may be resolved in the blend. Only for the extreme cases $\alpha = 0$ (thinner

reference line), i = 30° or M_p = 12 M_θ (effectively thinner reference line) will this line lie within the solution volume. The conservative nature of the rejection criteria should be underscored at this point and we speculate that such a line may not be readily resolved in practice (blurring caused by photon noise). Profile 7 is not well-represented by gaussian parameters and this example is only illustrative. Its position is 20 km/s above the Figure 9 surface and so this line too lies within the solution volume. Finally, profile 8 is also acceptable since it is only 15 km/s above the reference surface.

The conclusion we reach from this discussion is that the partial disk models considered above produce a range of emission lines which clearly intersects the solution volume of Section III. The fact that this intersection occurs at the low-W, medium-H, high-V_e edge of the solution volume is significant, as is the failure of profile 6 to fall within this volume. Since models 5-8 represent smaller emission regions, the implication is that larger disk sections will produce emission lines much deeper into the volume of acceptable contaminating lines. Such models (especially those whose inner radius is small, unlike model 6) will yield wider lines because of the greater velocity dispersion, and slower V_e's as symmetry about the secondary is increased. Adjustment of N_e and T_e could produce some H

value changes if necessary.

The plausibility of larger disk models contributing to this subtly distorting emission is reinforced by other considerations as well. The increased stability of emission integrated over a larger region is attractive for this model. Also the behavior of the dilution factors W_1 and W_2 indicate that a larger region than just that between the stars may be put into emission. W_1 varies only slowly across such a disk and the sensitivity of the results to this small change is not great (Table 4). In a complementary fashion, W_2 will increase rapidly near the secondary. The combined effect of such behavior is to encourage whole disk emission. Problems arise in extrapolating the results of this section to such models - disk structure becomes important - but such a trend is encouraging with respect to the absorption-emission mechanism.

Apparently, for Hβ, the strong radiation field and regular mass flow characteristic of close X-ray binaries can produce a range of emission lines, each able to mask a low-mass secondary by interfering with velocity determinations. That such an effect is important for a reasonable, but restricted, range of density, temperature and gas flow dimension is consistent with the anomalous nature of Cygnus X-1 (below). To more fully evaluate this result we

now review the qualifications of our treatment.

B. Qualifications and Assumptions

Throughout this study many assumptions and approximations have been made, in part to set reasonable values for the many free parameters and in part to simplify the mathematical treatment of the problem. The guidelines used to choose plausible numbers for the free parameters have largely been discussed above. The assumptions used to make the problem of emission-absorption blending tractable will now be examined for possible influence on the results of this study.

The first limitation of our treatment was the choice of Roche geometry to describe the close binary X-ray systems. This choice contains many assumptions: point masses, circular orbit, synchronized rotation and revolution and neglect of forces other than that of gravity. The small eccentricity of the Cygnus X-1 system indicates that its deviation from a circular orbit will have little effect on the use of the Roche lobe as a critical surface. Bolton (1975a) shows that this nonzero eccentricity may have some interesting effects on the nature of the mass transfer however, and he cites evidence that HDE226868 is, in fact, near its Roche surface. Apparently, violation of the point mass requirement by actual stars has little effect on the Roche geometry in practice

(Kondo 1974) since the approximation has been used with some success in describing the behavior of normal, eclipsing, close binaries. The synchronization of rotation and revolution is consistent with the circularization of the orbit as noted earlier (Section II), and also with the similarity of the observed rotational velocity and that predicted by the blending models of this paper (below). As for other forces, Bolton (1975a) has shown that radiation pressure affects the use of the Roche lobe as a critical surface only slightly. For a stellar wind with velocity 2000 km/s (Morton 1969) to exert a pressure comparable to that of the radiation pressure near the surface of a star with a temperature of 30,000 °K, a wind mass loss of 2×10^{-6} $M_\odot$/yr would be required. Such a large mass loss would be hard to explain. Apparently the Roche geometry is valid for this system, and it is likely that the primary is close to this surface. The consistency of the Roche lobe size of the reference model and the expected size of an 18 $M_\odot$ early supergiant was noted earlier and confirms this picture. Such a picture also requires that the primary be in hydrostatic and radiative equilibrium to guarantee a moderate mass loss rate.

The alternative to a Roche lobe overflow model is wind accretion as noted earlier. Such a model allows the primary to be smaller than its Roche surface, and although there is evidence to favor overflow accretion over the wind model

(Bolton, 1975a), it is interesting to see what effect a smaller size primary would have on the results of our investigation. The higher inclination angles accessible to these models can be accommodated by the blending mechanism - the solution surface of Section III will expand and the disk emission will scale in like fashion (below). The reduced rotational broadening due to the smaller primary radius will be offset by the higher inclination angle, but this should be a small effect. Higher inclinations in general will be required for these less distorted primarys to fit the observed light curve.

The choice $i = i_{crit}$ is only weakly supported by observations (Section II), and the success of the blending mechanism at this inclination angle is significant in that failure in this case would have made this entire effect improbable (Figure 2). This high inclination is consistent with other predictions of the low-mass-secondary models as well (below). In particular, such an angle should be consistent with the observed light curve which Hutchings et al. (1973) interpret as belonging to a low-inclination, high-mass-secondary system. Nevertheless, it is interesting to speculate on the importance of blending in a lower inclination system. The results of Section III show that the choice $i = 30°$ limits the range of acceptable emission lines (Figure 18) to narrower, slightly lower-V_e lines than

those in the higher inclination reference surface (Figure 9). The actual emission expected from a disk at this inclination should scale in a similar way. Narrower lines are guaranteed by the reduced velocity dispersion and slightly slower lines should result from the less attenuated contribution of the lower-radial-velocity far side of the disk. Higher lines should also be produced by the lower optical depth of a low inclination disk in accord with the shift to higher-H lines in Figure 18. Therefore low inclination gas models may produce emission within the solution volume of Section III. The smaller volume associated with low inclinations does in general make such low i blending models more contrived than those at higher angles.

The use of the light curve for Cygnus X-1 as a constraint on our models has been neglected for several reasons. The prediction of an inclination angle from the light curve relies on sophisticated light curve synthesis techniques which must use many poorly determined parameters in its application. The simplified treatments of the Cygnus X-1 system which yield low values for i (e.g. Bolton 1975a) are based on a poorly determined light curve (see Lyutyi et al. 1973) and use the linear limb darkening coefficients appropriate for normal stars. The validity of such an approximation is uncertain. Also, uncertainties in the chosen gravity darkening coefficient make the result less convincing.

Finally, the high secondary/primary mass ratio deduced from the observed mass function is used in determining the shape of the primary for derivation of the inclination estimate. The purpose of the present investigation is to evaluate the reliability of this mass function in mass determinations and so we must explicitly question any conclusions resulting from its use. Thus we see that the light curve is of more use in confirming the consistency of a model than it is in constraining such a model. This fact is a direct consequence of the uniqueness problems inherent in light curve synthesis methods - especially in noneclipsing systems. Application of the simple ellipsoidal light curve analysis (Russell and Merrill 1952) to the low-mass models of this paper yields angles much greater than 30°. In fact, the range of inclination angles defined by uncertainties in the limb darkening and gravity darkening coefficients includes the critical inclination angle (57°) for our reference model. Application of the detailed light curve synthesis programs of Avni and Bahcall (1975) to our low-mass models could further underscore the consistency of the observed light curve and a distorted velocity curve.

The few approximations made in Section III have been discussed there and shown to be conservative.

The most important approximations made in Section IV were designed to make the transfer problem tractable. Limiting the problem to consideration of the quadrature

configuration has two advantages. First, it is a severe test of the blending mechanism as noted earlier. Second, it allows us to treat line blending as an addition of intensities, thereby simplifying the transfer problem somewhat. The isotropic reradiation of stellar light by scattering from a disk can be considered separately from the description of the light received directly from the stars. The assumption of a radiation dominated gas to simplify solution of the statistical equilibrium equations was not used in practice; all collisional rates were calculated. Comparison of the radiative and collisional rates verified this assumption however, for the Hβ transition. Only in the highest transitions considered did collisions become important. This response of the gas to nonlocal conditions is important in producing the enhanced emission.

The thin gas approximation is central to our derivation of emission profiles. This single scattering picture allows considerable simplification of the transfer integrals in that the disk self-radiation need not be considered in the computation of level populations. Consistency checks on this assumption had discouraging results for our preliminary line estimates (Table 5). The detailed treatment drastically reduced these large optical depths, but some problems remain. While remaining thin in the continuum, gas model 1 was moderately thick ($\tau \simeq 100$) in some parts of the disk at line

center. The seven other models considered were generally thinner. Rigorously, an exact treatment of the transfer problem is required to include the effects of multiple scattering. However, as we are interested only in rough estimates for the lines and are limited by the assumption of gaussian profiles, our treatment should suffice if we note the following. The low collisional rates indicate that the thermalization depth is much smaller than the stream size ($\tau_{th} \simeq 10^{-3}\tau$); line photons not immediately escaping the disk will propagate in the line, possibly broadened by electron scattering, until they do. Retention of Hβ photons by a moderately thick cloud is not likely to diminish the line strength directly by significant heating of the gas. Only level populations in a small part of the disk should be affected by this multiple scattering. While the influence of the two stars on the disk may become slightly separated in a more exact treatment, generally we expect the emission to be enhanced as more line radiation is scattered into the line of sight, continuum radiation being only slightly affected. Thus the derived H and EW of Tables 7-9 should be regarded as being a bit underestimated by the thin treatment. Similarly, the omission of any scattering source terms in line and continuum emissivities, and the neglect of all but thermal Doppler broadening mechanisms to simplify the transfer integrals, contribute to the under-

estimation of W and H and to the overestimation of τ. Note that the implied corrections to the derived lines should not move them out of the solution volume.

The equivalence of the line opacity and emissivity profiles ϕ_λ and χ_λ appropriate for complete redistribution was assumed in Section IV. Such an approximation is justified in the present case because the thermal Doppler effect yields complete redistribution over most of a resonance line profile (Jeffries 1968). Moreover, irradiation by the primary and secondary is of almost constant intensity across the absorption line profile. In the case of a thin disk, such a situation guarantees this equivalence as well.

Finally, with respect to transfer approximations, we note that our results are not sensitive to the choice of n. A larger number of bound states considered in the statistical equilibrium program did not alter the populations in this transition significantly.

Several restrictions were made in the description of gas models considered in Section IV. A Keplerian velocity field was assumed for the disk for simplicity and is good near the secondary. The nature of the velocity field far from the secondary is not Keplerian. For example, the Keplerian velocity of the inner Lagrangian point about the secondary would be 190 km/s; its actual speed is 95 km/s. Effects of a stellar wind and of the mass flow injection velocity make

the actual velocity field difficult to predict. We ncte however, that modification of the Keplerian approximation may be important at phases other than quadrature: at such phases the possible effects of a stellar-wind-induced phase shift in the emission velocity curve would be expected. These effects may still be negligible however, especially near conjunction, if emission line strength decreases away from quadrature. Such behavior is expected if occultation by, and eclipsing of, the emission region occurs, or if the projected geometry of the region becomes unfavorable to scattering. Weakening of unblended emission near conjunction is observed in Cygnus X-1 (Smith et al. 1973). If at conjunction, significant emission survives, either of two effects may obtain. (1) Emission may become unblended, exposing the true absorption line velocity for the primary; (2) emission may remain blended, yielding a spurious eccentricity in the velocity curve data.

The most important limitation of our results comes from the assumed homogeneity of the disk models. Treatment of the detailed structure of a more realistic gas model is a problem of considerable magnitude and quickly becomes unwieldy because of the rapid increase of free parameters. We will satisfy ourselves with discussing observational tests for the blending mechanism which the results of this simpler approach suggest (below).

Extension of our results to other lines and orbital phases may be done easily only in a qualitative way. The line behavior will be discussed below. With respect to the phase behavior we only note that the observed decrease of unblended emission near conjunction, the high inclination of our models and the favoring of large disk models for emission imply that emission contamination should decrease away from quadrature in a manner consistent with the distortion requirements of Figure 3.

The qualifications of our treatment are not severe and our results are intact.

C. Other Implications of Low-Mass Models

To consolidate the success of this study we now make note of other consistencies of this model.

If such emission is to arise generally in X-ray binaries containing early primaries, we should expect a variety of effects manifested in the velocity curves of these objects. Some systems may not exhibit any regular emission; however, those in which conditions allow significant emission in many lines may give rise to three possibilities: a) unblended emission, yielding a readily interpreted velocity curve for the primary, b) partial blending, yielding distorted absorption lines and line-dependent velocity curves and c) frequent blending where systematic velocity curve distortion

is possible. Cases a) and b) are observed, as mentioned in Section IB and Case c) has been shown to be possible for HDE226868.

The consistency of this model with the observed light curve has been mentioned above. The observed primary's projected rotational velocity of $\sim$ 100 km/s (corrected for macroturbulence, Bolton 1975a) is consistent with that of the reference model of Table 1 if blending is occurring. The blending model is also compatible with the stream models for unblended emission as noted earlier. In these models emission arises from the region where the stream contacts the disk, off the line of centers in the trailing hemisphere (e.g. Bolton 1975a). Finally, we speculate that small changes in the disk's emission properties may help explain the scatter in the radial velocity curve data. Such a source of variation would not necessarily be periodic and so would not be detected in a power spectrum analysis of curve residuals.

D. Tests for Blending Effects

This paper has developed the theory of emission line contamination in Cygnus X-1 to the point where observational tests of the velocity curve distortion mechanism can have significant impact on the verification of the black hole candidacy of this object. However, detection of distorting

emission lines may be difficult. Systematic emission-absorption blending may produce shifted absorption lines with little profile distortion. Thus individual profiles need not show clear evidence of this blending; nor would the observed velocity curve shape show such evidence since the sinusoidal nature of the actual radial velocity curve may be maintained by the emission line blending mechanism. Measurement of velocities by line bisection, while giving 'true' velocities for blends such as that in Figure 6B, would not alter the results of line center measurements on the more typical lines such as that in Figure 4A. Furthermore, the strict limits on emission strength built into the blending requirements make subtraction of a standard spectrum to reveal the emission difficult. Differential line behavior - the dispersion of velocities, or variations in other phase dependent characteristics, among lines - is most likely to betray the presence of weak, distorting emission.

The higher Balmer lines in the primary spectrum are Stark broadened and so will tend to increase a bit in strength with respect to Hβ (becoming a bit deeper in the core and wider in the wings). Such lines require less energetic emission lines to effect a small shift in the position of the minimum. The manner in which the corresponding emission lines behave along the series determines

the extent to which such differential behavior will be significant among the blends. While the actual scaling of the higher emission Balmer lines is controlled by stream geometry and may be sensitive to the nature of transfer through the stream, several general observations can be made. These lines will tend to be more strongly influenced by collisions and so will more clearly reflect local conditions: the relative level populations will be governed by T_e. Consequently the gradual decrease of intensities along the series characteristic of thermal spectra might be expected. Widths should increase a bit as broadening becomes more significant, while values for V_e will not change greatly once the (common) stream geometry is specified. Thus the relative scaling of emission and absorption lines permits similar blends to form along the series and admits the possibility of low velocity dispersion among the blends. These results are interesting in that velocity dispersions for lines in HDE226868 are not large ($\leq$ 10 km sec^{-1}). Another consequence of relative scaling is the possible early termination of the blend Balmer series. In the Vela X-1 system the observed series terminates too early for the spectral type (Zuiderwijk et al. 1974); a similar effect may be expected in HDE226868. For other lines, the procedures of this study may be repeated. It should be noted that the absorption lines used in radial velocity determinations have strengths comparable to the

hydrogen lines considered above and so should not require unreasonably strong emission for a significant shift of line minimum.

Examination of radial velocities for various groups of lines may yield clues to the presence of such emission: grouping by excitation or width (acceptable emission lines are sensitive to primary line width - Section III) could reveal emission effects. A similar analysis of the line velocities of the 3U 0900-40 system (Zuiderwijk et al. 1974) gave significant amplitude variations in the velocity curve. Also of particular interest in this regard are blends, multiplets or other proximate lines in the primary spectrum - emission from the neighboring transition may produce unusual separation in the blend and cause significant phase variations in its shape. A study of phase-dependent asymmetries of the lines may also reveal emission blending in some lines (although the blending suggested here has selected against heavily distorted lines). In general, wings alternating in strength with phase, possibly with decreased core depth at conjunction, are expected. This phase behavior also distinguishes between the type of spectral contamination considered in this paper and that commonly associated with hot supergiants in general.

It has been shown that emission naturally arising in X-ray binaries with early primaries can theoretically inter-

act with the primary spectrum in such a way as to mask the real velocity curve and so lead to significant overestimation of the mass of the compact component. Such an effect casts considerable doubt on the black hole candicacy of Cygnus X-1. The nature of this effect also explains the uniqueness of the Cygnus X-1 system. Observational tests for this effect have also been suggested which rely on the possible sensitivity of different spectral lines to such distortion. Failure to detect such emission contamination will require consideration of lines other than Hβ. Such a study would then be needed to define the limits of differential line behavior and so decide the true importance of emission blending in these systems.

VI. BIBLIOGRAPHY

Abhyankar, K. D. 1959. Astrophys. J. Suppl. Ser. 4, 157.

Abramowicz, M. A. and Wagoner, R. V. 1976. Astrophys. J. 204, 896.

Allen, C. W. 1973. Astrophysical Quantities. (Athlone Press, London).

Auer, L. H. and Mihalas, D. 1972. Astrophys. J. Suppl. Ser. 24, 193.

Avni, Y. and Bahcall, J. N. 1975. Astrophys. J. 197, 675.

Bahcall, J. N., Dyson, F. J., Katz, J. I. and Paczynsky, B. 1974. Astrophys. J. Letters 189, L17.

Bahcall, J. N., Rosenbluth, M. N. and Kulsrud, R. M. 1973. Nature Phys. Sci. 243, 27.

Batten, A. H. 1973a. Binary and Multiple Systems of Stars. (Pergamon Press, Oxford).

Batten, A. H. 1973b. Flow of matter within binary systems. In Extended Atmospheres and Circumstellar Matter in Spectroscopic Binary Systems, edited by A. H. Batten. (D. Reidel Publ. Co., Boston), p. 1.

Bessell, M. S., Peterson, B. A., Wickramasinghe, D. T. and Vidal, N. V. 1974. Astrophys. J. 187, 355.

Biermann, P. 1971. Astron. Astrophys. 10, 205.

Bludman, S. A. 1973. Astrophys. J. 183, 649.

Blumenthal, G. A. and Tucker, W. H. 1974. Ann. Rev. Astron. Astrophys. 12, 23.

Bolton, C. T. 1972. Nature Phys. Sci. 240, 124.

Bolton, C. T. 1975a. Astrophys. J. 200, 269.

Bolton, C. T. 1975b. (Private communication).

Bolton, C. T. 1977. (Private communication).

Brecher, K. and Caporaso, G. 1975. Bull. Ann. Astron. Soc. 7, 546.

Brecher, K. and Morrison, P. 1973. Astrophys. J. Letters 180, L107.

Bregman, J., Butler, D., Kemper, E., Koski, A., Kraft, R. P. and Stone, R. P. S. 1973. Astrophys. J. Letters 185, L117.

Brucato, R. J. and Kristian, J. 1973. Astrophys. J. Letters 179, L129.

Brucato, R. J. and Zappala, R. R. 1974. Astrophys. J. Letters 189, L71.

Buerger, P. 1969. Astrophys. J. 158, 1151.

Cowley, C. R. 1970. The Theory of Stellar Spectra. (Gordon and Breach, New York).

Davidson, K. and Ostriker, J. P. 1973. Astrophys. J. 179, 585.

Fabian, A. C., Pringle, J. E. and Whelan, J. A. J. 1974. Nature 247, 351.

Gott, J. R. 1972. Astrophys. J. 173, 227.

Hegyi, D. J. 1977. Astrophys. J. 217, 244.

Hegyi, D. J., Lee, T. S. H. and Cohen, J. M. 1975. Astrophys. J. 201, 462.

Hutchings, J. B. 1973. Astrophys. J. 180, 501.

Hutchings, J. B. 1974. Astrophys. J. Letters 193, L61.

Hutchings, J. B. 1977. Astrophys. J. 217, 537.

Hutchings, J. B., Cowley, A. P., Crampton, D., Fahlmann, G., Glaspey, J. W. and Walker, G. A. H. 1974. Astrophys. J. 191, 743.

Hutchings, J. B., Crampton, D., Glaspey, J. and Walker, G. A. H. 1973. Astrophys. J. 182, 549.

Jeffries, J. T. 1968. Spectral Line Formation. (Blaisdell Pub. Co., Toronto).

Joss, P. C., McClintock, J. E. and Rappaport, S. A. 1975. Bull. Ann. Astron. Soc. 7, 525.

Kaplan, S. A. and Pikelner, S. B. 1970. The Interstellar Medium. (Harvard Univ. Press, Cambridge, Mass.).

Kondo, Y. 1974. Astrophys. Space Sci. 27, 293.

Kopal, Z. 1959. Close Binary Systems. (Wiley, New York), Ch. 3.

Lamb, D. Q. and Van Horn, H. M. 1973. Astrophys. J. 183, 959.

Lyutyi, V. M., Syunyaev, R. A. and Cherepashchuk, A. M. 1973. Soviet Astron. 17, 1.

Margon, B., Bowyer, S. and Stone, R. P. S. 1973. Astrophys. J. Letters 185, L113.

Mason, K. O., Hawkins, F. J., Sanford, P. W., Murdin, P. and Savage, A. 1974. Astrophys. J. Letters 192, L65.

Mauder, H. 1973. Astron. Astrophys. 28, 473.

Mihalas, D. 1964. Astrophys. J. Suppl. Ser. 9, 321.

Mikkelsen, D. R. 1977. Astrophys. J. 217, 248.

Milgrom, M. 1976. Astrophys. J. 207, 902.

Morton, D. C. 1969. Astrophys. Space Sci. 3, 117.

Murdin, P. 1975. (Private communication).

Oda, M., Govenstein, P., Gursky, H., Kellogg, E., Schreier, E., Tananbaum, H. and Giacconi, R. 1971. Astrophys. J. Letters 166, L1.

Osmer, P. S. and Hiltner, W. A. 1974. Astrophys. J. Letters 188, L5.

Plavec, M. 1970. Publ. Astron. Soc. Pacific 82, 957.

Pratt, J. P. and Strittmatter, P. A. 1976. Astrophys. J. Letters 204, L29.

Prendergast, K. H. 1960. Astrophys. J. 132, 162.

Press, W. H., Witta, P. J. and Smarr, L. 1975. Astrophys. J. Letters 202, L135.

Pringle, J. E. and Rees, M. J. 1972. Astron. Astrophys. 21, 1.

Russell, H. N. and Merrill, J. E. 1952. Contr. Princeton Univ. Obs. 26, 1.

Schuerman, D. W. 1972. Astrophys. Space Sci. 19, 351.

Smith, H. E., Margon, B. and Conti, P. S. 1973. Astrophys. J. Letters 179, L125.

Spitzer, L. 1968. Diffuse Matter in Space. (Interscience, New York).

Tananbaum, H., Gursky, H., Kellogg, E., Giacconi, R. and Jones, C. 1972. Astrophys. J. Letters 177, L5.

Tatum, J. B. 1968. Monthly Notices. Roy. Astron. Soc. 141, 43.

Trimble, V., Rose, W. K. and Weber, J. 1973. Monthly Notices Roy. Astron. Soc. 162, 1p.

Walborn, N. R. 1973. Astrophys. J. Letters 179, L123.

Webster, B. L. and Murdin, P. 1972. Nature 235, 37.

Wheeler, J. A., Misner, C. W. and Thorne, K. S. 1973. Gravitation. (Freeman and Company, San Francisco), Ch. 44.

Wickramasinghe, D. T., Vidal, N. V., Bessell, M. S., Peterson, B. A. and Perry, M. E. 1974. Astrophys. J. 188, 167.

Wiese, W. L., Smith, M. W. and Glennon, B. M. 1969. Atomic Transition Probabilities I. (U.S. Nat. Bur. Stnd., Washington).

Wolff, S. C. and Morrison, N. D. 1974. Astrophys. J. 187, 69.

Zeldovich, Ya. B. and Novikov, I. D. 1971. Stars and Relativity. (University of Chicago Press, Chicago), Ch. 10.

Zuiderwijk, E. J., van den Heuvel, E. P. J. and Hensberge, G. 1974. Astron. Astrophys. 35, 353.

VII. ACKNOWLEDGMENTS

It is a pleasure to acknowledge the people who have offered their support during this investigation.

I thank Dr. Dennis Ross for introducing me to Cygnus X-1, for his encouragement of independent inquiry and for his critical review of this work. I thank Drs. D. K. Ross, L. A. Willson and A. S. Grossman for many helpful discussions. I also thank Pat Gunnells for her expeditious and highly competent typing of the manuscript.

I especially thank my parents for their unselfish encouragement of growth, and my wife Debby for her patience and constant support of this effort.

VIII. APPENDIX: COMPUTATIONAL TECHNIQUES

A. Methods and Tests

This investigation has been structured around three major computational goals: generation of low-mass binary models, generation of emission lines able to distort an absorption line in a particular way, and generation of emission lines produced by gas which finds itself in an X-ray binary. To carry out these computations, five sequential computer programs were developed. This development was influenced by the large number of free parameters under investigation, by the associated high volume of generated data and by limited computer time. Consequently, these programs are generally responsive to variation of all important free parameters, display output data in a manner conducive to easy analysis and are very efficient. These programs are briefly described below.

GRDGEN:

The program GRDGEN (Grid Generator) performs the calculations of Section II. It uses one and two-dimensional Newton-Raphson techniques to solve the normalized equations of Roche geometry and thereby generates a grid of binary models for Cygnus X-1 each containing a low-mass secondary. The Roche functions proved to be well-behaved and convergence was rapid with this technique. The program

was able to reproduce the tables of normalized Roche parameters given by Kopal (1959). The generated critical inclination angles were good for all secondary/primary mass ratios. They also verified the values derived for the high mass ratio approximation (e.g., Brucato and Kristian 1973).

BLNDER:

The program BLNDER (line blender) performs the calculations of Section III. It uses a model from GRDGEN to modify a given absorption line and then finds emission lines able to distort this modified line to the observed shape. Solution of Equation (16) for S, given a large grid of H, W values, and the associated distortion tests, presented some problems in that large computing times were predicted. Considerable efficiency in these calculations was achieved by the development of a test to predict the number and approximate location of roots for each H, W point with little computational work. A bisection technique then produced rapid convergence to the appropriate root with more accuracy than required by observations. Similarly, computation time spent in distortion evaluation was considerably reduced by choosing an appropriate order for the distortion tests, and by taking full advantage of the properties of gaussian profile shapes.

The data display options offered by BLNDER make trends in the derived lines very clear. The 2-D and 3-D repre-

sentations were developed and were available in any combination, with or without an explicit record of the derived parameters. The apparent limitation of the 2-D picture - only ten symbols to represent the entire velocity range of a surface - was removed by allowing specification of the desired resolution. For higher resolution, more plots were generated, each using ten symbols to cover a smaller region of the surface. The sorting routines for these data displays proved to be fairly efficient. BLNDER also permits the plotting of individual blends chosen from a surface to check the consistency and accuracy of the distortion tests. The profiles of Figures 4-6 were drawn in this way. Finally, BLNDER produces a sample of the Keplerian velocity field about the input secondary for comparison with the derived emission line velocities.

POPGEN:

The program POPGEN, (population generator) and the following two programs, perform the calculations of Section IV. For a given gas flow model, POPGEN solves the statistical equilibrium equations for the level populations, computes opacities and emissivities and estimates crude emission line shapes for F = .001 and a particular line of sight dimension. All collisional and radiative rates are calculated and displayed. The numerical integrations for

the radiation fields were tested on known functions of similar behavior with success. A library matrix-diagonalizing routine was used for the solution for populations. Appropriate test choices for W_1, W_2, T_e, and N_e gave the thermal equilibrium population ratios. Line properties (H, W, EW, line center optical depth) were estimated for three ϕ_λ, χ_λ widths: thermal, 1Å, 4Å. W was estimated by stepping from line center in these profiles until the HWHM was reached in the generated $H(\lambda)$ line (Equation 29).

PROGEN:

The program PROGEN (profile generator) uses the opacities and emissivities of POPGEN to produce, point by point, a detailed emission profile for a specific Keplerian disk. The four-fold integration for the total flux (Equation 31) required the solution of an underlying geometry problem. For each point in the disk, the optical depth must be determined, and so the points of intersection of the line of sight with the boundaries of the disk (up to four points) must be derived for limits on the τ integration. The problem was time consuming, but a high degree of efficiency was attained by taking full advantage of the properties of disk geometry and by computing, simultaneously, the physical depths of each point for use in the continuum flux integration. The integrations were done with

combinations of 16-, 24- and 32-point gauss quadrature, corresponding to an average of about 3×10^5 integration points per model. Numerical experiments were carried out to determine the combination required to optimize the accuracy and computation time for a profile. To guarantee low oscillations in the derived profiles, relatively long computation times were required for each point. Consequently this program was written for use on the accessible PDP 11 rather than for the expensive IBM machine. This numerical method was initially tested on known integrals with success. PROGEN also monitors the maximum τ encountered in its integration over the disk and reports it for a check on the thin gas approximation.

PROFIT:

The program PROFIT (profile fit) displays the profile data generated by PROGEN, in terms of either H or flux relative to the primary. Smooth curve fits or gaussian fits to the data may be specified. In the later case, provision is made to restrict the fitting region. The gaussian fit parameters are reported with the plot.

B. Computer Codes

A listing of these programs follows. It should be noted that they were written for the case of Cygnus X-1 with Hβ at the .25 quadrature, and so will need some modifications to handle other cases.

```
C
C
C       PROGRAM CODE: GRDGEN
C
C            THIS PROGRAM OUTPUTS AN MX,M GRID OF BINARY MODELS
C            WITH PERIOD AND ECCENTRICITY OF CYGNUS X-1 AT A GIVEN
C            INCLINATION OR AT CRITICAL ECLIPSE INCLINATION
C            DIMENSIONS ARE REPORTED IN SOLAR RADIUS UNITS AND IN UNITS
C            NORMALIZED TO PAIR SEPARATION
C            DISTANCES ARE MEASURED FROM PRIMARY C OF M
C            OUTPUT:  SYSTEM C OF M
C                     INNER LAGRANGIAN POINT POSITION
C                     SECONDARY POSITION
C                     MEAN ROCHE LOBE RADII
C                     SEMI-MAJOR AXES Z7,Y5,X1
C                     INCLINATION ANGLE
C                     ALL ACTUAL AND PROJECTED VELOCITIES
C
C
      IMPLICIT REAL*8 (A-H,O-Z)
      REAL*8 M,MX,M0,MX0,MSTP,MXSTP
C
C     READ IN STEPPING CONDITIONS AND INCLINATION MODE
C          DEGMOD>90 GIVES CRITICAL INCLINATION ASPECT
C          DEGMOD<90 GIVES INCLINATION I=DEGMOD
C
      READ(5,100) MX0,MXSTP,NMX,M0,MSTP,NM
      READ(5,100) DEGMOD
C
C     EPSI IS FOR X1
C     EPSID IS FOR JACOBIAN IN X0,Z0,X5,Z7
C     EPSIF IS FOR X0,Z0,X5,Z7
C     EPSIFY IS FOR Y5
C     EPSIN IS FOR YPR IN X1,Y5
C     NFLGLM IS LIMIT OF ITERATIONS UNTESTED FOR DIVERGENCE IN THE 1-D
C          NEWTON RAPHSON ROUTINES
C     LCON IS THE SAME PARAMETER FOR THE 2-D ROUTINES
C     MXIT** DESIGNATE ITERATION MAXIMA
      NFLGLM=5
      LCON=5
      MXITX1=25
      MXITX0=50
      MXITX5=50
      MXITY5=25
      EPSI = .00001D0
      EPSIF=.00001D0
      EPSIFY=.00001D0
      EPSID=.0005D0
      EPSIN=.0005D0
      A=1.D0/3.D0
```

```
      AB=-.5D0
      AC=-1.5D0
      AD=-2.5D0
      APER=5.6025D0/365.26D0
      TPI=6.28318530717959
      DEGCOR=360.D0/TPI
      SUNCOR=1496.D0/6.96D0
      CORFAC=14.960D0/3.1558D0
      ERGCOR=66.70D0*1.989D0/6.960D0
C
C     INITIATE STEPPING
C
      N=-1
      DO 1 L=1,NMX
      MX=MX0+(L-1)*MXSTP
      DO 2 K=1,NM
      M=M0+(K-1)*MSTP
      N=N+1
      F=MX/M
      IF(N/3*3 .EQ. N) WRITE(6,200)
      WRITE(6,201) MX,M,F
      AU=((APER**2)*(MX+M))**A
      AUSUN=AU*SUNCOR
      CM=MX/(MX+M)
      CMS=CM*AUSUN
C
C     FIND X1
C
      C=1.D0+F
      D=2.D0+3.D0*F
      E=1.D0+3.D0*F
      X=.5D0
      NFLG=1
    3 Y=C*(X**5)-D*(X**4)+E*(X**3)-(X**2)+2.D0*X-1.D0
      Z=DABS(Y)
      IF(Z.LE.EPSI) GO TO 4
      NFLG=NFLG+1
      IF(NFLG .GT. MXITX1) GO TO 5
      YPR=5.D0*C*(X**4)-4.D0*D*(X**3)+3.D0*E*(X**2)-2.D0*X+2.D0
      ABYPR=DABS(YPR)
      IF(ABYPR .LT. EPSIN) GO TO 6
      YOYPR=Y/YPR
      X=X-YOYPR
      IF(NFLG .LT. NFLGLM) GO TO 3
      IF(X.GT.1. .OR. X.LT. 0.) GO TO 7
      GO TO 3
    6 WRITE(6,203) NFLG,X
      GO TO 20
    7 WRITE(6,204) NFLG,X
      GO TO 20
```

```
    5 WRITE(6,202)
    4 X1=X
C
C       FIND RMEAN
C
        AA=2.D0*F/(1.D0-X1)
        BB=AA+F+1.D0
        CC=2.D0+(X1**3)*BB
        RMN=2.D0*X1/CC
        OMEGA1=(1.D0/X1)+F*((1.D0/(1.D0-X1))-X1)+(((F+1.D0)*X1*X1)/2.D0)
C
C       FIND RM2
C
        X1=1.D0-X1
        F=1.D0/F
        AA=2.D0*F/(1.D0-X1)
        BB=AA+F+1.D0
        CC=2.D0+(X1**3)*BB
        RM2=2.D0*X1/CC
        X1=1.D0-X1
        F=1.D0/F
C
C       FIND RVOL
C
        RZ=1.D0/(OMEGA1-F)
        RZ3=RZ**3
        RZ6=RZ3**2
        A0=(F**2)*RZ6
        A1=1.D0+12.D0*A0/5.D0+15.D0*A0*RZ*RZ/7.D0+2.D0*A0*(RZ**4)
        A2=(F*RZ3)**3
        A3=22.D0*A2/7.D0+157.D0*A2*RZ*RZ/7.D0
        A4=(F+1.D0)/2.D0
        A5=2.D0*A4*RZ3
        A6=A5*(1.D0+A4*RZ6*(16.D0/5.D0+88.D0*A4/7.D0))
        A7=8.D0*A4*F*RZ6/5.D0
        A8=A7*(1.D0+37.D0*RZ3*(2.D0*F+A4)/7.D0)
        A9=26.D0*A4*F*(F+3.D0*A4)*(RZ6**2)/(35.D0*RZ)
        A10=(A1+A3+A6+A8+A9)**A
        RVOL=RZ*A10
C
C       CHANGE TO SOLAR UNITS AND DISPLAY
C
        X1S=X1*AUSUN
        RMNS=RMN*AUSUN
        RM2S=RM2*AUSUN
        RVOLS=RVOL*AUSUN
        WRITE(6,209) AUSUN,X1,CM,RVOL,RMN,RM2
        WRITE(6,223) X1S,CMS,RVOLS,RMNS,RM2S
        IF(DEGMOD .LE. 90.D0) GO TO 8
```

```
C
C      FIND X0,Z0 FOR CRITICAL ECLIPSE INCLINATION
C
       Z=RMN
       X=0.D0
       LCONVG=0
       NECHO=0
   13  W0=(X*X)+(Z*Z)
       W1=X-1.D0
       W2=W0-X
       W3=W2-W1
       W4=X*W1
       W5=W3**AB
       W0X=2.D0*X
       W0Z=2.D0*Z
       W2X=W0X-1.D0
       W3X=W2X-1.D0
       W5X=AB*(W3**AC)*W3X
       W5Z=AB*(W3**AC)*W0Z
       W0AC=-1.D0*(W0**AC)
       W0CD=-1.D0*AC*W2*(W0**AD)
       F1=W0AC*W2-F*(W5+W1)+(F+1.D0)*W4
       F2=(W0**AB)+F*(W5-X)+(((F+1.D0)*X*X)/2.D0)-OMEGA1
       F1X=W0CD*W0X+W0AC*W2X-F*(W5X-1.D0)+(F+1.D0)*W2X
       F1Z=W0Z*(W0CD+W0AC)-F*W5Z
       F2X=-1.D0*AB*W0AC*W0X+F*(W5X-1.D0)+(F+1.D0)*X
       F2Z=-1.D0*AB*W0AC*W0Z+F*W5Z
       DXZ=F1X*F2Z-F1Z*F2X
       ABDXZ=DABS(DXZ)
       ABF1=DABS(F1)
       ABF2=DABS(F2)
       IF(ABDXZ .LT. EPSID) GO TO  9
       GO TO  10
    9  WRITE(6,205) LCONVG
       GO TO 20
   10  IF(ABF1 .LT. EPSIF .AND. ABF2 .LT. EPSIF) GO TO  11
       LCONVG=LCONVG+1
       IF(LCONVG .GT. MXITX0) GO TO 12
       T0=F2*F1Z-F1*F2Z
       T1=F1*F2X-F2*F1X
       X=X+(T0/DXZ)
       Z=Z+(T1/DXZ)
       IF(LCONVG .LT. LCON) GO TO 13
       IF(X .GT. XI .OR. X .LT. -1.*X1) GO TO 14
   15  CONTINUE
       IF(Z .LE. 0.) GO TO 16
   17  CONTINUE
       IF(NECHO .NE. 0) GO TO 20
       GO TO 13
```

```
   14 WRITE(6,207) LCONVG,X
      NECHO=1
      GO TO 15
   16 WRITE(6,208) LCONVG,Z
      NECHO=1
      GO TO 17
   12 WRITE(6,206) ABF1,ABF2
   11 X0=X
      Z0=Z
C
C     FIND INCLINATION ANGLE AND SINI
C
      TANI=(1.D0-X0)/Z0
      ANGI=DATAN(TANI)
      GO TO 18
    8 ANGI=DEGMOD/DEGCOR
   18 SINI=DSIN(ANGI)
      DEGI=ANGI*DEGCOR
      IF(DEGMOD .LE. 90.D0) GO TO 35
      WRITE(6,211) DEGI,SINI,X0,Z0
      GO TO 36
   35 WRITE(6,210) DEGI,SINI
   36 CONTINUE
C
C     FIND SYSTEM VELOCITIES AND MASS FUNCTION        DISPLAY
C
      V=TPI*AU*CORFAC*CM/APER
      VK1=V*SINI
      VROT=TPI*RMN*AU*CORFAC/APER
      VROTA=VROT*SINI
      FREAL=((MX*SINI)**3)/((MX+M)**2)
      WRITE(6,212) V,VK1,FREAL,VROT,VROTA
C
C     FIND X5, Z7      DISPLAY
C
      X=0.D0
      Z=RMN
      LCONVG=0
      NECHO=0
   24 W0=(X*X)+(Z*Z)
      W1=X-1.D0
      W2=W0-X
      W3=W2-W1
      W5=W3**AB
      W4=W1*AC*(W3**AD)
      W0X=2.D0*X
      W0Z=2.D0*Z
      W3X=W0X-2.D0
      W5X=AB*(W3**AC)*W3X
```

```
      W5Z=AB*(W3**AC)*W0Z
      W0AC=-1.D0*(W0**AC)
      W0CD=-1.D0*AC*(W0**AD)*X
      F1=X*W0AC-F*(W1*(W3**AC)+1.D0)+X*(F+1.D0)
      F2=(W0**AB)+F*(W5-X)+(((F+1.D0)*X*X)/2.D0)-OMEGA1
      F1X=W0AC+W0CD*W0X-F*((W3**AC)+W4*W3X)+F+1.D0
      F1Z=W0CD*W0Z-F*W4*W0Z
      F2X=-1.D0*AB*W0AC*W0X+F*(W5X-1.D0)+(F+1.D0)*X
      F2Z=-1.D0*AB*W0AC*W0Z+F*W5Z
      DXZ=F1X*F2Z-F1Z*F2X
      ABDXZ=DABS(DXZ)
      ABF1=DABS(F1)
      ABF2=DABS(F2)
      IF(ABDXZ .LT. EPSID) GO TO 19
      GO TO 21
   19 WRITE(6,213) LCONVG
      GO TO 20
   21 IF(ABF1 .LT. EPSIF .AND. ABF2 .LT. EPSIF) GO TO 22
      LCONVG=LCONVG+1
      IF(LCONVG .GT. MXITX5) GO TO 23
      T0=F2*F1Z-F1*F2Z
      T1=F1*F2X-F2*F1X
      X=X+(T0/DXZ)
      Z=Z+(T1/DXZ)
      IF(LCONVG .LT. LCON) GO TO 24
      IF(X .GT. X1 .OR. X .LT. -1.*X1) GO TO 25
   26 CONTINUE
      IF(Z .LE. 0.) GO TC 27
   28 CONTINUE
      IF(NECHO .NE. 0) GO TO 20
      GO TO 24
   25 WRITE(6,215) LCONVG,X
      NECHO=1
      GO TO 26
   27 WRITE(6,216) LCONVG,Z
      NECHO=1
      GO TO 28
   23 WRITE(6,214) ABF1,ABF2
   22 X5=X
      Z7=Z
      X5S=X5*AUSUN
      Z7S=Z7*AUSUN
      WRITE(6,220) X5,Z7,X5S,Z7S
C
C     FIND Y5 AND DISPLAY
C
      Y=RMN
      NFLG=1
   33 W0=X5*X5+Y*Y
      W1=((1.D0-X5)**2)+Y*Y
```

```
      F1=W0**AB+F*((W1**AB)-X5)+(((F+1.D0)*W0)/2.D0)-OMEGA1
      ABF1=DABS(F1)
      IF(ABF1 .LT. EPSIFY) GO TO 29
      NFLG=NFLG+1
      IF(NFLG .GT. MXITY5) GO TO 30
      YPR=Y*(AB*(W0**AC)*2.D0+F*AB*(W1**AC)*2.D0+F+1.D0)
      ABYPR=DABS(YPR)
      IF(ABYPR .LT. EPSIN) GO TO 31
      GO TO 32
   31 WRITE(6,218) NFLG,Y
      GO TO 20
   32 CONTINUE
      YOYPR=F1/YPR
      Y=Y-YOYPR
      IF(NFLG .LT. NFLGLM) GO TO 33
      IF(Y .LT. 0. .OR. Y .GT. 1.) GO TO 34
      GO TO 33
   34 WRITE(6,219) NFLG,Y
      GO TO 20
   30 WRITE(6,217) ABF1
   29 Y5=Y
      Y5S=Y5*AUSUN
      WRITE(6,221) Y5,Y5S
C
C     FIND OMEGA  (POTENTIAL OF INNER LAGRANGIAN POINT WRT SECONDARY)
C
   20 CONST1=(ERGCOR*M)/AUSUN
      CONST2=(F*CM)/2.D0
      OMEGA=CONST1*(OMEGA1+CONST2)
      WRITE(6,222) OMEGA
    2 CONTINUE
    1 CONTINUE
      STOP
C
C     FORMAT CARDS
C
  100 FORMAT(2(2F5.1,I3,2X))
  200 FORMAT('1')
  201 FORMAT('  MX= ',F4.1,X,'SOLAR MASSES   MP= ',F4.1,' SOLAR MASSES
     * Q= ',F4.3,//)
  202 FORMAT(' ',20X,'X1 ITERATION MAX EXCEEDED')
  203 FORMAT(' ',20X,'SINGULAR DENOMINATOR ON ITERATION # ',I2,' FOR X1.
     *   X= ',E14.7)
  204 FORMAT(' ',20X,'CONVERGENCE EXIT ON ITERATION # ',I2,' FOR X1.   X
     *= ',E14.7)
  205 FORMAT(' ',20X,'SINGULAR JACOBIAN ON ITERATION # ',I2,' IN X0,Z0 D
     *ETERMINATION')
  206 FORMAT(' ',20X,'X0,Z0 ITERATION MAX EXCEEDED WITH ABF1= ',E14.7,
     *', ABF2= ',E14.7,X)
```

```
207 FORMAT(' ',20X,'X0 CONVERGENCE EXIT ON ITERATION # ',I2,'.  X0= ',
   *E14.7)
208 FORMAT(' ',20X,'Z0 CONVERGENCE EXIT ON ITERATION # ',I2,'.   Z0= '
   *,E14.7)
209 FORMAT(' ',10X,'ASUN= ',F4.1,5X,'X1= ',F4.3,5X,'CM= ',F4.3,5X,
   *'RVOL= ',F4.3,5X,'RMN= ',F4.3,5X,'RM2= ',F4.3,/)
210 FORMAT(' ',20X,'DEGI= ',F4.1,5X,'SINI= ',F4.3,/)
211 FORMAT(' ',20X,'DEGI= ',F4.1,5X,'SINI= ',F4.3,10X,'(CRITICAL ASPEC
   *T:  X0= ',F4.3,'    Z0= ',F4.3,')',/)
212 FORMAT(' ',20X,'V= ',F5.1,5X,'K1= ',F5.1,5X,'F(M) IS REALLY ',
   *F5.4,5X,'VROT= ',F5.1,5X,'VROTA= ',F5.1,/)
213 FORMAT(' ',20X,'SINGULAR JACOBIAN ON ITERATION # ',I2,' IN X5,Z7 D
   *ETERMINATION')
214 FORMAT(' ',20X,'X5,Z7 ITERATION MAX EXCEEDED WITH ABF1= ',E14.7,
   *'   ABF2= ',E14.7)
215 FORMAT(' ',20X,'X5 CONVERGENCE EXIT ON ITERATION # ',I2,'   X5= ',
   *E14.7)
216 FORMAT(' ',20X,'Z7 CONVERGENCE EXIT ON ITERATION # ',I2,'   Z7= ',
   *E14.7)
217 FORMAT(' ',20X,'Y5 ITERATION MAX EXCEEDED WITH ABF1= ',E14.7)
218 FORMAT(' ',20X,'SINGULAR DENOMINATOR ON ITERATION # ',I2,' FOR Y5.
   * Y5= ',E14.7)
219 FORMAT(' ',20X,'Y5 CONVERGENCE EXIT ON ITERATION # ',I2,'   Y5= ',
   *E14.7)
220 FORMAT(' ',20X,'X5= ',F5.3,5X,'Z7= ',F4.3,5X,'X5S= ',F4.1,5X,
   *'Z7S= ',F4.1,/)
221 FORMAT(' ',20X,'Y5= ',F4.3,5X,'Y5S= ',F4.1,/)
222 FORMAT(' ',20X,'OMEGA EQUALS ',E14.7,' IN UNITS OF TEN TO THE 14TH
   * ERGS PER GRAM',///)
223 FORMAT(' ',20X,'X1S= ',F4.1,5X,'CMS= ',F4.1,5X,'RVOLS= ',F4.1,5X,
   *'RMNS= ',F4.1,5X,'RM2S= ',F4.1,/)
    END
```

```
C
C
C      PROGRAM CODE: BLNDER
C
C           THIS PRCGRAM USES A SYSTEM MODEL
C                VR,KAYONE,KAYTWO,VSINI,
C                DEGI,AU,RMN,RMN2,MP,MX,DELONE
C           TO MODIFY AN ABSORPTION LINE
C                LM0,W1, C1  (ANGSTROMS).
C           FOR A RELATIVE CONTINUUM VALUE H IT THEN STEPS THROUGH AN
C           EMISSION LINE HEIGHT-WIDTH GRID
C                C2I,C2STP,NC2,WI,WSTP,NW
C           TO FIND SEPARATION NECESSARY TO DISTORT THIS MODIFIED LINE
C           TO A REQUIRED VELOCITY
C                VREQ,DELREQ
C           ALPHE IS THE RCTATIONAL BROADENING FACTOR, AND NC2LIM ALLCWS
C           RESTRICTION OF THE HEIGHT SEARCH DIMENSION
C           REJECTICN CRITERIA FOR THE DISTCRTION TEST ARE
C                CR,FIR,RSR1,RSR2,RSR3,WR,ARR
C           VRSLV IS THE MINIMUM VELOCITY SEPARATION OF SYMBOLS USED
C           IN THE 2-D DISPLAY
C           CERR, CV ARE CHARACTER ARRAYS OF THE 2-D SYMBOLS
C           NRESL SPECIFIES THE DESIRED RESOLUTICN OF THE 2-D DISPLAY
C           VBOT, VTOP DEFINE LIMITS FOR THE 3-D PLOT
C           NSCH IS A BOOKKEEPING LABEL FOR THE SEARCH
C      THIS PROGRAM MAY ALSO BE USED TO PLOT INDIVIDUAL LINE PRCFILES
C          NGPH CHOOSES GRID SEARCH (0) OR PROFILE PLOTS (1)
C      IF NSCH IS A THREE DIGIT NUMBER, THE FIRST DIGIT INDICATES THE
C      NUMBER OF A PROFILE GRAPHING ROUTINE TAKEN FROM THE SEARCH ROUTINE
C      WHOSE NUMBER IS GIVEN BY THE LAST TWO DIGITS
C
C      DATA MANIPULATION CPTIONS
C
C      NGTD       NTD       RESULT
C       -1          0        2D, STORE
C                   1        2C, STORE, 3D
C        0          0        2D
C                   1        2D
C        1          0        STORE
C                   1        STORE, 3D
C      NOPTN = 1             PRIMARY AND SECONDARY SOLUTIONS FOUND
C            = 0             PRIMARY ONLY, SECONDARY TYPED OUT
C
C           LINE PLOT PARAMETERS ARE
C                NPTS,XSIZ,YSIZ,SYMHT,DATLAB,DATLB,XLAB,YLAB,GLAB
C                RESOOL = LEFT MOST GRAPH POSITION (NORMALIZED UNITS)
C                C2,W,NSOL SPECIFY DESIRED LINE
C                NSOL = 3 IS A DUMMY VALUE INDICATING END OF PRC PLOTS
C
C
```

```
      DIMENSION RTS(2),VMAX(2),VMIN(2),V(11),VSAVE(10),SSEP(11),
     *VLCTY(2,42,91)
      INTEGER*2 NG(2),NB(2),IG1(2),ISAVE(10),JSAVE(10),IORDR(10),
     *JORDR(10),IHTLAB(10)
      DIMENSION XNOR(160), YNOR(160), YCOM(160)
      DIMENSION DATLAB(5), DATLB(5), XLAB(5), YLAB(5), GLAB(5)
      INTEGER*2 CARR(2,42,91), CERR(6), CV(10), CHAR
      LOGICAL*1 IC(2,42,91),IV(2,42,91)
      REAL LM1,LM0,KAYONE,KAYTWO,MP,MX
      COMMON H,C1,C2,W,ALN2,XMN,ARGMNT
      COMMON/SCREEN/CR,FIR,RSR1,RSR2,RSR3,WR,ARR/ODD/ERR
      COMMON/SPEED/WID,LM1,SPLT,LM0,KAYTWO,SINI,VR
      ICODE=0
C
C     INITIALIZE
C
      READ(5,141) CERR
      READ(5,141) CV
      READ(5,132) VBOT, VTOP
      READ(5,137) NSCH
      READ(5,132) VR,KAYONE,KAYTWO,VSINI,VREQ
      READ(5,133) DEGI,AU,RMN,RMN2,MP,MX
      READ(5,134) LM0,W1,C1,H
      READ(5,135) C2I,C2STP,NC2,WI,WSTP,NW
      READ(5,136) CR,FIR,RSR1,RSR2,RSR3,WR,ARR
      READ(5,132) ALPHE
      READ(5,132) VRSLV
      READ(5,133) DELREQ, DELONE
      READ(5,137) NOPTN
      READ(5,137) NRESL
      READ(5,137) NGTD
      READ(5,137) NTD
      READ(5,137) NGPH
      READ(5,137) NC2LIM
C
C     OPTIONAL GRAPH PACK -- INITIALIZATION
C
      IF (NGPH .EQ. 0) GO TO 55
      READ(5,144) RESOOL,NPTS
      READ(5,143) XSIZ, YSIZ, SYMHT
      READ(5,142) DATLAB
      READ(5,142) DATLB
      READ(5,142) XLAB
      READ(5,142) YLAB
      STEPP=2.*RESOOL/(NPTS-1)
      XGLAB=.5*XSIZ-.5
      YGLAB=YSIZ-.5
   55 CONTINUE
      WRITE(6,109) NSCH
      WRITE(6,125) MP,MX,DEGI,AU,RMN,RMN2
```

```
      WRITE(6,126) VR,KAYONE,KAYTWO,VSINI,VREQ
      WRITE(6,127) LM0,W1,C1,H
      WRITE(6,128) ALPHE
      WRITE(6,146) DELREQ, DELONE, VBOT, VTOP
      IF (NGPH .EQ. 1) GO TO 69
      WRITE(6,130) C2I,C2STP,NC2,WI,WSTP,NW
   69 CONTINUE
      WRITE(6,131) CR,FIR,RSR1,RSR2,RSR3,WR,ARR
      SINI=SIN(3.141593*DEGI/180.)
      SPLT=3.*10**5
      ALN2=ALOG(2.)
      CORFAC=1.+(VR+KAYONE+DELONE)/SPLT
      LM1=LM0*CORFAC
      W1D=W1*CORFAC+LM0*VSINI*ALPHE/(2.*SPLT)
      C1=C1*W1/W1D
      XMN=LM0*(VREQ+DELREQ-KAYONE-DELONE)/(W1D*SPLT)
      ERR=LM1*VRSLV/(SPLT*W1D)
      WRITE(6,129) LM1,W1D,XMN,ERR
      IF(XMN .LT. 2.) GO TO 42
      WRITE(6,138)
      GO TO 99
   42 CONTINUE
      NG(1)=0
      NG(2)=0
      NB(1)=0
      NB(2)=0
C
CC    INITIATE STEPPING
C
      DO I I=1,NW
      W=(WI+(NW-I)*WSTP)/W1D
      DO 2 J=I,NC2
      C2=C2I+(J-1)*C2STP
      IF (NGPH .EQ. 0) GO TO 60
      READ(5,145) C2, W, NSOL, GLAB
      W=W/W1D
      IF (NSOL .EQ. 3) GO TO 99
   60 CONTINUE
      ARGMNT=ALN2*XMN*XMN*(1.-W*W)/(W*W)
      DO 58 L=1,2
      IC(L,I,J)= .TRUE.
      IV(L,I,J)= .TRUE.
      VLCTY(L,I,J)=VBOT
      IF (NW .NE. 1 .AND. J .NE. NC2) GO TO 64
      VLCTY(L,I,J)=VTOP
   64 CONTINUE
   58 CARR(L,I,J)=CERR(6)
      IF (J .GT. NC2LIM) GO TO 2
```

```
C
C       INITIATE ROOT SEARCH
C
        CALL SEARCH(NRTS,RT1,RT2)
        IF(NRTS-1) 2,3,4
    4   RTS(2)=RT2
    3   RTS(1)=RT1
        IF(NRTS-1) 2,5,6
C
C       TEST PROFILES AND ASSIGN LABELS
C
    6   IF(NOPTN .EQ. 1) GO TO 5
        CALL PROTST(RT2,INDEX)
        IF(INDEX .NE. 6) GO TO 7
        SPD=VEL(RT2)
        WRITE(6,100) C2,W,RT2,SPD
        NRTS=1
        GO TO 5
    7   CHAR=CERR(INDEX)
        WRITE(6,101) C2,W,RT2,CHAR
        NRTS=1
    5   DO 24 L=1,NRTS
        IC(L,I,J)= .FALSE.
        RT=RTS(L)
        CALL PROTST(RT,INDEX)
        IF(INDEX .EQ. 6) GO TO 8
        CARR(L,I,J)=CERR(INDEX)
        NB(L)=NB(L)+1
        GO TO 24
    8   SPD=VEL(RT)
        IV(L,I,J)= .FALSE.
        VLCTY(L,I,J)=SPD
        NG(L)=NG(L)+1
        IF(NG(L) .NE. 1) GO TO 9
        VMAX(L)=SPD
        VMIN(L)=SPD
        IG1(L)=I
        GO TO 24
    9   VM=VMAX(L)
        VN=VMIN(L)
        VMAX(L)=AMAX1(VM,SPD)
        VMIN(L)=AMIN1(VN,SPD)
   24   CONTINUE
C
C       OPTIONAL GRAPH PACK -- EXECUTION
C
        IF (NGPH .EQ. 0) GO TO 2
        IF (J .NE. 1) GO TO 61
        DO 62 L=1,NPTS
        XNOR(L)=STEPP*(L-1)-RESOOL
```

```
      XNC=XNCR(L)
   62 YNOR(L)=PROFIL(1.,0,XNO)
   61 CONTINUE
      IF (NRTS .LT. NSOL) GO TO 2
      W=W*W1D
      WRITE(6,111) J, NSOL, NRTS, C2, W
      ROOOT=RTS(NSOL)
      CHAR=CARR(NSOL,I,J)
      YTC=VLCTY(NSOL,I,J)
      WRITE(6,112) ROOOT, CHAR, YTC
      DO 63 L=1,NPTS
      XNO=XNCR(L)
   63 YCOM(L)=PROFIL(ROOOT,1,XNO)
      CALL ORIGIN (XGLAB,YGLAB,6)
      CALL ORIGIN (SYMHT,0.0,5)
      CALL GRAPH (NPTS,XNOR,YNOR,0,2,XSIZ,YSIZ,0.,0.,0.,0.,XLAB,YLAB,
     *GLAB,DATLAB)
      CALL GRAPHS (NPTS,XNOR,YCOM,1,101,DATLB)
    2 CONTINUE
    1 CONTINUE
C
C     STORAGE ROUTINE
C
      IF (NGTD) 68,65,68
   68 DO 66 N=8,9
      WRITE(N) NW,NC2,VMAX(N-7),VMIN(N-7)
      DO 67 I=1,NW
   67 WRITE(N) (VLCTY(N-7,I,J),J=1,NC2)
   66 CONTINUE
      WRITE(6,113)
      ICODE=1
      IF (NGTD) 65,65,99
   65 CONTINUE
C
C     CREATE VELOCITY SCHEME -- SORT,GROUP,LABEL
C
      MN=0
      LX=0
      KK=0
      LY=1
      NRES=1
      BVINT=0.
      NT1=NG(1)+NB(1)
      NT2=NG(2)+NB(2)
      NT=NT1+NT2
      IF(NT .NE. 0) GO TO 10
      WRITE(6,139)
      GO TO 99
   10 IF(NT2 .NE. 0 .AND. NOPTN .EQ. 1) GO TO 25
      IL=1
```

```
      JL=1
      IF(NOPTN .EQ. 0) GO TO 46
      WRITE(6,140)
      GO TO 46
   25 IL=1
      JL=2
      NFLAG=0
      IF(NG(1) .GT. 10 .AND. NG(2) .GT. 10) NFLAG=1
   46 CONTINUE
      DO 45 LL=IL,JL
      IG1C=IG1(LL)
      IF(NG(LL) .EQ. 0) GO TO 11
      IF(NG(LL) .LE. 10) GO TO 12
      IF(NFLAG .EQ. 1 .AND. NOPTN .EQ. 1) GO TO 26
      VLMX=VMAX(LL)
      VLMN=VMIN(LL)
      GO TO 48
   26 AAA=VMAX(1)
      BBB=VMAX(2)
      CCC=VMIN(1)
      DDD=VMIN(2)
      VLMX=AMAX1(AAA,BBB)
      VLMN=AMIN1(CCC,DDD)
   48 CONTINUE
      IF(NFLAG .EQ. 1 .AND. LL .EQ. 2) GO TO 47
      VINTVL=(VLMX-VLMN)/(10.*NRES)
      KK=LL
      BVINT=VINTVL
      IF(VINTVL .LT. VRSLV) GO TO 13
      NSYM=10
      GO TO 31
   13 NSYM=INT((VLMX-VLMN)*10.)+1
      VINTVL=VRSLV
   31 M=NSYM+1
      DO 14 I=1,M
      V(I)=VLMN+(I-1)*VINTVL+NSYM*VINTVL*LX
      VV=V(I)
   14 SSEP(I)=SEP(VV)
   47 CONTINUE
      L=0
      N=NSYM/2+1
      DO 15 I=IG1C,NW
      DO 16 J=1,NC2
      IF(IV(LL,I,J)) GO TO 16
      IF(V(N)-VLCTY(LL,I,J))  28,29,30
   28 K=N
      GO TO 17
   29 K=N+1
      GO TO 19
   30 K=1
```

```
      IF(V(K) .GT. VLCTY(LL,I,J)) GO TO 50
   17 K=K+1
      IF(K .EQ. NSYM+2) GO TO 50
      IF(V(K) .GT. VLCTY(LL,I,J)) GO TO 19
      IF(V(K) .EQ. VLCTY(LL,I,J) .AND. K .EQ. M) GO TO 18
      GO TO 17
   50 CARR(LL,I,J)=CERR(6)
      GO TO 51
   18 K=NSYM+1
   19 CARR(LL,I,J)=CV(K-1)
   51 CONTINUE
      L=L+1
      IF(L .GE. NG(LL)) GO TO 41
   16 CONTINUE
   15 CONTINUE
   41 MM=0
      GO TO 11
   12 N=0
      DO 32 I=IG1C,NW
      DO 33 J=1,NC2
      IF(IV(LL,I,J)) GO TO 33
      N=N+1
      VSAVE(N)=VLCTY(LL,I,J)
      ISAVE(N)=I
      JSAVE(N)=J
      IF(N .GE. NG(LL)) GO TO 34
   33 CONTINUE
   32 CONTINUE
   34 CONTINUE
      NGO=NG(LL)
      DO 35 L=1,NGO
      VMX=VSAVE(L)
      K=L
      DO 36 N=1,NGO
      IF(VSAVE(N) .LE. VMX) GO TO 36
      VMX=VSAVE(N)
      K=N
   36 CONTINUE
      VSAVE(K)=-1000.
      M=NG(LL)-L+1
      V(M)=VMX
      IORDR(M)=ISAVE(K)
   35 JORDR(M)=JSAVE(K)
      DO 20 I=1,NGO
      VV=V(I)
   20 SSEP(I)=SEP(VV)
      DO 37 M=1,NGO
      I=IORDR(M)
      J=JORDR(M)
   37 CARR(LL,I,J)=CV(M)
```

```
      NSYM=NG(LL)
      MM=1
   11 CONTINUE
C
C     GRAPH RESULTS
C
      IF(LL .EQ. 1) GO TO 56
      WRITE(6,110) NRES,LY,NRES
      GO TO 57
   56 WRITE(6,120) NRES,LY,NRES
   57 CONTINUE
      DO 21 I=1,NW
      W=W1+(NW-I)*WSTP
      IF(I .EQ. NW/2) GO TO 22
      IF(I .EQ. NW/2+1) GO TO 23
      WRITE(6,121) W, (CARR(LL,I,J),J=1,NC2)
      GO TO 21
   22 WRITE(6,122) W, (CARR(LL,I,J),J=1,NC2)
      GO TO 21
   23 WRITE(6,123) W, (CARR(LL,I,J),J=1,NC2)
   21 CONTINUE
      N=INT(C21)
      DO 49 K=1,10
   49 IHTLAB(K)=N+(K-1)*10
      WRITE(6,124) (IHTLAB(K),K=1,10)
C
C     DISPLAY VELOCITY AND SEPARATION KEY
C
   27 IF(NG(LL) .EQ. 0) GO TO 45
      IF(NFLAG .EQ. 1 .AND. LL .EQ. 2) GO TO 45
      IF(MM .EQ. 1) GO TO 38
      WRITE(6,102)
      DO 39 K=1,NSYM
      L=K+1
   39 WRITE(6,103) V(K),SSEP(K),CV(K),SSEP(L),V(L)
      GO TO 45
   38 CONTINUE
      WRITE(6,104)
      DO 40 K=1,NSYM
   40 WRITE(6,105) CV(K), V(K),SSEP(K)
   45 CONTINUE
C
C     DISPLAY REJECT KEY
C
      IF(MN .EQ. 1) GO TO 52
      IF(NB(1)+NB(2) .EQ. 0) GO TO 44
      WRITE(6,114)
      WRITE(6,115) CERR(1),CR
      WRITE(6,116) CERR(2),FIR
```

```
      WRITE(6,117) CERR(3)
      WRITE(6,118) CERR(4),WR
      WRITE(6,119) CERR(5),ARR
   44 CONTINUE
C
C     DISPLAY TYPICAL KEPLER DISK VELOCITIES
C
      IF(NG(1)+NG(2) .EQ. 0) GO TO 99
      WRITE(6,106)
      DO 43 N=1,8
      ALFA=1./N
      DO 59 M=1,3
      THETA=(M-1)*30.
      THITA=THETA*3.1416/180.
      RIMV=SQRT(6.668*1.989*10**5*MX/(ALFA*RMN2*6.960))*COS(THITA)
   59 WRITE(6,107) ALFA,THETA,RIMV
   43 CONTINUE
      IF(NRESL .EQ. 1) GO TO 99
C
C     INCREASE RESOLUTION
C
      MN=1
      IF(NOPTN .EQ. 0 .AND. NG(1) .LE. 10) GO TO 99
      IF(NG(1) .LE. 10 .AND. NG(2) .LE. 10) GO TO 99
      IF(BVINT .LT. 2.*VRSLV) GO TO 99
      NUM=INT(BVINT/VRSLV)
      NRES=MIN0(NRESL,NUM)
      LX=-1
      LY=0
      IF (NFLAG .EQ. 0 .OR. NOPTN .EQ. 0) GO TO 53
      IL=1
      JL=2
      GO TO 52
   53 IL=KK
      JL=KK
   52 CONTINUE
      IF(LY .EQ. NRES) GO TO 99
      DO 54 LT=IL,JL
      DO 54 I=1,NW
      DO 54 J=1,NC2
   54 CARR(LT,I,J)=CERR(6)
      LX=LX+1
      LY=LX+1
      GO TO 46
   99 IF (ICODE .EQ. 1 .AND. NTD .EQ. 1) STOP 100
      STOP
  100 FORMAT(  ' LINE WITH C2=',F4.0,' AND W= ',F4.2,' HAS A ROOT AT S=
     *',F6.4,' CORRESPONDING TO A SPEED OF ',F6.1,' KM/S')
  101 FORMAT(  ' LINE WITH C2=',F4.0,' AND W= ',F4.2,' HAS A ROOT AT S=
     *',F6.4,5X,A1)
```

```
102 FORMAT(T17,'VELOCITY AND SEPARATION KEY',/,T6,49('-'),/,T6,
   *'V(KPS)',T15,'S(W1D)',T28,'SYMBOL',T40,'S(W1D)',T49,'V(KPS)',/)
103 FORMAT(T6,F6.1,3X,F6.4,9X,A1,9X,F6.4,3X,F6.1)
104 FORMAT(T6,'VELOCITY AND SEPARATION KEY',/,T6,27('-'),/,T7,
   *'SYMBOL',T15,'V(KPS)',T25,'S(W1D)',/)
105 FORMAT(T9,A1,5X,F6.1,4X,F6.4)
106 FORMAT(/,T11,'TYPICAL KEPLER DISK VELOCITIES',/,T6,40('-'),/,T6,
   *'RADIUS(RMN2)',4X,'THETA(DEG)',4X,'SPEED(KPS)',/)
107 FORMAT(T9,F5.3,T24,F5.1,T38,F6.1)
109 FORMAT('1THIS IS SEARCH ',I3,' FOR THE FOLLOWING MODEL:',/)
110 FORMAT('1THESE ARE SECONDARY SOLUTIONS. RESOLUTION IS ',I1,
   *'. THIS IS GRAPH # ',I1,' OF ',I1,'.')
111 FORMAT(/,' LINE DISPLAY GRAPH # ',I2,/,' THIS IS SOLUTION ',I1,
   *' OF ',I1,' FOR EMISSION LINE C2=',F5.1,' AND W=',F5.2,'ANGSTROMS
   *')
112 FORMAT(' SEPARATION IS ',F6.4,/,' REJECTION SYMBOL IS ',A1,/,
   *' VELOCITY IS ',F6.1)
113 FORMAT(//' INFORMATION PASSED TO 3-D',//)
114 FORMAT('1',T26,'REJECT KEY',/,T6,51('-'),/)
115 FORMAT(T7,A1,' -- CONTINUUM INCREASED MORE THAN ',2PF5.1,' %')
116 FORMAT(T7,A1,' -- LINE DEPTH FILLED IN MORE THAN ',2PF5.1,' %')
117 FORMAT(T7,A1,' -- EMISSION LINE IS RESOLVED')
118 FORMAT(T7,A1,' -- LINE WIDTH FILLED IN MORE THAN ',2PF5.1,' %')
119 FORMAT(T7,A1,' -- EQUIVALENT WIDTH DECREASED MORE THAN ',2PF5.1,
   *' %')
120 FORMAT('1THESE ARE PRIMARY SOLUTIONS. RESOLUTION IS ',I1,
   *'. THIS IS GRAPH # ',I1,' OF ',I1,'.')
121 FORMAT(T13,F5.2,3X,91A1)
122 FORMAT('  HALF-WIDTH',T13,F5.2,3X,91A1)
123 FORMAT('     (ANG)',T13,F5.2,3X,91A1)
124 FORMAT(T21,10('|',9X),/,T20,10(I3,7X),/,T60,'HEIGHT')
125 FORMAT('   MP=',F4.1,'   MX=',F4.1,'   DEGI=',F4.1,'   AU=',F4.1,
   *'   RMN=',F4.1,'   RMN2=',F4.1)
126 FORMAT('   VR=',F6.1,'   KAYONE=',F6.1,'   KAYTWO=',F6.1,
   *'   VSINI=',F6.1,'   VREQ=',F6.1)
127 FORMAT(/,' THE LINE IS H-BETA WITH:',/,'   LMO=',F8.3,'   W1=',
   *F4.1,'   C1=',F4.2,'   H=',F6.4)
128 FORMAT(/,' THE LINE BROADENING EFFICIENCY IS ',F3.1)
129 FORMAT(/,' THE REFERENCE LINE HAS:',/,'   LM1=',F8.3,'   W1D=',
   *F4.1,'   XMN=',F5.3,'   ERR=',E9.3)
130 FORMAT(/,' STEPPING CONDITIONS ARE:',/,'   C2I=',F4.1,'   C2STP=',
   *F5.2,'   NC2=',I3,'   WI=',F4.2,'   WSTP=',F4.2,'   NW=',I3)
131 FORMAT(/,' PROFILE TEST USES:',/,'   CR=',F5.3,'   FIR=',F4.2,
   *'   RSR1=',F5.3,'   RSR2=',F5.3,'   RSR3=',F5.3,'   WR=',F4.2,
   *'   ARR=',F4.2)
132 FORMAT(6F9.2)
133 FORMAT(6F5.1)
134 FORMAT(F10.3,F5.1,F5.2,F5.4)
135 FORMAT(2(2F5.2,I3))
136 FORMAT(7F5.3)
```

```
  137 FORMAT(I3)
  138 FORMAT(/,' XMN IS NOT LESS THAN 2.0')
  139 FORMAT(/,' NO SOLUTIONS EXIST FOR THIS PRIMARY LINE')
  140 FORMAT(/,' NO SECONDARY SOLUTIONS EXIST')
  141 FORMAT(10A1)
  142 FORMAT(5A4)
  143 FORMAT(3F5.2)
  144 FORMAT(F3.1,2X,I3)
  145 FORMAT(2F5.2,I1,5A4)
  146 FORMAT(/,' DELREQ=',F5.1,5X,'DELONE=',F5.1,/,
     *' VBOT=',F6.1,5X,'VTOP=',F6.1)
      END
C
C     SUBROUTINE SEARCH
C          SEARCH FINDS THE NUMBER OF ROOTS (NRTS) OF THE SEPARATION
C          FUNCTION AND REPORTS AS MANY AS TWO OF THEM, RT1&RT2
C
      SUBROUTINE SEARCH(NRTS,RT1,RT2)
      COMMON D1,D2,D3,D4,D5,D6,D7/ODD/ER
      EXTERNAL FFS, FPS1
      NRTS=0
      BB=2.*D4+ER
      F=FS(0.)
      FP=FPS(0.)
      IF(FP .LT. 1.) GO TO 1
      IF(F) 2,99,99
    2 NRTSL=1
      CALL DETECT(NRTSL,FFS,NRTS,RT1,RT2,0.,BB,D4,ER,-1)
      IF(NRTS .NE. NRTSL) WRITE(6,109) D3,D4,NRTS,NRTSL
      GO TO 99
    1 IF(F) 2,2,3
    3 CALL DETECT(1,FPS1,KRTS,S0,S1,0.,BB,D4,ER,1)
      IF(KRTS .EQ. 0) GO TO 6
      F0=FS(S0)
      IF(F0-S0) 4,5,99
    4 IF(S0 .LE. ER) GO TO 7
      NRTSL=2
      CALL DETECT(NRTSL,FFS,NRTS,RT1,RT2,0.,BB,S0,ER,1)
      IF(NRTS .NE. NRTSL) WRITE(6,109) D3,D4,NRTS,NRTSL
      GO TO 99
    6 WRITE(6,110) D3,D4
      GO TO 99
    7 NRTSL=1
      CALL DETECT(NRTSL,FFS,NRTS,RT1,RT2,S0,BB,S0,ER,-1)
      IF(NRTS .EQ. 0) GO TO 8
      NRTS=2
      RT2=S0
      GO TO 99
    8 NRTS=1
      RT1=S0
```

```
      WRITE(6,113) D3,D4
      GO TO 99
    5 NRTS=1
      RT1=S0
   99 RETURN
  109 FORMAT(  ' IN SEARCH, EXPECTED # ROOTS NOT FOUND-- C2= ',F4.0,3X,
     *' W= ',F4.2,3X,' NRTS= ',I1,3X,' NRTSL= ',I1)
  110 FORMAT(  ' IN SEARCH, KRTS WAS NOT FOUND-- C2= ',F4.0,3X,' W= ',
     *F4.2)
  113 FORMAT(  ' IN SEARCH, RT2 FAILED-- C2= ',F4.0,3X,' W= ',F4.2)
      END
C
C     SUBOUTINE DETECT
C          NRT ROOTS ARE SOUGHT IN THE FUNCTION FX BETWEEN POINTS A AND E
C          INITIAL STEP LENGTH IS STEP AND FINAL RESOLUTION IS ER
C          MRTS ROOTS ARE FOUND AND TWO OF THEM, R1&R2, ARE REPORTED
C          INDX (-1,0,1) IS OPTIONAL(0) SIGN OF FIRST DISCREPANCY
C
      SUBROUTINE DETECT(NRT,FX,MRTS,R1,R2,A,E,STEP,ER,INDX)
      DIMENSION RT(2)
      NF=0
      MRTS=0
      B=E
      C=ABS((B-A)/2.)
      D=STEP
      STET=STEP
      N=2
      IF(A .GT. B) N=1
      STET=(-1)**N*D
      IF(NRT .EQ. 2 .AND. D .GT. C) B=2.*STET+ER*(-1)**N+A
      NINDX=INDX
      Z1=A
      IF(NINDX) 1,2,3
    1 ISF1=-1
      GO TO 4
    3 ISF1=1
      GO TO 4
    2 FZ1=FX(Z1)
      ISF1=INT(SIGN(1.,FZ1))
    4 CONTINUE
      Z2=Z1+STET
      IF(N .EQ. 2) GO TO 10
      IF(Z2 .LT. B) NF=NF+1
      GO TO 11
   10 IF(Z2 .GT. B) NF=NF+1
   11 CONTINUE
      IF(NF .EQ. 2) GO TO 99
      FZ2=FX(Z2)
      IF(FZ2 .EQ. 0.) GO TO 98
      ISF2=INT(SIGN(1.,FZ2))
```

```
      IF(ISF1 .NE. ISF2)  GO TO 5
      IF(NF .EQ. 1) GO TO 99
      Z1=Z2
      GO TO 4
    5 STP=STET/2.
    7 CONTINUE
      Z1=Z2-STP
      FZ1=FX(Z1)
      IF(FZ1 .EQ. 0.) GO TO 97
      ISF1=INT(SIGN(1.,FZ1))
      IF(ISF1 .NE. ISF2) GO TO 6
      Z2=Z1
    6 IF(ABS(STP) .LE. ER) GO TO 98
      STP=STP/2.
      GO TO 7
   97 Z2=Z1
   98 MRTS=MRTS+1
      RT(MRTS)=Z2
      IF(MRTS .EQ. NRT) GO TO 99
      Z1=Z2+STP
      FZ1=FX(Z1)
      IF(FZ1 .EQ. 0.) GO TO 97
      ISF1=INT(SIGN(1.,FZ1))
      IF(ISF1 .NE. ISF2) GO TO 97
      GO TO 4
   99 IF(MRTS-1) 100,8,9
    8 R1=RT(1)
      GO TO 100
    9 R1=RT(2)
      R2=RT(1)
  100 RETURN
      END
C
C     SUBROUTINE PROTST
C          RL IDENTIFIES A PROFILE WHOSE PROPERTIES ARE TESTED AND
C          REPORTED BY INDX
C          RL = SEPARATION
C
C                INDX      ERROR
C                  1     CONTINUUM
C                  2     FILLED IN
C                  3     RESOLVED
C                  4     NARROW
C                  5     EW CHANGE
C                  6        NONE
C
      SUBROUTINE PROTST(RL,INDX)
      COMMON F1,F2,F3,F4,F5,F6,F7/PROPAS/Y,RT
      COMMON/SCREEN/C,F,RS1,RS2,RS3,WW,AR
      EXTERNAL PROATI
```

```
      RT=RL
      ZCUR=0.
      NTAG=0
      EMLIM=-RT-2.*F4
      ABLIM=-2.
      ALNLM=AMIN1(EMLIM,ABLIM)
      ZTEP=-ALNLM/4.
      RN=-2.
      GO TO 16
   17 NTAG=NTAG+1
      IF (NTAG .GE. 6) GO TO 1
      RN=-RT-(NTAG-1)*ZTEP
   16 Z=PROFIL(RT,1,RN)
      IF (Z .LE. ZCUR) GO TO 1
      IF (NTAG .GT. 0) ZCUR=Z
      IF (Z .LE. 1.+F1+C) GO TO 17
      INDX=1
      GO TO 99
    1 ALFA=1.-(1.+F1-PROFIL(RT,1,F6))/F2
      IF(ABS(ALFA) .LE. F) GO TO 2
      INDX=2
      GO TO 99
    2 TSTPNT=-RT-2.*F4
      RS=RS2
      IF(PROSLP(RT,TSTPNT) .LT. RS3) RS=RS1
      DO 14 K=1,3
      PNT=-RT+F4*((K-1)*.5-1.5)
      IF(PROSLP(RT,PNT) .GT. RS) GO TO 15
   14 CONTINUE
      GO TO 3
   15 INDX=3
      GO TO 99
    3 Y=1.-(1.-ALFA)*F2/2.+F1
      S=2.-F6
      CALL DETECT(1,PROATI,NRS,RL1,RL2,2.,F6,S,.01,1)
      IF(NRS .EQ. 1) GO TO 4
      WRITE(6,111) F3,F4
      INDX=4
      GO TO 99
    4 X1=RL1
      IF(RT .GE. 2.) GO TO 5
      Z=PROFIL(RT,1,-RT)
      IF(Z-Y) 6,7,8
    7 X2=-RT
      GO TO 11
    6 A=-2.
      S=2.-RT
      IF(S .LT. .01) GO TO 7
      B=-RT
      GO TO 9
```

```
    8 A=-RT
      S=F4
      B=F6
      GO TO 9
    5 A=-2.
      S=1.
      B=F6
    9 CALL DETECT(1,PROATI,NRS,RL1,RL2,A,B,S,.01,1)
      IF(NRS .EQ. 1) GO TO 10
      WRITE(6,112) F3,F4
      INDX=4
      GO TO 99
   10 X2=RL1
   11 CONTINUE
      IF (ABS(X1-X2) .GE. .01) GO TO 18
      WRITE(6,113) F3,F4
      INDEX=4
      GO TO 99
   18 CONTINUE
      BETA=1.-(X1-X2)/2.
      IF(ABS(BETA) .LE. WW) GO TO 12
      INDX=4
      GO TO 99
   12 IF(ALFA+BETA-ALFA*BETA .LE. AR) GO TO 13
      INDX=5
      GO TO 99
   13 INDX=6
   99 RETURN
  111 FORMAT(  ' IN PROTST, NARROW-TEST FAILED TO FIND X1-- C2= ',F4.0,
     *3X,' W= ',F4.2)
  112 FORMAT(  ' IN PROTST, NARROW-TEST FAILED TO FIND X2-- C2= ',F4.0,
     *3X,' W= ',F4.2)
  113 FORMAT( ' IN PROTST, X1=X2 IN NARROW-TEST: C2=',F4.0,'    W=',F4.2)
      END
C
C     THE FOLLOWING FUNCTIONS ARE RELATED TO GAUSSIAN OR BLEND
C     PROFILES OR PROFILE SLOPES
C
C
C     FUNCTION FS
C
      FUNCTION FS(T)
      COMMON F1,F2,F3,F4,F5,F6,F7
      ARG2=F5*T*(2.*F6+T)/(F4*F4)
      ARG=F7+ARG2
      IF(ABS(ARG) .LT. 161.) GO TO 1
      IF(ARG) 3,3,2
    2 FS=1000.
      GO TO 4
    3 ARG=0.
```

```
    1 BE=F4*F4*F2/(F1*F3)
      FS=F6*(BE*EXP(ARG)-1.)
    4 RETURN
      END
C
C     FUNCTION FPS
C
      FUNCTION FPS(T)
      COMMON F1,F2,F3,F4,F5,F6,F7
      ARG2=F5*T*(2.*F6+T)/(F4*F4)
      ARG=F7+ARG2
      IF(ABS(ARG) .LT. 161.) GO TO 1
      IF(ARG) 3,3,2
    2 FPS=1000.
      GO TO 4
    3 ARG=0.
    1 BE=2.*F5*F6*F2/(F1*F3)
      FPS=BE*EXP(ARG)*(F6+T)
    4 RETURN
      END
C
C     FUNCTION FPS1
C
      FUNCTION FPS1(T)
      COMMON F1,F2,F3,F4,F5,F6,F7
      ARG2=F5*T*(2.*F6+T)/(F4*F4)
      ARG=F7+ARG2
      IF(ABS(ARG) .LT. 161.) GO TO 1
      IF(ARG) 2,3,3
    2 FPS1=1000.
      GO TO 4
    3 ARG=0.
    1 BE=F1*F3/(2.*F6*F2*F5)
      FPS1=BE/EXP(ARG)-F6-T
    4 RETURN
      END
C
C     FUNCTION PROFIL
C          INDX SPECIFIES REFERENCE (0) OR BLEND (1)
C
      FUNCTION PROFIL(R,INDX,PT)
      COMMON F1,F2,F3,F4,F5,F6,F7
      ARG1=F5*PT*PT
      A=1.-F2/EXP(ARG1)
      IF(INDX .EQ. 1) GO TO 1
      PROFIL=A
      GO TO 99
    1 ARG2=F5*((PT+R)/F4)**2
      B=F1
      IF(ARG2 .LT. 170.) B=F1*(1.+F3/EXP(ARG2))
```

```
      PROFIL=A+B
   99 RETURN
      END
C
C     FUNCTION FFS
C
      FUNCTION FFS(T)
      FFS=FS(T)-T
      RETURN
      END
C
C     FUNCTION PROATI
C
      FUNCTION PROATI(T)
      COMMON/PROPAS/YY,RR
      PROATI=PROFIL(RR,1,T)-YY
      RETURN
      END
C
C     FUNCTION PROSLP
C
      FUNCTION PROSLP(R,PT)
      COMMON F1,F2,F3,F4,F5,F6,F7
      ARG1=F5*PT*PT
      A=F2*PT/EXP(ARG1)
      ARG2=F5*((PT+R)/F4)**2
      B=0.
      IF(ARG2 .LT. 170.) B=F1*F3*(PT+R)/(F4*F4*EXP(ARG2))
      PROSLP=2.*F5*(A-B)
      RETURN
      END
C
C     FUNCTION VEL
C
      FUNCTION VEL(R)
      COMMON/SPEED/F1,F2,F3,F4,F5,F6,F7
      VEL=((F2-R*F1-F4)*F3/F4-F5-F7)/F6
      RETURN
      END
C
C     FUNCTION SEP
C
      FUNCTION SEP(V)
      COMMON/SPEED/F1,F2,F3,F4,F5,F6,F7
      SEP=(F2-F4*(F6*V+F5+F7)/F3-F4)/F1
      RETURN
      END
```

```
C
C
C      PROGRAM CODE: TRIPLT
C           THIS PROGRAM PLOTS THE 3-D REPRESENTATION OF EMISSION
C           LINES FOUND BY BLNDER
C           ONLY GRAPH LABELS ST* AND BOOKKEEPER NSCH NEED BE
C           SPECIFIED. OTHER PARMS ARE PASSED FROM BLNDER
C           TRIPLT IS STEP TWO OF BLNDER EXECUTION
C
      DIMENSION DATE(7), PARM(11), A(100,91)
      DIMENSION VMAX(2), VMIN(2)
      DIMENSION ST1(4), ST2(3), ST3(4), ST4(4)
      COMMON ANGA,ANGB,HV,DUMMY(14)
      PI=3.141593
      HV=10.
      BDEG=60.0
      ANGB=BDEG*PI/180.0
      ADEG=-20.0
      ANGA=ADEG*PI/180.0
      READ(5,103) ST1
      READ(5,103) ST2
      READ(5,103) ST3
      READ(5,103) ST4
      READ(5,104) NSCH
      CALL LABEL(DATE,PARM,NPARM)
      I=1
      WRITE(6,100) I, NSCH, ADEG, BDEG
      WRITE(6,101) DATE,PARM
      DO 1 N=8,9
      M=N-7
      READ(N) NW,NC2,VMAX(M), VMIN(M)
      DO 2 I=1,NW
    2 READ(N) (A(NW+1-I,J),J=1,NC2)
      WRITE(6,102) M, VMAX(M), VMIN(M)
      CALL SYMBOL(0.0,2.3,.15,ST1,-66.2,16)
      CALL SYMBOL(4.7,0.7,.15,ST2,17.6,12)
      CALL SYMBOL(5.0,9.0,.15,ST3,00.0,16)
      CALL SYMBOL(3.4,9.5,.20,ST4,00.0,16)
    1 CALL THREED(A,NW,NC2,3)
      CALL ENDPLT
      STOP
  100 FORMAT(//,' THIS IS SEARCHPLOT ',I2,' FROM SEARCH ',I3,/,
     *'  ADEG= ',F5.1,' AND BDEG= ',F5.1)
  101 FORMAT(' ****',7A4,5X,10A4)
  102 FORMAT(/,' FOR SOLUTION #',I2,' VMAX IS ',F6.1,' AND VMIN IS ',
     *F6.1)
  103 FORMAT(4A4)
  104 FORMAT(I3)
      END
```

```
C
C
C      PROGRAM CODE: POPGEN
C
C           THIS PROGRAM SOLVES THE STATISTICAL EQUILIBRIUM EQUATIONS
C           FOR NN BOUND HYDROGEN STATES AND THE CONTINUUM. IT ALSO
C           CALCULATES OPACITY AND EMISSIVITY AND ESTIMATES EMISSION
C           LINE SHAPES
C            INPUT:  KL - MATRIX ACCURACY REQMNT (SIGNIF FGRS)
C                    NN - QUANTUM # OF HIGHEST BOUND STATE
C                    FRAT - RELATIVE SECONDARY CONTINUUM STRENGTH
C                    AT THE LINE
C                    BOL - PRIMARY FLUX AT THE LINE
C                    (ERGS/SEC-CM**2-ANG)
C                    A(I,J) - TRANSITION LIFETIMES
C                    MM - # OF MODELS PER RUN
C                    T1,T2 - PRIMARY,SECONDARY EFF TEMPS (DEG-K)
C                    S - LINE OF SIGHT DIMENSION (CM)
C                    NH,NE - DENSITIES (CM**-3)
C                    TE - GAS ELECTRON TEMPERATURE (DEG-K)
C                    W1,W2 - DILUTION FACTORS
C                    PRT - DISTANCE FROM OPACITY PROFILE CENTER
C                     (HALF WIDTHS) FOR ESTIM OF W
C           OUTPUT:  C,R,P,D - RATE AND STAT EQUILIB MATRICES
C                    LEVEL POPULATIONS
C                    KES,KFF,KBF,KC - PARTIAL & TOTAL CONTIN OPACITIES
C                       (CM**-1)
C                    JFF,JFB,JC - EMISSIVITIES (ERG/S-CM**3-STR-ANG)
C                    KL,JL - LINE COEFS (ANG/CM),(ERG/S-CM**3-STR)
C                    FAC - FF/TOTAL CONTIN
C                    VOL - VOLUME REQUIRED BY F (CM**3)
C                    JFFT - TOTAL FF (ERG/S)
C                    CLOUD MASS
C                    THERMAL WIDTH (ANG)
C                    3 PROFILE HEIGHT ESTIMATES,THERM PROFILE EW
C                    OPTICAL DEPTHS FOR THERM AND 1 ANG LINES
C
C
      IMPLICIT REAL*8 (A-H,O-Z)
      REAL*8 NH,NE,MMDEI
      DIMENSION A(5,5),C(6,6),R(6,6),P(6,6),D(6,6),B(6),WKA(60)
      COMMON TT/H/RKC,RKL,RJC,RJL,S,RLP,TAUCM
      EXTERNAL E1,E2
      READ(5,101) KL
      READ(5,101) NN
      READ(5,100) FRAT,BOL
      READ(5,100) PRT
      PSR=DEXP(-DLOG(2.D0)*PRT*PRT)
```

```
      AA=-15.9826D4
      BB=.18750D0
      PI=3.14159D0
      RLP=DSQRT(DLOG(2.D0)/PI)
      L=0
      DO 11 N=1,NN
   11 L=L+NN-N
      READ(5,102) ((I,J,A(I,J)),K=1,L)
      WRITE(6,114)
      KK=NN-1
      DO 13 I=1,KK
      LL=I+1
      DO 12 J=LL,NN
   12 WRITE(6,115) I,J,A(I,J)
   13 CONTINUE
      READ(5,101) MM
      READ(5,100) T1,T2,S
      WRITE(6,118)
      WRITE(6,104) T1,T2,S,BOL,FRAT
      DO 15 KKK=1,MM
      READ(5,100) NH,NE,TE
      READ(5,100) W1,W2
      WRITE(6,116)
      WRITE(6,117)
      WRITE(6,104) NH,NE,TE,W1,W2
      SQT=DSQRT(TE)
      Z=8.625D-5*TE
      G=TE/T1
      H=TE/T2
      M=NN+1
      DO 1 I=1,M
      DO 2 J=I,M
      IF(I .NE. J) GO TO 3
      C(I,J)=0.D0
      R(I,J)=0.D0
      P(I,J)=0.D0
      GO TO 2
C
C     CALCULATE BOUND-BOUND RATES
C
    3 IF(J .EQ. M) GO TO 4
      X=13.6D0*(1./(I*I)-1./(J*J))/Z
      C(I,J)=13.4540D0*A(I,J)*J*J*NE/(X**3.68D0*DEXP(X)*TE**3.5D0)
      C(J,I)=C(I,J)*I*I*DEXP(X)/(J*J)
      R(I,J)=A(I,J)*J*J/(I*I)*(W1/(DEXP(G*X)-1.)+W2/(DEXP(H*X)-1.))
      R(J,I)=A(I,J)+R(I,J)*I*I/(J*J)
      P(I,J)=C(I,J)+R(I,J)
      P(J,I)=C(J,I)+R(J,I)
      GO TO 2
```

```
C
C       CALCULATE BOUND-FREE RATES
C
    4   X=13.6D0/(I*I*Z)
        C(I,J)=1.23D-5*NE*I/(SQT*DEXP(X)*X)
        C(J,I)=5.04D-21*I*I*I*NE*NE/(TE*TE*X)
        TT=G
        S1=SIMP(E1,X,1.D3,1.D-9,1000,.05D0)
        S3=SIMP(E2,X,1.D3,1.D-9,1000,.05D0)
        TT=H
        S2=SIMP(E1,X,1.D3,1.D-8,1000,.10D0)
        S4=SIMP(E2,X,1.D3,1.D-9,1000,.05D0)
        R(I,J)=7.84700D9/(I**5)*(W1*S1+W2*S2)
        R(J,I)=3.2579D-6*NE*DEXP(X)*(MMDEI(2,X,IE)+W1*S3+W2*S4)/(TE*I**3*
       *SQT)
        P(I,J)=C(I,J)+R(I,J)
        P(J,I)=C(J,I)+R(J,I)
    2   CONTINUE
    1   CONTINUE
C
C       FORM STAT EQUILIB MATRIX
C
        DO 5 I=1,M
    5   D(1,I)=1.
        DO 6 I=2,M
        K=I-1
        DO 7 J=1,M
    7   D(I,J)=P(J,K)
    6   CONTINUE
        DO 8 I=2,M
        J=I-1
        Y=0.D0
        DO 9 K=1,M
    9   Y=Y+P(J,K)
    8   D(I,J)=D(I,J)-Y
        DO 10 I=2,M
   10   B(I)=0.D0
        B(1)=NH
        WRITE(6,103)
        WRITE(6,104) ((C(I,J),J=1,M),I=1,M)
        WRITE(6,105)
        WRITE(6,104) ((R(I,J),J=1,M),I=1,M)
        WRITE(6,106)
        WRITE(6,104) ((P(I,J),J=1,M),I=1,M)
        WRITE(6,107)
        WRITE(6,104) ((D(I,J),J=1,M),I=1,M)
C
C       DIAGONALIZE FOR POPULATIONS
C
        CALL LEQT2F(D,1,M,M,B,KL,WKA,IER)
```

```
      WRITE(6,108) (I,I=1,M)
      WRITE(6,104) (B(I),I=1,M)
C
C     CALCULATE OPACITIES, EMISSIVITIES
C
      TM=2.96D4/TE
      CC=0.D0
      DO 14 I=3,10
      DD=I*I*1.D0
      EE=DD*I
      FF=AA/TE
   14 CC=CC+DEXP(FF*(BB-1.D0/DD))/EE
      RJFB=2.158D-22*NE*NE*CC/(TE*SQT)
      RKES=6.65D-25*NE
      RKBF=1.45D-17*B(2)
      RKFF=1.57D-36*NE*NE*(1.D0-DEXP(-TM))/SQT
      RKC=RKFF+RKBF+RKES
      RJFF=6.9067D-28*NE*NE/(DEXP(TM)*SQT)
      RJL=3.26D-13*A(2,4)*B(4)
      RKL=7.4053D-22*B(2)*A(2,4)*(4.D0-B(4)/B(2))
      RJC=RJFF+RJFB
      RJCT=FRAT*BOL
      V=RJCT/(12.57D0*RJC)
      FAC=RJFF/RJC
      RJFFT=1.435D-27*NE*NE*SQT*V
      GASMAS=NE*V*8.37D-57
      WRITE(6,109)
      WRITE(6,104) RKES,RKFF,RKBF,RKC,RKL,RJL
      WRITE(6,110)
      WRITE(6,104) RJFF,RJFB,RJC,FAC,V,RJFFT
      WRITE(6,111) GASMAS
C
C     CALCULATE PROFILE HEIGHT ESTIMATES
C
      DELLAM=2.08D-3*SQT
      Z1=HT(DELLAM,1.D0)
      TAU1=TAUCM
      Z2=HT(DELLAM,PSR)
      Z3=HT(1.D0,1.D0)
      TAU2=TAUCM
      Z4=HT(1.D0,PSR)
      Z5=HT(4.D0,1.D0)
      Z6=HT(4.D0,PSR)
      EW=Z1*DELLAM*FRAT/RLP
      WRITE(6,112)
      WRITE(6,113) DELLAM,Z1,Z2,Z3,Z4,Z5,Z6
      WRITE(6,119) EW
   15 WRITE(6,120) TAU1,TAU2
      STOP
  100 FORMAT(8D10.2)
```

```
  101 FORMAT(I3)
  102 FORMAT(5(2I3,D10.3))
  103 FORMAT(' ',5X,'C(I,J) = ')
  104 FORMAT((' ',11X,6(1PD10.3,2X)))
  105 FORMAT(' ',/ ,' ',5X,'R(I,J) = ')
  106 FORMAT(' ',/ ,' ',5X,'P(I,J) = ')
  107 FORMAT(' ',/ ,' ',5X,'D(I,J) = ')
  108 FORMAT(' ',/ ,' ',9X,6(2X,'POPLEVEL ',I1))
  109 FORMAT('0',14X,'KES,  KFF,  KBF,  KC,  KL,  JL  ARE:',/)
  110 FORMAT('0',14X,'JFF,  JFB,  JC,  FAC,  VOL,  JFFT  ARE:',/)
  111 FORMAT(' ',/ ,' CLOUD MASS IS ',1PD8.2,' SOLAR MASSES')
  112 FORMAT('0',14X,'THERMAL WIDTH(ANG), HEIGHTS(THERM,HALF,1ANG,HALF,4
     *ANG,HALF) ARE:',/)
  113 FORMAT((' ',11X,7(1PD10.3,2X)))
  114 FORMAT('1THE BOUND TRANSITIONS CONSIDERED AND THEIR A(I,J)S ARE:')
  115 FORMAT(' ',2I3,4X,1PD10.3)
  116 FORMAT('1MODEL PARAMETERS ARE:')
  117 FORMAT(' ',15X,'NH',10X,'NE',10X,'TE',10X,'W1',10X,'W2')
  118 FORMAT('0',14X,'T1,  T2,  S,  BOL,  F  ARE:',/)
  119 FORMAT('0',14X,'EQUIVALENT WIDTH OF A THERMAL LINE WOULD BE ',
     *1PD10.3,' ANGSTROMS IN THE PRIMARY CONTINUUM')
  120 FORMAT('0',14X,'LINE CENTER OPTICAL DEPTHS FOR THERMAL AND ONE ANG
     *STROM LINES ARE:',2(5X,1PD10.3))
      END
C
C     SIMPSON INTEGRATOR
C         INTEGRATES FUNCTION FX FROM X0 TO Y0 (STEPSIZE STP) WITH
C         TOLERANCE TOL IN THE SUM. MXIT LIMITS STEP NUMBER
C
      REAL FUNCTION SIMP*8(FX,X0,Y0,TOL,MXIT,STP)
      IMPLICIT REAL*8 (A-H,O-Z)
      N=0
      SUM=0.D0
      SSUM=0.D0
    6 X=X0+N*STP
      IF(X .EQ. X0 .OR. X .EQ. Y0) GO TO 1
      IF(N/2*2 .EQ. N) GO TO 2
      T=4.D0
      GO TO 3
    1 T=1.D0
      GO TO 3
    2 T=2.D0
    3 F=T*FX(X)
      SUM=SUM+F
      IF(X .EQ. Y0 .OR. F .LT. TOL) GO TO 4
      IF(N .LE. MXIT) GO TO 5
      A=X+50*STP
      B=A+50*STP
      C=B+50*STP
      D=C+50*STP
```

```
      SSUM=50*STP*(F/T+4.D0*FX(A)+2.D0*FX(B)+4.D0*FX(C)+FX(D))/3.D0
     *-(F-F/T)*STP/3.D0
      GO TO 4
    5 N=N+1
      GO TO 6
    4 SIMP=STP*SUM/3.D0+SSUM
      IF(SIMP .NE. 0.D0) GO TO 7
      SIMP=STP*TOL
    7 RETURN
      END
C
C     RADIATION INTEGRAL INTEGRANDS
C
      REAL FUNCTION E1*8(X)
      IMPLICIT REAL*8 (A-H,O-Z)
      COMMON T
      E1=1./(X*(DEXP(T*X)-1.))
      RETURN
      END
      REAL FUNCTION E2*8(X)
      IMPLICIT REAL*8 (A-H,O-Z)
      COMMON T
      E2=1./(X*DEXP(X)*(DEXP(T*X)-1.))
      RETURN
      END
C
C     LINE HEIGHT ESTIMATOR
C          DELLAM = HWHM OF OPACITY PROFILE
C          FRAC = DISTANCE FROM LINE CENTER (NORMALIZED)
C
      REAL FUNCTION HT*8(DELLAM,FRAC)
      IMPLICIT REAL*8 (A-H,O-Z)
      COMMON /H/ RKC,RKL,RJC,RJL,S,RLP,TAUCM
      RK0=RLP*RKL*FRAC/DELLAM
      RJ0=RLP*RJL*FRAC/DELLAM
      TOTK=RK0+RKC
      TAUCM=S*TOTK
      TAUC=S*RKC
      IF(DABS(TAUC) .GT. .3D0) GO TO 1
      H2=TAUC
      GO TO 2
    1 IF(TAUC .LE. 172.D0) GO TO 3
      H2=1.
      GO TO 2
    3 H2=1.-DEXP(-TAUC)
    2 IF(DABS(TAUCM) .GT. .3D0) GO TO 4
      H1=TAUCM
      GO TO 5
    4 IF(TAUCM .LE. 172.D0) GO TO 6
      H1=1.
```

```
      GO TO 5
    6 IF(TAUCM .GE. -172.D0) GO TO 7
      H1=-1.D75
      GO TO 5
    7 H1=1.-DEXP(-TAUCM)
    5 H3=RKC*H1/(TOTK*H2)
      HT=H3*(1.D0+RJO/RJC)-1.D0
      RETURN
      END
```

```
C
C
C      PROGRAM CODE: PROGEN
C
C           THIS PROGRAM TAKES OPACITY AND EMISSIVITY DATA FROM PUPGEN
C           AND CALULATES EMISSION LINE PROFILES FOR A SPECIFIED GAS
C           FLOW GEOMETRY
C              INPUT: R1,R2,A1,A2,Z1,Z2 - DISK GEOMETRY
C                     AI - INCLINATION ANGLE
C                     W0 - REF LINE WAVELENGTH (THERM WIDTHS)
C                     XM - STELLAR MASS (SOLAR M)
C                     XJL - LINE EMISSIVITY (ERG/S-CM**3-STR)
C                     XJC - CONTIN EMISS (ERG/S-CM**3-STR-WIDTH)
C                     XKL - LINE OPACITY (THERM WIDTH/SOLAR R)
C                     XKC - CONTIN OPACITY (SOLAR R**-1)
C                     S0,SSTP,NS - SEPARATION STEPPING PARMS
C                     N - DATA FILE SPECIFIER 1=DISK, 0=PRINTER
C                     EXMX - CONTROL OF OPTICAL DEPTH INTEGRATIONS
C                            SETS EXP(-T) TO 1 IF IT IS >EXMX
C                     WTH - THERMAL WIDTH (ANGSTROMS)
C                     B0F - CONT FLUX*DISTANCE**2 AT HBETA
C                       (ERG/S-WTH)*10**32
C           OUTPUT:   S - PROFILE SEP FROM REF LINE CENTER
C                     VEL - CORRESPONDING DOPPLER VELOCITY (KM/S)
C                     XX - PROFILE HEIGHT
C                     DMAX - MAX DIST EXCLUDED FROM TAU INTEGRATION (SOLAR)
C                     TMX,DISM - MAX TAU,LINE OF SIGHT DIST
C                         (CONTINUUM AND TOTAL)
C                     CORE - CORRECTION FACTOR FOR ALTERATION OF PROFILES
C                     XX0 CALC WITH TAUC=0: XX=CORE*(XX0+1)-1
C                     FC - INTEGRATED CORRECTION FOR FINITE TAU
C                         (SOLAR R**3)
C                     FC0 - CONT FLUX AT HBETA (ERG/S-WIDHT)*10**32
C                     F - FC0/B0F = REL SECOND CONT STRENGTH
C
C
      IMPLICIT REAL*8 (A-H)
      IMPLICIT REAL*8 (C-Z)
      COMMON R,A,R1,R2,A1,A2,Z1,Z2
      COMMON /AA/SINI,COSI,TANI,RST,TA1,DMAX,DSM
      COMMON /AB/XJL,XJC,W0,AI,XM,S,XKL,XKC
      COMMON /AC/XL2,PI,RLP,XKLRLP,XJLRLP
      COMMON /TM/TMX,DISM
      EXTERNAL FF
      EXTERNAL F
      CALL ASSIGN(5,'CR:',3,IND)
      READ(5,100) R1,R2,A1,A2,Z1,Z2
      READ(5,101) XJL,XJC,W0,AI,XM
      READ(5,101) XKL,XKC,EXMX
      READ(5,101) WTH,B0F
```

```
      READ(5,102) S0,SSTP,NS
      READ(5,103) N
  100 FORMAT(6D10.3)
  101 FORMAT(5D15.7)
  102 FORMAT(2D10.3,I3)
  103 FORMAT(I1)
      IF(N .EQ. 1) GO TO 2
      CALL ASSIGN(6,'LP:',3,IND)
      GO TO 3
    2 CALL ASSIGN(6,'DP0:13LP.LST',12,IND)
    3 CONTINUE
      WRITE(6,200) R1,R2,A1,A2,Z1,Z2
      WRITE(6,201) XJL,XJC,W0,AI,XM
      WRITE(6,205) XKL,XKC,EXMX
      WRITE(6,202) S0,SSTP,NS
      WRITE(6,210) WTH,B0F
  200 FORMAT(' R1,R2,A1,A2,Z1,Z2 ARE ',6(3X,D10.3))
  201 FORMAT(' JL,JC,W0,AI,XM ARE ',5(3X,D10.3))
  202 FORMAT(' S0,SSTP,NS ARE ',2(3X,D14.7),I3)
  205 FORMAT(' XKL,XKC,EXMX ARE ',3(3X,D10.3))
  210 FORMAT(' WTH AND B0F ARE ',2(3X,D10.3))
      D=1.456313666D-3
      CO=1.745329252D-2
      PI=3.141592654D0
      XL2=DLOG(2.D0)
      SQM=DSQRT(XM)
      RLP=DSQRT(XL2/PI)
      XKLRLP=XKL*RLP
      XJLRLP=XJL*RLP
      DMAX=DLOG(1.D0/EXMX)/(XKLRLP+XKC)
      WRITE(6,206) DMAX
  206 FORMAT(' DMAX IS ',3X,D10.3)
      AI=AI*CO
      A1=A1*CO
      A2=A2*CO
      SINI=DSIN(AI)
      COSI=DCOS(AI)
      TANI=SINI/COSI
      SA1=DSIN(A1)
      TA1=SA1/DCOS(A1)
      RST=R2*SA1
      DSM=D*SQM*SINI
      V=(Z2-Z1)*(R2*R2-R1*R1)*(A2-A1)/2.D0
      VOL=3.37D32*V
      WRITE(6,204) VOL
  204 FORMAT(' V= ',D10.3)
      TMX=0.D0
      DISM=0.D0
```

```
C
C       RADIUS INTEGRATION FOR THE CONTINUUM
C
        CALL DGG24(R1,R2,FF,FC)
        WRITE(6,208) TMX,DISM
  208 FORMAT(' FOR THE CONTINUUM, TMX AND DISM ARE ',2(D14.7,4X))
        CORE=V/FC
        WRITE(6,209) CORE
  209 FORMAT(' CONTINUUM CORRECTION FACTOR IS ',D14.7)
        FCO=XJC*FC*3.3715D0
        EF=FCO/B0F
        WRITE(6,211) FC,FCO,EF
  211 FORMAT(' FC IS ',3X,D10.3,3X,'IN UNITS OF 10**32 ERGS/SEC-W, FCO
     * IS ',3X,D10.3,10X,'F= ',D10.3)
        WRITE(6,207)
  207 FORMAT(' ',/,10X,'S',16X,'XX',15X,'VEL',15X,'TM',16X,'DM',/)
        DO 1 I=1,NS
        S=S0+(I-1)*SSTP
        TMX=0.D0
        DISM=0.D0
C
C       RADIUS INTEGRATION FOR THE LINE
C
        CALL DGG24(R1,R2,F,FL)
        XX=FL/FC-1.D0
        VEL=(3.0D05*S)/(W0*SINI)
    1 WRITE(6,203) S,XX,VEL,TMX,DISM
  203 FORMAT(' ',5X,5(D14.7,3X))
        STOP
        END
C
C       ANGLE INTEGRATION FOR THE CONTINUUM
C
        DOUBLE PRECISION FUNCTION FF(X)
        IMPLICIT REAL*8 (A-H)
        IMPLICIT REAL*8 (O-Z)
        COMMON R,A,R1,R2,A1,A2
        EXTERNAL GG
        R=X
        CALL DPG24(A1,A2,GG,Y)
        FF=Y
        RETURN
        END
C
C       THICKNESS INTEGRATION FOR THE CONTINUUM
C
        DOUBLE PRECISION FUNCTION GG(X)
        IMPLICIT REAL*8 (A-H)
        IMPLICIT REAL*8 (O-Z)
        COMMON R,A,R1,R2,A1,A2,Z1,Z2
```

```
      EXTERNAL D
      A=X
      CALL SSWTCH(13,J)
      IF(J .EQ. 1) STOP
      CALL DCG24(Z1,Z2,D,Z)
      GG=Z
      RETURN
      END
C
C     INTEGRAND FOR THE CONTINUUM
C
      DOUBLE PRECISION FUNCTION D(X)
      IMPLICIT REAL*8 (A-H)
      IMPLICIT REAL*8 (O-Z)
      COMMON R,A
      COMMON /AA/SINI,COSI
      COMMON /AB/XJL,XJC,W0,AI,XM,S,XKL,XKC
      COMMON /AD/X0,Y0,Z0
      COMMON /TM/TMX,DISM
      X0=R*DCOS(A)
      Y0=R*DSIN(A)
      Z0=X
      YP1=SINI*X0+COSI*Z0
      YD1=0.D0
      YD0=0.D0
      CALL TLIM(YP0,FRG,YD1,YD0)
      DIS=YP0-YP1+YD0-YD1
      DISM=DMAX1(DIS,DISM)
      TAU=XKC*DIS
      TMX=DMAX1(TAU,TMX)
      D=DEXP(-TAU)*R
      RETURN
      END
C
C     ANGLE INTEGRATION FOR THE LINE
C
      DOUBLE PRECISION FUNCTION F(X)
      IMPLICIT REAL*8 (A-H)
      IMPLICIT REAL*8 (O-Z)
      COMMON R,A,R1,R2,A1,A2
      EXTERNAL G
      R=X
      CALL DPG24(A1,A2,G,Y)
      F=Y
      RETURN
      END
C
C     THICKNESS INTEGRATION FOR THE LINE
C
      DOUBLE PRECISION FUNCTION G(X)
```

```
      IMPLICIT REAL*8 (A-H)
      IMPLICIT REAL*8 (O-Z)
      COMMON R,A,R1,R2,A1,A2,Z1,Z2
      EXTERNAL H
      A=X
      CALL SSWTCH(13,J)
      IF(J .EQ. 1) STOP
      CALL DCG16(Z1,Z2,H,Z)
      G=Z
      RETURN
      END
C
C     INTEGRAND FOR THE LINE
C
      DOUBLE PRECISION FUNCTION H(X)
      IMPLICIT REAL*8 (A-H)
      IMPLICIT REAL*8 (O-Z)
      COMMON R,A
      COMMON /AA/SINI,COSI,TANI,RST,TA1,DMAX,DSM
      COMMON /AB/XJL,XJC,W0,AI,XM,S,XKL,XKC
      COMMON /AC/XL2,PI,RLP,XKLRLP,XJLRLP
      VX=DSM*DSIN(A)/DSQRT(R)
      AA=S-W0*VX
      CC=AA*AA
      IF(CC .GT. 126.D0) CC=126.D0
      DD=1.D0/(2.D0**CC)
      RJ=(XJLRLP/XJC)*DD
      TT=T(X)
      IF(TT .GT. 87.D0) TT=87.D0
      H=(RJ+1.D0)*R*DEXP(-TT)
      RETURN
      END
C
C     TAU INTEGRATION FOR THE LINE
C
      DOUBLE PRECISION FUNCTION T(X)
      IMPLICIT REAL*8 (A-H)
      IMPLICIT REAL*8 (O-Z)
      COMMON R,A
      COMMON /AA/SINI,COSI,TANI,RST,TA1,DMAX,DSM
      COMMON /AD/X0,Y0,Z0
      COMMON /TM/TMX,DISM
      EXTERNAL E
      E1=0.D0
      E2=0.D0
      XD0=0.D0
      XD1=0.D0
      X0=R*DCOS(A)
      Y0=R*DSIN(A)
      Z0=X
```

```
      XP1=SINI*X0+COSI*Z0
      CALL TLIM(XP0,FLG,XD1,XD0)
      DIS=XP0-XP1+XD0-XD1
      DISM=DMAX1(DIS,DISM)
      IF(DABS(XP1-XP0) .LE. DMAX) GO TO 1
      CALL DPG16(XP1,XP0,E,E1)
    1 IF(FLG .EQ. 0) GO TO 2
      IF(DABS(XD1-XD0) .LE. DMAX) GO TO 2
      CALL DPG16(XD1,XD0,E,E2)
    2 T=E1+E2
      TMX=DMAX1(T,TMX)
      RETURN
      END
C
C     FINDS BOUNDS FOR THE TAU INTEGRATION
C          FLG LABELS THE NUMBER OF PIECES FOUND
C          XP0,XD1,XD0 ARE THE BOUNDS
C
      SUBROUTINE TLIM(XP0,FLG,XD1,XD0)
      DOUBLE PRECISION XP0,XD1,XD0,R,A,A2,Z1
      COMMON R,A,R1,D1,R2,D2,A1,D3,A2,Z1,Z2
      COMMON /AA/SINI,D4,COSI,D5,TANI,D6,RST,D7,TA1
      COMMON /AD/X0,D8,Y0,D9,Z0
      XXD1=0.
      XXD0=0.
      FLG=0
      G=X0-Z0*TANI
      H=Z0-X0/TANI
      IF(Y0 .LT. R1) GO TO 1
    6 SZ=Z2
      SX=TANI*SZ+G
      SR=SQRT(SX*SX+Y0*Y0)
      SA=ATAN2(Y0,SX)
      IF(SR .LE. R2 .AND. SA .GE. A1) GO TO 2
      IF(Y0 .LT. RST) GO TO 3
      SX=SQRT(R2*R2-Y0*Y0)
      GO TO 4
    3 SX=Y0/TA1
    4 SZ=SX/TANI+H
    2 IF(FLG .EQ. 1) GO TO 5
    8 XXP0=SINI*SX+COSI*SZ
      GO TO 9
    5 XXD0=SINI*SX+COSI*SZ
      GO TO 9
    1 IF(X0 .GE. 0.) GO TO 6
      SX=-SQRT(R1*R1-Y0*Y0)
      SZ=SX/TANI+H
      IF(SZ .LT. Z2) GO TO 7
      SZ=Z2
      SX=TANI*SZ+G
```

```
      GO TO 8
    7 XXP0=SINI*SX+COSI*SZ
      SX=SQRT(R1*R1-Y0*Y0)
      SZ=SX/TANI+H
      IF(SZ .GE. Z2) GO TO 9
      FLG=1
      XXD1=SINI*SX+COSI*SZ
      GO TO 6
    9 XP0=DBLE(XXP0)
      XD0=DBLE(XXD0)
      XD1=DBLE(XXD1)
      RETURN
      END
C
CC    TAU INTEGRAND (AT LINE)
C
      DOUBLE PRECISION FUNCTION E(X)
      IMPLICIT REAL*8 (A-H)
      IMPLICIT REAL*8 (O-Z)
      COMMON /AA/SINI,COSI,TANI,RST,TA1,DMAX,DSM
      COMMON /AB/XJL,XJC,W0,AI,XM,S,XKL,XKC
      COMMON /AC/XL2,PI,RLP,XKLRLP,XJLRLP
      COMMON /AD/X0,Y0,Z0
      YP=Y0
      ZP=-COSI*X0+SINI*Z0
      VX=SINI*X-COSI*ZP
      VX=(VX*VX+YP*YP)**.75D0
      VX=(DSM/VX)*YP
      AA=S-W0*VX
      CC=AA*AA
      IF(CC .GT. 126.D0) CC=126.D0
      DD=1.D0/(2.D0**CC)
      E=XKLRLP*DD+XKC
      RETURN
      END
C
CC    THE FOLLOWING ARE EXAMPLES OF THE 12,16,24,32 POINT GAUSS
CC         QUADRATURES USED IN PROGEN
C
C
CC    12-POINT
C
      SUBROUTINE DPG12(XL,XU,FCT,Y)
      DOUBLE PRECISION XL,XU,Y,A,B,C,FCT
      A=.5D0*(XU+XL)
      B=XU-XL
      C=.4907803171233596 3D0*B
      Y=.2358766819325591 4D-1*(FCT(A+C)+FCT(A-C))
      C=.4520586281852374 3D0*B
      Y=Y+.5346966299765921 5D-1*(FCT(A+C)+FCT(A-C))
```

```
      C=.38495133709715234D0*B
      Y=Y+.80039164271673110-1*(FCT(A+C)+FCT(A-C))
      C=.29365897714330872D0*B
      Y=Y+.10158371336153296D0*(FCT(A+C)+FCT(A-C))
      C=.18391574949909010D0*B
      Y=Y+.11674626826917740D0*(FCT(A+C)+FCT(A-C))
      C=.62616704255734458D-1*B
      Y=B*(Y+.12457352290670139D0*(FCT(A+C)+FCT(A-C)))
      RETURN
      END
C
CC    16-POINT
C
      SUBROUTINE DPG16(XL,XU,FCT,Y)
      DOUBLE PRECISION XL,XU,Y,A,B,C,FCT
      A=.5D0*(XU+XL)
      B=XU-XL
      C=.49470046749582497D0*B
      Y=.13576229705877047D-1*(FCT(A+C)+FCT(A-C))
      C=.47228751153661629D0*B
      Y=Y+.31126761969323946D-1*(FCT(A+C)+FCT(A-C))
      C=.43281560119391587D0*B
      Y=Y+.47579255841246392D-1*(FCT(A+C)+FCT(A-C))
      C=.37770220417750152D0*B
      Y=Y+.62314485627766936D-1*(FCT(A+C)+FCT(A-C))
      C=.30893812220132187D0*B
      Y=Y+.74797994408288370-1*(FCT(A+C)+FCT(A-C))
      C=.22900838882861369D0*B
      Y=Y+.84578259697501270-1*(FCT(A+C)+FCT(A-C))
      C=.14080177538962946D0*B
      Y=Y+.91301707522461790-1*(FCT(A+C)+FCT(A-C))
      C=.47506254918818720D-1*B
      Y=B*(Y+.94725305227534250-1*(FCT(A+C)+FCT(A-C)))
      RETURN
      END
C
CC    24-POINT
C
      SUBROUTINE DPG24(XL,XU,FCT,Y)
      DOUBLE PRECISION XL,XU,Y,A,B,C,FCT
      A=.5D0*(XU+XL)
      B=XU-XL
      C=.49759360999851068D0*B
      Y=.61706148999935993D-2*(FCT(A+C)+FCT(A-C))
      C=.48736427798565475D0*B
      Y=Y+.14265694314466832D-1*(FCT(A+C)+FCT(A-C))
      C=.46913727600136638D0*B
      Y=Y+.22138719408709903D-1*(FCT(A+C)+FCT(A-C))
      C=.44320776350220052D0*B
```

```
      Y=Y+.29649292457718390D-1*(FCT(A+C)+FCT(A-C))
      C=.41000099298695146D0*B
      Y=Y+.36673240705540153D-1*(FCT(A+C)+FCT(A-C))
      C=.37006209578927718D0*B
      Y=Y+.43095080765976638D-1*(FCT(A+C)+FCT(A-C))
      C=.32404682596848778D0*B
      Y=Y+.48809326052056944D-1*(FCT(A+C)+FCT(A-C))
      C=.27271073569441977D0*B
      Y=Y+.53722135057982817D-1*(FCT(A+C)+FCT(A-C))
      C=.21689675381302257D0*B
      Y=Y+.57752834026862801D-1*(FCT(A+C)+FCT(A-C))
      C=.15752133984808169D0*B
      Y=Y+.60835236463901696D-1*(FCT(A+C)+FCT(A-C))
      C=.95559433736808150-1*B
      Y=Y+.62918728173414148D-1*(FCT(A+C)+FCT(A-C))
      C=.32028446431302813D-1*B
      Y=B*(Y+.63969097673376078D-1*(FCT(A+C)+FCT(A-C)))
      RETURN
      END
C
C     32-POINT
C
      SUBROUTINE  DPG32(XL,XU,FCT,Y)
      DOUBLE PRECISION XL,XU,Y,A,B,C,FCT
      A=.5D0*(XU+XL)
      B=XU-XL
      C=.49863193092474078D0*B
      Y=.35093050047350483D-2*(FCT(A+C)+FCT(A-C))
      C=.49280575577263417D0*B
      Y=Y+.81371973654528350-2*(FCT(A+C)+FCT(A-C))
      C=.48238112779375322D0*B
      Y=Y+.12696032654631030D-1*(FCT(A+C)+FCT(A-C))
      C=.46745303796886984D0*B
      Y=Y+.17136931456510717D-1*(FCT(A+C)+FCT(A-C))
      C=.44816057788302606D0*B
      Y=Y+.21417949011113340D-1*(FCT(A+C)+FCT(A-C))
      C=.42468380686628499D0*B
      Y=Y+.25499029631188088D-1*(FCT(A+C)+FCT(A-C))
      C=.39724189798397120D0*B
      Y=Y+.29342046739267774D-1*(FCT(A+C)+FCT(A-C))
      C=.36609105937014484D0*B
      Y=Y+.32911111388180923D-1*(FCT(A+C)+FCT(A-C))
      C=.33152213346510760D0*B
      Y=Y+.36172897054424253D-1*(FCT(A+C)+FCT(A-C))
      C=.29385787862038116D0*B
      Y=Y+.39096947893535153D-1*(FCT(A+C)+FCT(A-C))
      C=.25344995446611470D0*B
      Y=Y+.41655962113473378D-1*(FCT(A+C)+FCT(A-C))
      C=.21067563806531767D0*B
      Y=Y+.43826046502201906D-1*(FCT(A+C)+FCT(A-C))
```

```
C=.16593430114106382D0*B
Y=Y+.45586939347881942D-1*(FCT(A+C)+FCT(A-C))
C=.11964368112606854D0*B
Y=Y+.46922199540402283D-1*(FCT(A+C)+FCT(A-C))
C=.72235980791398250-1*B
Y=Y+.47819360039637430D-1*(FCT(A+C)+FCT(A-C))
C=.24153832843869158D-1*B
Y=B*(Y+.48270044257363900D-1*(FCT(A+C)+FCT(A-C)))
RETURN
END
```

```
C
C
C      PROGRAM CODE: PROFIT
C
C           THIS PROGRAM PLOTS THE DATA PRODUCED BY PROGEN.
C           MODE=0 PLOTS ONE SET OF DATA AND DISPLAYS THE BEST
C           GAUSSIAN FIT TO A SELECTED PORTION OF THAT PROFILE
C           MODE>0 DRAWS MODE PROFILES PER PLOT
C           MOD2=0 PLOTS RELATIVE FLUX
C           MOD2=1 PLOTS LINE HEIGHT (H)
C           INPUT:   NGPHS - GRAPHS PER RUN
C                    GRAPH PARMS (LABELS,SCALES)
C                    NPTS - NUMBER OF POINTS
C                    NSYM,MODPLT - PLOT PARMS
C                    WTH - THERMAL HWHM (ANGSTROMS)
C                    EF - REL SECONDARY CONT STRENGTH
C                    SEP0,SEPSTP - X-AXIS POINT SPECIFIERS
C                    HARY - Y-AXIS VALUES
C                    NF,NL - GAUSS FIT RANGE (LOCATES POINTS IN HARY)
C                    NPF,NPL - PLOT RANGE
C           OUTPUT:  GRAPHS
C                    GAUSS FIT PARMS
C
C
      IMPLICIT REAL*8 (A-H,O-Z)
      REAL*4 XLAB(5),YLAB(5),GLAB(5),DATLAB(5),VELARA(35),HARA(35),SNGL,
     *XSZ,YSZ,XSF,YSF,XMN,YMN,YLBL(5)
      DIMENSION ANGARY(35),HARY(35),PARM(4),X(3),XJAC(35,3)
      DIMENSION WRK(91),F(35),XJTJ(6)
      COMMON FTXARY(35),FTYARY(35),C,AA,BB
      EXTERNAL FUN
      SINI=.838670568
      COR=3.0D05/(4861.D0*SINI)
      C=-1.D0*DLOG(2.D0)
      RPL=DSQRT(-3.141592654/C)
      READ(5,100) NGPHS
      READ(5,102) XLAB,YLAB,YLBL
      DO 1 I=1,NGPHS
      AA=1.0D0
      BB=0.0D0
      M=0
      READ(5,102) GLAB
      READ(5,101) XSZ,YSZ,XSF,YSF,XMN,YMN
      READ(5,100) MODE,MOD2
      IF(MOD2 .EQ. 1) GO TO 15
      WRITE(6,200) GLAB
      GO TO 6
   15 WRITE(6,205) GLAB
    6 READ(5,102) DATLAB
      READ(5,100) NPTS,NSYM,MODPLT
```

```
      READ(5,103) WTH,EF,SEP0,SEPSTP
      READ(5,104) (HARY(J),J=1,NPTS)
      EF=EF*1000.D0
      WRITE(6,201) DATLAB
      WRITE(6,204) WTH,EF
      DO 16 J=1,NPTS
      ANGARY(J)=WTH*(SEP0+(J-1)*SEPSTP)
   16 VELARA(J)=SNGL(COR*ANGARY(J))
      IF(MOD2 .EQ. 1) GO TO 10
      AA=EF
      BB=EF
      DO 2 K=1,NPTS
      HARY(K)=EF*HARY(K)+EF
    2 HARA(K)=SNGL(HARY(K))
      GO TO 12
   10 DO 11 K=1,NPTS
   11 HARA(K)=SNGL(HARY(K))
   12 CONTINUE
      IF(M .NE. 0) GO TO 3
      IF(MOD2 .EQ. 0) GO TO 13
      CALL GRAPH(NPTS,VELARA,HARA,NSYM,MODPLT,XSZ,YSZ,XSF,XMN,YSF,YMN,
     *XLAB,YLBL,GLAB,DATLAB)
      GO TO 14
   13 CALL GRAPH(NPTS,VELARA,HARA,NSYM,MODPLT,XSZ,YSZ,XSF,XMN,YSF,YMN,
     *XLAB,YLAB,GLAB,DATLAB)
   14 CONTINUE
      M=1
    7 IF(MODE-1) 4,1,5
    5 MODE=MODE-1
      GO TO 6
    3 MODPLT=MODPLT+100
      CALL GRAPHS(NPTS,VELARA,HARA,NSYM,MODPLT,DATLAB)
      GO TO 7
    4 READ(5,100) NF,NL
      II=0
      MM=NL-NF+1
      DO 8 J=NF,NL
      II=II+1
      FTXARY(II)=ANGARY(J)
    8 FTYARY(II)=HARY(J)
      READ(5,103) (X(J),J=1,3)
      CALL ZXSSQ(FUN,MM,3,5,0.,0.,200,1,PARM,X,SS,F,XJAC,MM,XJTJ,WRK,
     *INFER,IER)
      READ(5,100) NPF,NPL
      MMM=NPL-NPF+1
      III=0
      DO 9 J=NPF,NPL
      III=III+1
      ANGARY(III)=ANGARY(J)
      HARY(III)=BB+AA*X(1)*DEXP(C*((ANGARY(III)-X(2))/X(3))**2)
```

```
      VELARA(III)=VELARA(J)
    9 HARA(III)=SNGL(HARY(III))
      EW=EF*X(1)*X(3)*RPL/(1000.D0+EF)
      X(2)=CCR*X(2)
      WRITE(6,202) (X(J),J=1,3),EW,NF,NL,NPF,NPL
      CALL GRAPHS(MMM,VELARA,HARA,0,102,'    GAUSSIAN FIT;')
    1 WRITE(6,203)
      STOP
  100 FORMAT(5I3)
  101 FORMAT(6F10.4)
  102 FORMAT(20A4)
  103 FORMAT(8G10.4)
  104 FORMAT(10(G7.3,1X))
  200 FORMAT(' ',10X,'THIS IS ',5A4,5X,'A FLUX PLOT',//,15X,' PLOTS ARE
     *AS FOLLOWS',/)
  201 FORMAT(' ',20X,5A4)
  202 FORMAT(' ',23X,'GAUSSIAN FIT HAS H=',F6.2,' POS=',F6.2,'  W=',
     *F6.2,'  EW= ',F4.3,'    WITH NF,NL,NPF,NPL BEING ',4(I3,2X))
  203 FORMAT(////)
  204 FORMAT(' ',27X,'WTH(ANGSTROMS) AND F(UNITS OF 10 TO THE -3) ARE  '
     *,2(F5.3,5X))
  205 FORMAT(' ',10X,'THIS IS ',5A4,5X,'A HEIGHT PLOT',//,15X,' PLOTS AR
     *E AS FOLLOWS',/)
      END
      SUBROUTINE FUN(X,M,N,F)
      IMPLICIT REAL*8 (A-H,O-Z)
      DIMENSION X(N),F(M)
      COMMON ANGARY(35),HARY(35),C,AA,BB
      DO 1 I=1,M
    1 F(I)=HARY(I)-(BB+AA*X(1)*DEXP(C*((ANGARY(I)-X(2))/X(3))**2))
      RETURN
      END
```